Spin-dependent Transport in Current-in-plane Giant Magnetoresistive Devices:
Materials Selection, Structure and Properties

Kresna Bondan Fathoni

February 2022

Spin-dependent Transport in Current-in-plane Giant Magnetoresistive Devices:
Materials Selection, Structure and Properties

Kresna Bondan Fathoni
Doctoral Program in Materials Science and Engineering

Submitted to the Graduate School of
Pure and Applied Sciences
in Partial Fulfillment of the Requirements
for the Degree of Doctor of Philosophy in
Engineering

at the
University of Tsukuba

Contents

Chapter 1: Introduction 1

1.1. Spintronics and magnetoresistance effect 1

1.2. Magnetic sensors 2

1.3. Current in-plane giant magnetoresistive (CIP-GMR) spin valve 3

1.3.1. Electron transport in CIP-GMR 5

1.3.2. Effect of materials selection in CIP-GMR 7

1.3.3. Effect of layer thicknesses in CIP-GMR 8

1.3.4. Effect of specular reflection in CIP-GMR 9

1.4. Materials selection in this thesis 10

1.4.1. Heusler alloy ferromagnets 10

1.4.2. Co-Fe-Ni alloy ferromagnets 12

1.5. Outline 13

Chapter 2: Experimental method 15

2.1. Sputter deposition 15

2.2. Microfabrication 16

2.2.1. Optical lithography 16

2.2.2. Ion etching 16

2.3. Electric and magnetic properties characterization 17

2.3.1. Vibrating-sample magnetometer (VSM) 17

2.3.2. DC four-point probe 17

2.4. Structural properties characterization 19

2.4.1. Reflective high-energy electron diffraction (RHEED) 19

2.4.2. X-ray diffraction (XRD) 19

2.4.3. Transmission electron microscope (TEM) 19

Chapter 3: Epitaxial current-in-plane giant magnetoresistance using $Co_2FeAl_{0.5}Si_{0.5}$ Heusler alloy 21

3.1. Experiments and Results 22

3.2. Discussion 27

3.3. Summary 31

Chapter 4: Epitaxial Current-in-plane giant magnetoresistance in $Co_{1-x}Fe_x/Cu/Co_{1-x}Fe_x$ multilayers 33

4.1. Experiment 33

4.2. Results and discussion 34

4.3. Summary 43

Chapter 5: Reduction of coercivity on epitaxial current-in-plane giant magnetoresistance using CoFeNi alloy 45

- 5.1. Epitaxial bcc-$Ni_{75}Fe_{25}$/Cu–based CIP-GMR spin valve ... 46
  - 5.1.1. Experiments and Results ... 47
  - 5.1.2. Discussion ... 49
- 5.2. Epitaxial bcc-CoFeNi/Cu–based CIP-GMR spin valve ... 50
  - 5.2.1. Experiments and Results ... 51
  - 5.2.2. Discussion ... 55
- 5.3. Summary ... 56

Chapter 6: Epitaxial bcc-Cu-based current-in-plane giant magnetoresistance on Si substrate ... 57

- 6.1. Preliminary work: The bcc-Cu–based CIP-GMR on amorphous SiO_x substrate ... 57
  - 5.1.1. Experiments and Results ... 58
  - 5.1.2. Discussion ... 60
- 6.2. Epitaxial bcc-Cu–based current-in-plane giant magnetoresistance on Si substrate ... 62
  - 5.1.1. Experiments and Results ... 62
  - 5.1.2. Discussion ... 71
- 6.3. Summary ... 73

Chapter 7: Summary and future prospects ... 75

References ... 77

Publications ... 84

Chapter 1: Introduction

1.1. Spintronics and magnetoresistance effect

Spintronic is one of the major physics that deals with manipulating electronic spin inside of materials. Nowadays spintronic has found its way to expand its application as storage devices, magnetic field sensors, magnetic memory, spin-based quantum computing and more[1]. It starts by the discovery of anisotropic magnetoresistance (AMR) in 1857 by William Thomson where the resistance changes depending on the relative orientation between its magnetization and current direction[2]. Then, along with the advancements in the thin film technology, the first big leap in the spintronic was the discovery of giant magnetoresistance (GMR) effect found in ferromagnet (FM)/nonmagnet (NM)/FM multilayers by Grünberg et al and Fert et al. in 1988[3,4].

It has been more than three decades since the discovery of current in-plane giant magnetoresistance (CIP-GMR) effect. This technology has reached maturity and has been widely used in many applications. The discovery of this effect does give a big impact towards the application of spintronics. Initially, this technology was developed for read head sensor in hard-disk drive. During its emerging era, many researchers jump into this topic resulting in the development of this technology in rapid pace. As the time goes, the application broadens beyond just for read head sensor. With materials engineering, the response of the sensor can be manipulated to behave linearly which opens for more capabilities. CIP-GMR has several advantage which make this old technology stay relevant. It has relatively high sensitivity, which can still be improved further. The in-plane nature of this device give flexibility to tune and adjust its macroscopic properties. It also does not need multiple process to be used, therefore easy to integrate into other technologies.

The term giant magnetoresistance refers to the big change in the resistance when external magnetic field is applied to this structure. As depicted in Figure 1.1(a) the resistance changes depending on the magnetization of the magnetic film. At zero field, the magnetization is antiparallel. Because each spin direction scattered differently in FM materials[5], each spin direction will be scattered more in one or the other FM layer. When magnetic field is applied, the magnetizations of the FM layers are aligned in parallel. One of the spin directions will be less scattered which lead to the decrease of resistance. The figure of merit which is $\Delta R/R_P$ or simply called MR ratio then can be calculated (MR ratio $= (R_{AP} - R_P)/R_P$). Historically GMR was setup to have contacts on top of the thin film multilayers as seen in Figure 1.1(b) which allows the current to flow in-plane to the film. Device with this configuration is called current-in-plane (CIP) GMR. Several years after the discovery of this effect, CIP-GMR was introduced as read-head sensor in hard-disk drive[6]. Since then, the research continues to mature and propagating into other magnetic sensing applications as well[7].

GMR with different configuration is also possible with current flowing perpendicular-to-plane (CPP) instead of in-plane as seen in Figure 1.1(c). To ensure the current distribution is homogeneous and flowing vertically throughout the multilayers, lateral size of this device need to be very small (<1μm^2) which is possible to achieve thanks to the advancement of the microfabrication technology. Because current can reliably pass through all layers compared to

CIP-GMR, obtained MR ratio is larger for the same thin film samples[8]. Another phenomenon called tunnel magnetoresistance (TMR) occurs when two ferromagnetic layers is separated by an insulator and current flows normal to the film as seen in Figure 1.1(d)[9,10]. This effect utilizes the spin-dependent tunneling through thin insulating barrier which exhibit much larger MR ratio compared to GMR effect. TMR effect ended up replacing CIP-GMR as read-head sensor until now.

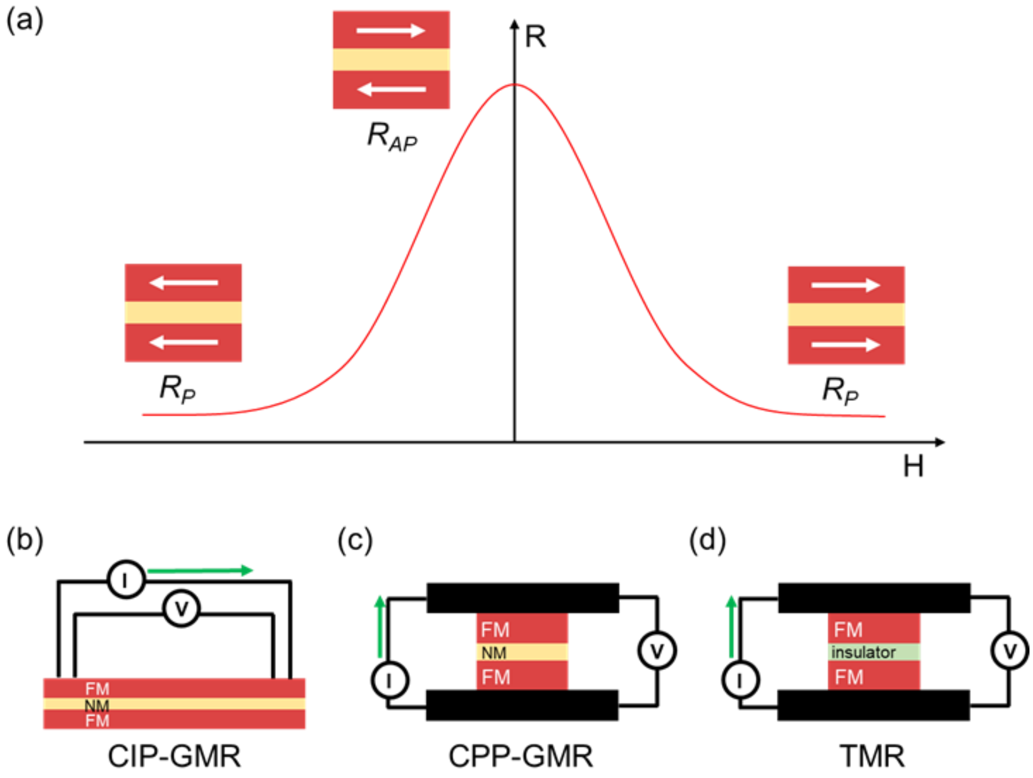

Figure 1.1 (a) Schematic illustration of external field dependence of resistance in magnetoresistive devices. Schematic illustration of (b) CIP-GMR, (c) CPP-GMR and (d) TMR devices.

1.2. Magnetic sensors

Magnetic sensors are devices which measure magnitude and/or direction of magnetic field. This can be used for general measurement of magnetic field or specialized use such as electronic compass, proximity measurement and non-destructive testing for microcracks. Over the past few decades, magnetic sensors have been developed and are commercially used based on various phenomenon such as superconducting interference device (SQUID), Hall effect, flux gate, AMR, GMR and TMR sensors. Optimal magnetic sensors should fulfill several parameters that are specific for each application. Some parameters are defined by the intrinsic properties of the multilayer, while others can be modified using electrical engineering and microfabrication. Often than not, improving one parameter lead to the decrease of the others, therefore optimizations are always required. The general required properties for magnetoresistive devices to be used as magnetic sensors are as follows[11–15]:

1. High sensitivity, defined by S = (MR ratio)/ΔH at operating range.
2. Small nonlinearity at operating range, ideally linear range is larger than operating range.
3. Small coercivity, to reduce hysteresis error.
4. Resistance and sheet resistance is optimal for the system.
5. Good stability over long period of use.
6. Low intrinsic noise within operation frequency

1.3. Current-in-plane giant magnetoresistive (CIP-GMR) spin valve

Shortly after the discovery of GMR effect, spin-valve type CIP-GMR was introduced by Dieny et al[16,17] driven by the needs for magnetic switching at lower external field. Although the GMR value of interlayer coupled magnetic multilayer is larger (>80% at RT), the field required to saturate the device can be as high as 20 kOe which largely reduce the sensitivity and impractical for real application. Spin valve which generally has MR ratio ranging from 5-15% can be switched with external field as low as 2 Oe.

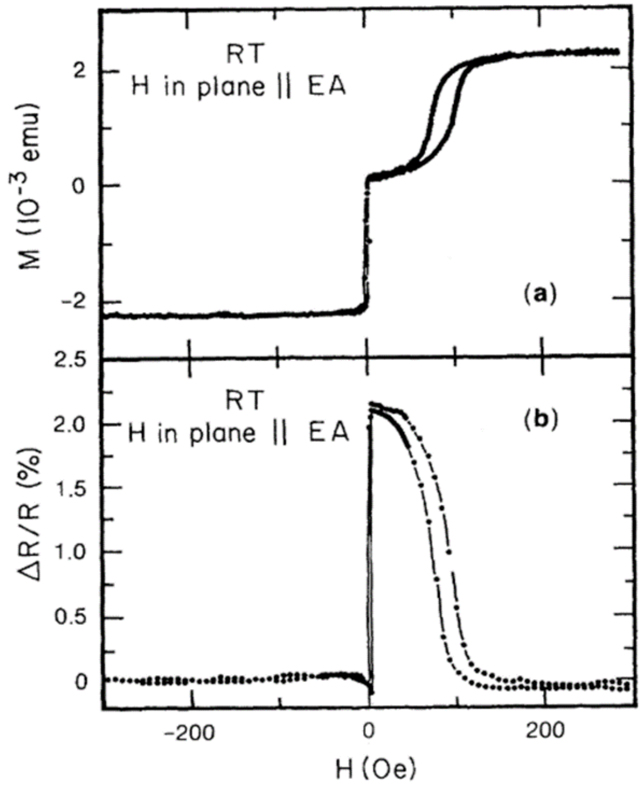

Figure 1.2 Magnetization (a) and magnetoresistance (b) curve of spin valve with the structure of NiFe(15 nm)/Cu(2.6 nm)/NiFe(15 nm)/FeMn(10 nm). MR ratio is 2% with switching field of 7 Oe at RT[17].

A spin valve consists of FM/NM/FM multilayers with one of the FM layers (called pinned layer) is exchange-coupled to an antiferromagnetic (AFM) layer. This exchange coupling pins the magnetization direction of this layer to certain direction which shift the hysteresis loop off-center. The other FM (free layer) is freely switching unrelated to the pinned layer if the coupling between both FM layers is weak enough. Free layer is usually consisted of magnetically soft FM layer in order to switch its magnetization at close to zero with as small hysteresis as possible, resulting in highly sensitive magnetoresistive device which can be used for low field application. In less than a decade, this invention leads to its application as read-head sensor in hard-disk drive, first commercialized by IBM, which would be used for years[6]. This attracts many researchers to discover more suitable materials for achieving larger MR ratio. In 1995, a new phenomenon was discovered in magnetic tunnel junction of Fe/AlO_x/Fe called tunnel magnetoresistance (TMR)[18,19]. TMR effect exhibits resistance change when exposed to external magnetic field similar to CIP-GMR but with much larger MR ratio >100% at RT. This effect utilizes tunneling effects which allow specific electron spin to decay faster during tunneling resulting in larger sensitivity. Because tunneling occurs perpendicularly in respect to the film, microfabrication into small "pillar" is necessary. Due to its large signal output, lower power consumption and small size, TMR replaces CIP-GMR as read-head sensor in 2005. From this point while the material development of TMR is starting to bloom, the research in CIP-GMR become less prominent[15].

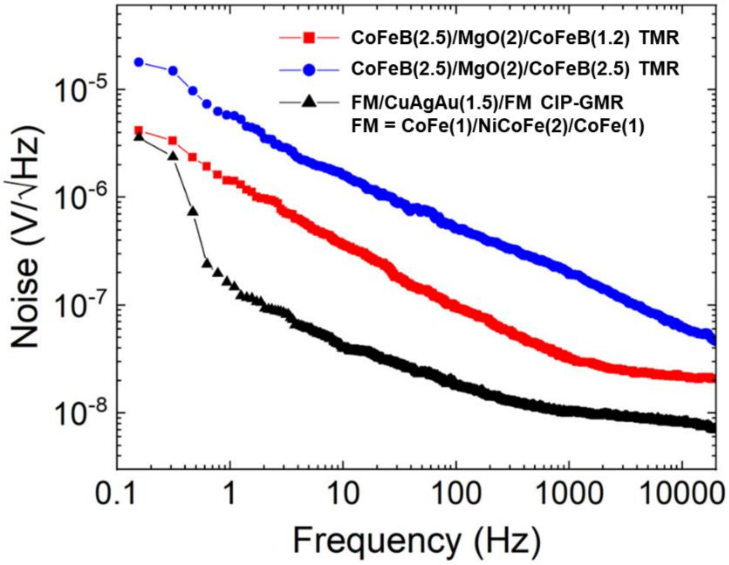

Figure 1.3 Comparison of noise voltage spectral density of Ta(5 nm)/Ru(5 nm)/IrMn(11 nm)/CoFe(2 nm)/Ru(0.9 nm)/CoFeB(2.5 nm)/MgO(2 nm)/CoFeB(1.2 nm) TMR, Ta(5 nm)/Ru(5 nm)/IrMn(11 nm)/CoFe(2 nm)/Ru(0.9 nm)/CoFeB(2.5 nm)/MgO(2 nm)/CoFeB(2.5 nm) TMR and Ta(5 nm)/Ru(5 nm)/IrMn(11 nm)/CoFe(2 nm)/Ru(0.9 nm)/CoFe(1 nm)/NiCoFe(2 nm)/CoFe(1 nm)/CuAgAu(1.5 nm)/CoFe(1 nm)/NiCoFe(2 nm)/CoFe(1 nm) CIP-GMR devices[20].

Although CIP-GMR is no more used as read-head sensors, it has been used for magnetic sensors commercially. Research is also extensively done to explore the possibility of use in wider range of applications including medical diagnostics using biomagnetism of human body, sensor for specific biomolecules using modified magnetic nanoparticles, speed, velocity and proximity sensor in automotive and industrial applications[14,21–25]. For medical application in particular due to small biomagnetic signal (<1 pT), lower detectivity is required. Detectivity, defined as noise signal divided by sensitivity, is limited by the signal to noise ratio (SNR) which means that increasing signal output (MR ratio) and reduction of noise level in low frequency range (< 100Hz) is necessary. Currently SQUID is the most established and reliable method to detect such small biomagnetic signal. The detectivity limit of SQUID is as low as 1 $fT/Hz^{0.5}$. However, the operation cost of the machine is high due to the need for cryogenic operation temperature to maintain superconductivity[26–28]. At room temperature, the closest magnetoresistive device in detecting biomagnetic signal, from the heart and potentially from the brain, is TMR devices due to having large MR ratio, thus improving detectivity down to <1 $pT/Hz^{0.5}$ range[29,30]. However, due to the size constrain of TMR device, the low frequency noise (1/f) noise is relatively high. In this regard, CIP-GMR has the advantage. As seen in Figure 1.3, GMR device show much lower 1/f noise mainly due to larger device size in general thanks to the averaging effect[20]. Another advantage of CIP-GMR is the flexibility of having in-plane configuration. Device can be designed as needed for example to modify its resistance or to suppress external noise[31]. However, at the current stage, the MR ratio is still too low. Currently the progress for improving MR ratio of CIP-GMR is stagnant for more than 15 years with the maximum value of 15% for spin valve and 27% for specular reflective pseudo spin valve[32,33]. Improving MR ratio of CIP-GMR device is necessary to reduce the detectivity limit of magnetoresistive device for future applications.

1.3.1 Electron transport in CIP-GMR

In a ferromagnetic material such as Co, the *3d* band splits because of exchange interaction resulting in the majority and minority spin has different state at the Fermi level as seen in Figure 1.4(a) and (b). The majority-spin have highly dispersive sp band at the Fermi level which have high mobility, thus more conductive. The minority-spin have d band at the Fermi level instead, which has low mobility because of its high effective mass. The different characteristic for each spin, creates different resistivity for both majority ($\rho_\uparrow$) and minority spin ($\rho_\downarrow$). The current flowing through a material can be considered as current flowing through two different conduction channel in parallel, thus called two current model[34]. Then, spin polarization of electric current passing through an FM material can be defined as $P = (\rho_\downarrow - \rho_\uparrow)/(\rho_\downarrow + \rho_\uparrow)$.

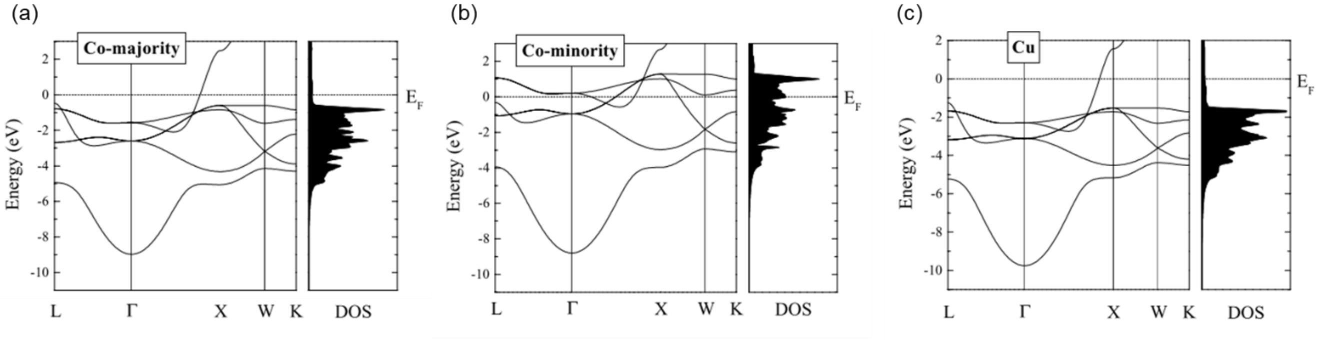

Figure 1.4 Electronic band structures and density of states of (a) fcc-Cu as well as (b) majority- and (c) minority-spin of fcc-Co[35].

Figure 1.5 show the potential energy of a CIP-GMR having an alternating Co/Cu/Co/Cu structure. Co layers can have two possible magnetization configurations, namely parallel and antiparallel. In the case of parallel configuration, the majority-spin electron experience smaller scattering compared to the minority-spin. In antiparallel configuration both majority- and minority-spin electron experience increased scattering in either one of the Co layers. As a result, when the magnetization of the Co layers is parallel, the resistivity of the multilayer is lower because the majority-spin is freely moving with minimal scattering. Whereas in antiparallel configuration both spin experience increased scattering which lead to increased resistivity.

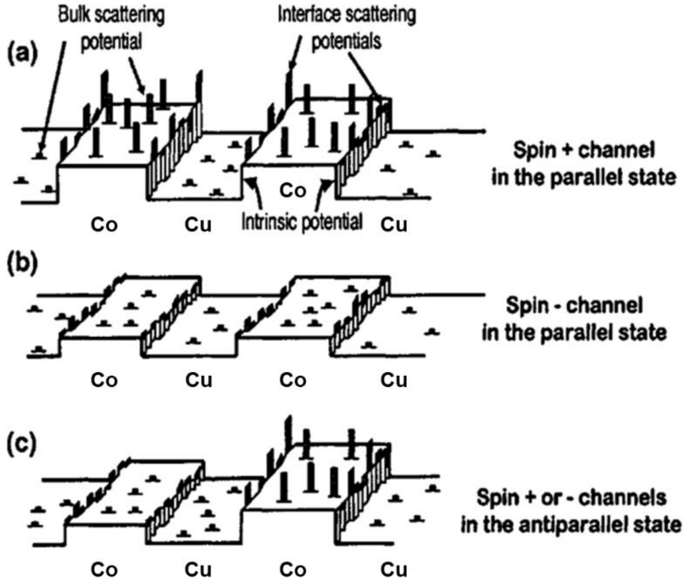

Figure 1.5 Schematics of potential energy of Co/Cu/Co/Cu multilayers. The height of the landscape represent intrinsic potential energy of either spin of Co and Cu whereas the spikes represent scattering potential. (a) Minority-spin channel

and (b) majority-spin channel in parallel state showing opposing feature. In contrast, (c) antiparallel state showing identical scattering density for either spin[36].

Then CIP-GMR can be explained as follows. Within the Co/Cu/Co/Cu multilayers while in parallel configuration, majority-spin electrons are weakly scattered throughout all layers therefore will have lower resistivity ($\rho_\uparrow$). The opposite is true for minority-spin causing it to have larger resistivity ($\rho_\downarrow$). Similar in the case of single FM material, the total resistivity of this multilayer in parallel configuration can be estimated using two-current model.

$$\rho_P = \frac{\rho_\uparrow \rho_\downarrow}{\rho_\uparrow + \rho_\downarrow}$$

In contrast, for antiparallel configuration, both spin directions are equally scattered. They are scattered strongly or weakly depending on the site of scattering, whether it is in the aligned magnetization or opposing magnetization. The resistivity of the multilayer then can be estimated as below.

$$\rho_{AP} = \frac{(\rho_\uparrow + \rho_\downarrow)}{4}$$

CIP-GMR then can be calculated as

$$\frac{\Delta R}{R_P} = \frac{\Delta \rho}{\rho_P} = \frac{\rho_{AP} - \rho_P}{\rho_P} = \frac{(\rho_\uparrow - \rho_\downarrow)^2}{4\rho_\uparrow \rho_\downarrow}$$

The above-mentioned theory[37,38] covers the basis of GMR mechanism with only considering spin-dependent scattering effects. In addition to the spin-dependent scattering due to different scattering density between majority- and minority-spin, there is also difference in potential energy[39,40], for example between Co and Cu layer as shown in Figure 1.5. This also contributes to spin-dependent transport. The matching between the band structure of Co majority-spin and Cu resulting in flatter potential throughout the layers which is the opposite for minority-spin. More detailed theory was developed over the years which involves more relevant parameters such as the difference in lattice potential and spin-dependent interfacial resistivities.

1.3.2 Effect of materials selection in CIP-GMR

In the history of CIP-GMR, certain combination of FM and NM materials can yield large magnetoresistance whereas the other are not. One good example is Fe/Cr and Co/Cu multilayers with MR ratio up to 42% and 65% at RT, respectively[41,42]. When the pairs are swapped to each other, Fe/Cu and Co/Cr multilayers exhibit much lower MR ratio of 5.5% and 3% at RT, respectively[43,44]. There are two important factors which have to be considered to achieve large MR ratio value in CIP-GMR. First one is high band matching between FM and NM layers. Figure 1.4 shows the electronic band structures for majority- and minority-spin of Co as well as Cu. Cu shows delocalized *sp* band at the Fermi level which makes Cu highly conductive. Co shows different band structure between its majority- and minority-spin. The majority-spin of Co is similar to Cu with dispersive *sp* band at the Fermi level, allowing for highly conductive channel when interfacing with Cu. Minority-spin of Co which has *d* band at the Fermi level instead, resulting in lower conductivity of this conduction channel. This conduction asymmetry between majority- and minority-spin conduction of Co at the interface is one of the main reasons for large MR ratio in Co/Cu multilayers. In the case of Fe/Cr, it works the opposite way where only the minority-spin of Fe is the one that band is matched with Cr creating conduction asymmetry similar to Co/Cu system. When the pairs are swapped, the matching between FM and NM layers does not exist, thus the lower MR ratio. The second important factor is high lattice matching which are shown between Co and Cu with <2% lattice matching in face-centered cubic (fcc) structure as well as between Fe and Cr with <1% lattice matching in their body-centered cubic (bcc) structure[35].

1.3.3 Effect of layer thicknesses in CIP-GMR

In optimizing the CIP-GMR spin valve device, all layer thicknesses can directly affect the MR ratio of the device. Due to the in-plane current flow of CIP-GMR, any conductive channel which does not positively contributes to spin-dependent scattering will decrease MR ratio. NM spacer is used in the CIP-GMR SV structure to magnetically separate FM layers. If it is too thin, ferromagnetic interlayer exchange coupling between FM layers will happen and prevent the individual magnetic switching, resulting in no antiparallel state. The scattering inside the bulk of NM layer is spin-independent, therefore if it is too thick current shunting through the spacer will happen and MR ratio will be reduced as a result as shown in Figure 1.6(a). Another thing that can also happen is with wider spacer region, electron is more likely to be scattered before entering the opposite FM layer, which does not generate GMR either. This effect phenomenologically can be expressed as[35,45]:

$$\frac{\Delta R}{R} = \left(\frac{\Delta R}{R}\right)_0 \frac{\exp(-d_{NM}/l_{NM})}{(1 + d_{NM}/d_0)}$$

Numerator part is related to the probability of electron to cross through (escape) the NM spacer. The more spacer can allow electron to pass through without experiencing scattering, the larger the MR ratio will be. The denominator represents the shunting effect. d_{NM} is the thickness of the NM layer whereas l_{NM} is related to mean-free path in NM layer, λ_{NM}. This is reflected in Figure 1.6(a) where Au (λ_{Au} = 8.5 nm) which has shorter mean-free path compared to Cu (λ_{Cu} = 11.5 nm)[35], also have lower MR ratio in comparison.

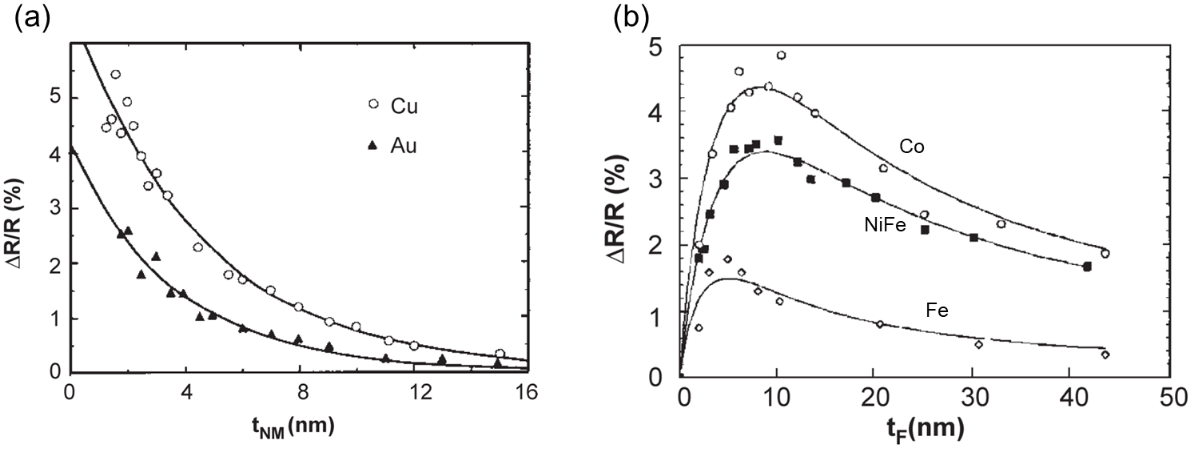

Figure 1.6 (a) Nonmagnetic thickness dependence of MR ratio for Co(7 nm)/NM(t_{NM})/NiFe(5 nm)/FeMn(8 nm)/NM(1.5 nm). Ferromagnetic thickness dependence of MR ratio for F(t_F)/Cu(2.5 nm)/NiFe(5 nm)/FeMn(10 nm) with F = NiFe, Co and Fe [35,45].

Ferromagnetic layer thickness is affecting the MR ratio as seen in Figure 1.6(b). Because bulk region of FM layer also contributes to spin-dependent scattering, increasing the thickness of this layer can improve MR ratio. However, if the FM layer is thicker than its spin-diffusion length current shunting will start to dominate, thus reducing MR ratio. Phenomenological expression can be written as well for this layer[35,45].

$$\frac{\Delta R}{R} = \left(\frac{\Delta R}{R}\right)_0 \frac{1 - \exp(-d_{FM}/l_{FM})}{(1 + d_{FM}/d_0)}$$

Similar to NM spacer layer, the denominator part represents the shunting of the current inside FM layer which responsible for the decrease at large thickness. The numerator however is related to the probability of electron coming from other FM layer to be scattered inside the FM layer. d_{FM} is the thickness of the NM layer whereas l_{FM} is a value which is related to mean-free path in FM layer, λ_{FM}.

1.3.4 Effect of specular reflection in CIP-GMR

In CIP-GMR, electron moves parallel in respect to the interfaces of the multilayer with some perpendicular component. During the transport when spin-polarized electron reaches the outer boundary of the GMR, i.e. AFM layer or seed layer, two things are possible to happen. If the outer boundary allows for further conduction, electron will continue its path and its spin is randomized, reducing MR ratio. Other possibility may occur in which electron is specularly reflected back into the FM layer retaining its momentum and spin. This specular reflection generally increases the MR ratio of CIP-GMR device. Figure 1.7 shows that spin valve devices with more specular reflective layer has its MR ratio increased compared to the one without[46]. Of course, it is important to control so the specular layer does not magnetically interfere with the main FM/NM/FM part of the GMR. Specular layer can be applied by depositing oxide layer or oxidize part of the FM layer[34,47–51].

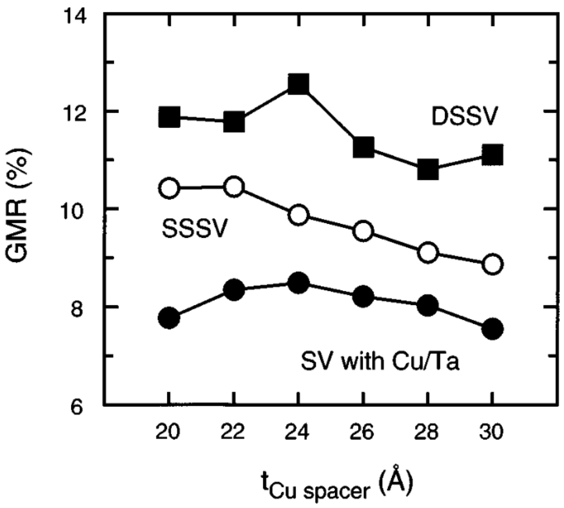

Figure 1.7 Cu thickness dependence of MR ratio for PdPtMn/CoFeB/Ru/CoFeB(B)/Cu/CoFeB(A). SSSV stands for single specular spin valve with oxide layer embedded into CoFeB(A). DSSV stands for dual specular spin valve with oxide layer embedded into both CoFeB(A) and CoFeB(B)[46].

1.4. Materials selection in this thesis

Wide range of FM and NM materials are available to be used in CIP-GMR. In this thesis, materials are selected considering the band and lattice matching between FM and NM layers. Additionally, its performance from past research is also accounted for consideration.

1.4.1 Heusler alloy ferromagnets

Heusler alloy was discovered in 1903 by Friedrich Heusler. These alloys have general composition of X_2YZ (X,Y = Co, Fe, Ni or Mn and Z = Si, Al, Ge, etc.). Structure of Heusler alloy with perfect L21 (space group Fm-3m) atomic ordering is depicted in Figure 1.8.

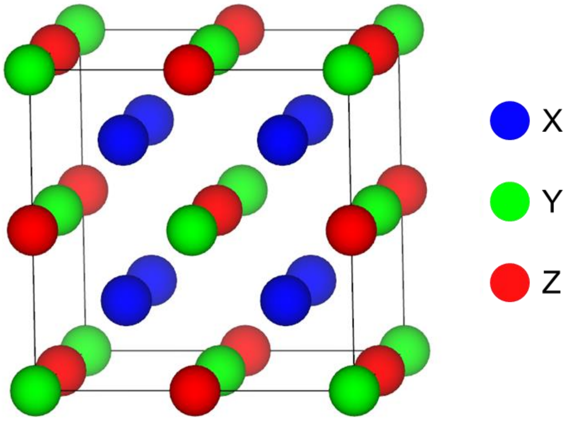

Figure 1.8 Diagram of $L2_1$ (Fm-3m) atomic ordered Heusler alloys.

Order-disorder transition is important properties to notice in Heusler alloy. Disordered structure gives different properties than the ordered structure, therefore understanding how to control this transition is necessary. In the thin film state, Heusler alloy often forms disordered A2 (space group Im-3m) which gradually improves to partially ordered B2 (space group Pm-3m) or fully-ordered L2$_1$ structure upon given thermal treatment. For example, Heusler compound Co_2FeAl thin film is reported to show transition from A2 to B2 structure after annealing above 200°C and to L2$_1$ structure after 500°C[52].

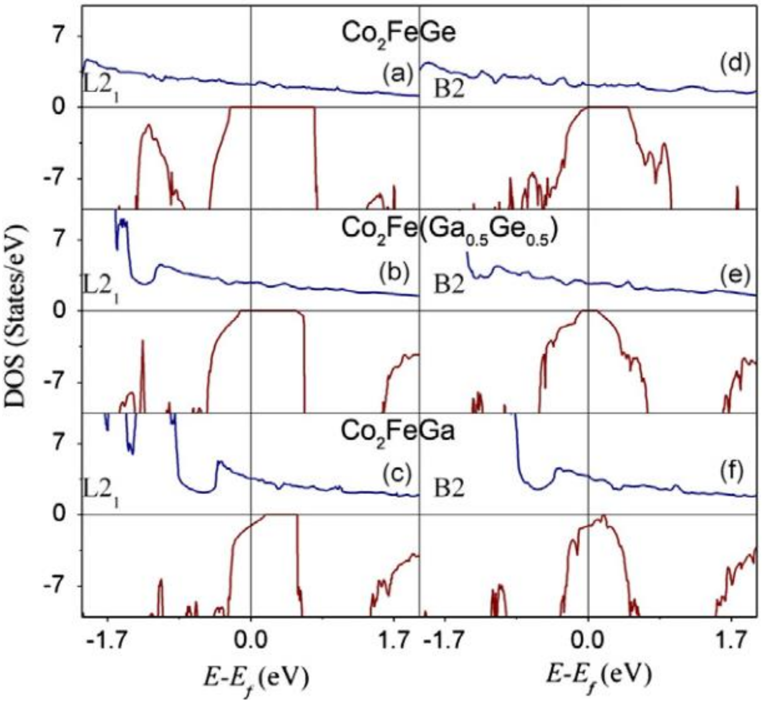

Figure 1.9 Calculated density of states (DOS) of Co_2FeGe, $Co_2FeGa_{0.5}Ge_{0.5}$ and Co2FeGa near Fermi level for L2$_1$ and B2 structures[53].

Some Heusler alloys are predicted and experimentally proven to exhibit half-metallic properties in which the spin polarization is so high that only one spin direction can flow through[54,55,64,56–63]. It is indicated by the appearance of electronic state in one spin direction but not the others. Figure 1.9 shows the density of states (DOS) of Co_2FeGe, $Co_2FeGa_{0.5}Ge_{0.5}$ (CFGG) and Co_2FeGa with L2$_1$ and B2 structures close to the Fermi level[53]. The DOS of Co_2FeGe shows half-metallic properties on both L2$_1$ and B2 structures indicated by the existing states for its majority-spin but not for minority-spin at Fermi level. For the B2 structure of Co_2FeGe, the upper part of the valence band is very close to the Fermi which suggests the possibility of existing minority-spin state at finite temperateure, effectively reducing spin polarization. By mixing with Co_2FeGa, Fermi level shifts to the middle of the minority-spin band gap for both L2$_1$ and B2 structure which lead to high spin polarization of both structures even at room temperature. This properties resulting in large MR ratio in CFGG-based CPP-GMR device. Epitaxial CPP-GMR device with CFGG and Ag as FM and NM layers respectively can achieve up to 57% MR ratio at RT[65]. Improved version using NiAl at the CFGG/Ag interface enhance the MR ratio further up to 77% at RT[66]. Not only with CFGG, other Heusler alloy with similar properties also show excellent result in CPP-GMR devices[67–72]. For example, epitaxially grown $Co_2FeAl_{0.5}Si_{0.5}$ in pseudo spin valve type CPP-GMR with Ag layer as spacer exhibit MR ratio of 34% and at RT[73]. All of this is possible due to CFGG/CFAS having large spin polarization as well as high lattice and band matching to their spacer[66,74,75]. It is also possible to utilize this material combination showing high lattice and band matching in CIP-GMR to achieve large MR ratio.

In the past, some Heusler alloy were reported for CIP-GMR. However, the MR ratio is generally very low, and the reason is not well understood. Half Heusler NiMnSb-based spin valve with Mo and Cu spacer was reported to show MR ratio of 1.2%[76] and 0.2%[77]. Pseudo spin-valve using full Heusler Co_2FeAl shows MR ratio less than 0.03% at room temperature with drastic enhancement of MR ratio up to 5.84% by introducing specular reflection effect via thin nano-oxide layer at the outer boundary[78].

1.4.2 Co-Fe-Ni alloy ferromagnets

The discovery of GMR effects start with two pairs of material combinations, Fe/Cr and Co/Cu[3,4]. This combination of materials stays as having largest MR ratio in giant magnetic type CIP-GMR structure. Several other combinations of materials were reported to show large MR ratio as well such as Co/Ag, $Ni_{80}Fe_{20}$/Cu, $Ni_{80}Fe_{20}$/Cu and $Ni_{80}Fe_{20}$/Ag[35].

In the earliest discovery of spin valve type CIP-GMR device, $Ni_{80}Fe_{20}$ was used as the FM material[17,79,80]. This material has several benefit. First, are the soft magnetic properties of the $Ni_{80}Fe_{20}$. The purpose of making spin valve type is reducing the required external field to switch the magnetization configuration of the device from antiparallel to parallel direction. Therefore, having soft magnetic properties greatly reduce this requirement. Next one is the immiscibility to its spacer. $Ni_{80}Fe_{20}$ usually used together with Cu as the spacer. Immiscible Ni80Fe20 ensure that intermixing between FM and NM layers does not happen. Intermixing could produce point defects, magnetically dead layer, rough interfaces and many other problems which could be avoided by selecting immiscible materials. Finally, $Ni_{80}Fe_{20}$ has good lattice matching to its Cu spacer which resulting in decent MR ratio value of this material combination.

Other commonly used FM material for CIP-GMR is fcc-CoFe, specifically $Co_{90}Fe_{10}$. Almost all reportedly large MR ratio uses $Co_{90}Fe_{10}$ in combination with Cu as its spacer. Similar to $Ni_{80}Fe_{20}$, soft magnetic properties of $Co_{90}Fe_{10}$ are very suitable to be used in CIP-GMR spin valve. Unlike $Ni_{80}Fe_{20}$ which can only show MR ratio <10% on its own, $Co_{90}Fe_{10}$ reportedly show MR ratio up to 27% at RT[33]. Usually fcc-$Co_{90}Fe_{10}$ is used as an alloy mix or as part of composite FM layer in spin valve multilayer[35,81–87].

It was previously mentioned that one of the most important factors determining the MR ratio is lattice matching. The fcc Co and fcc Co-Fe alloys have high lattice matching to fcc-Cu, resulting in large MR ratio. Co/Cu/Co/NiO was reported showing MR ratio of 20% at room temperature[88,89]. In order to reduce hysteresis, fcc Ni-rich Ni-Fe alloy such as $Ni_{80}Fe_{20}$ is often used as free layer due to high lattice matching to Cu spacer. On itself, $Ni_{80}Fe_{20}$ show lower MR ratio for <10%[79,80]. However, with by making the free layer as composite with Co, Co-Fe or Co-Fe-Ni alloys interfacing with Cu spacer, large MR ratio can be maintained while having low coercivity[49,49,81,86,90]. Therefore, these materials are potential to achieve even larger MR ratio in CIP-GMR. Along the spectrum of Co-Fe alloys, stable bcc phase is also exists for Fe composition >30% which might come into consideration as well[91].

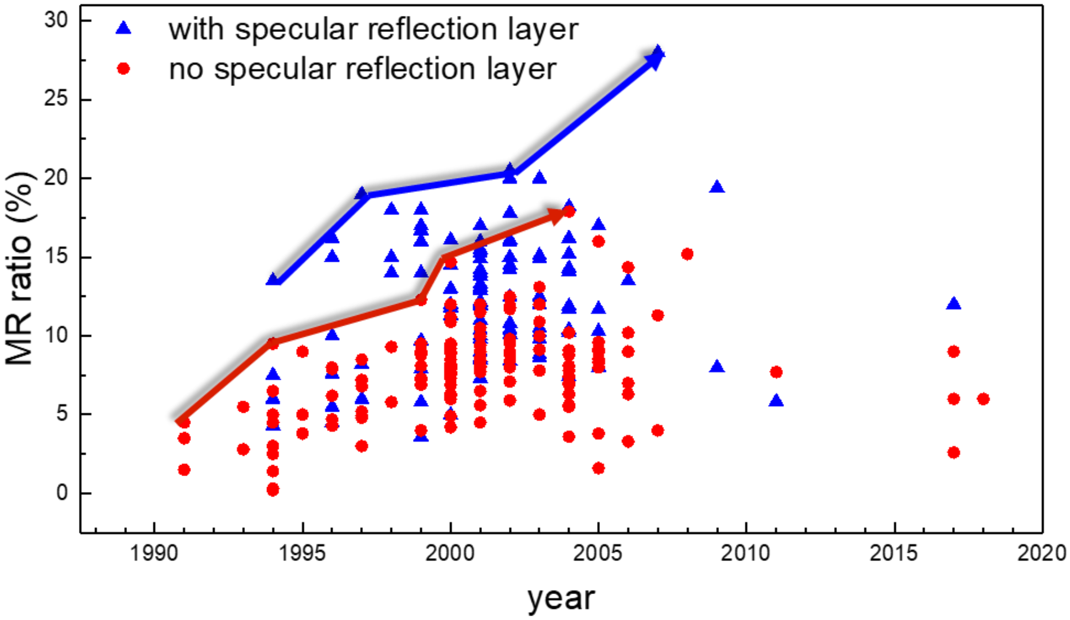

Figure 1.10 MR ratio of CIP-GMR spin valves with and without specular reflection layers over the years. Guideline emphasis progression of the largest MR ratio.

1.5. Outline

This thesis aiming for pushing the limit of CIP-GMR sensor in which the materials development towards larger MR output has been dormant for more than 15 years as shown in Figure 1.10. In order to satisfy the need for magnetic sensor with high sensitivity and lower detectivity, the MR ratio of CIP-GMR device need to be increased further. In this thesis pairs of FM and NM materials showing high lattice and band matching are selected. After evaluating their properties, structural analysis and theoretical calculations were performed for deeper understanding.

Chapter 1 starts with the overview of spintronics and its application in magnetic sensors. The historical development of CIP-GMR spin valve and how the improvements were approach are described. Materials that were thought to have potential in CIP-GMR are also mentioned.

In chapter 2, the methods used for sample preparation and characterization are also briefly described.

In chapter 3, an initial approach by choosing highly spin-polarized $Co_2FeAl_{0.5}Si_{0.5}$ (CFAS) Heusler alloy as FM layer and Ag as NM spacer layer in an epitaxially grown spin valve is described. For comparison, similar multilayer was also fabricated using conventional $Co_{50}Fe_{50}$ alloy as FM layer. Spin valve with CFAS/Ag show low MR ratio value which deny initial expectation as they have high lattice and band matching. Moreover, CoFe/Ag spin valve which show inferior band matching show larger MR ratio. It is then revealed that the large resistivity of CFAS limits the potential of CFAS in CIP-GMR devices and become the reason for poor MR ratio, underlining the important of taking account resistivity as a factor to achieve large MR ratio.

In chapter 4, systematic study on the epitaxially grown CIP-GMR spin valves using Co-Fe alloys with various compositions as FM layers is described. In this case, Cu was selected as the spacer due to historically showing large MR ratio in combination with Co-Fe alloys. The bcc-$Co_{50}Fe_{50}$ shows largest MR ratio compared to other Co-Fe alloy compositions with maximum value of 26.5%; larger than previous record value in CIP-GMR spin valve of 15%[83]. Structural analysis reveals the formation of metastable bcc-Cu which mimic the structure of its surrounding bcc-$Co_{50}Fe_{50}$, allowing for perfect lattice matching with bcc-$Co_{50}Fe_{50}$. First-principles calculation show large spin-dependent transport at bcc-$Co_{50}Fe_{50}$/bcc-Cu interfaces due to the high band matching. Although large MR ratio has been obtained, several problems regarding bcc-$Co_{50}Fe_{50}$/bcc-Cu-based CIP-GMR are noticed. Firstly, the free layer of bcc-$Co_{50}Fe_{50}$/bcc-Cu-based CIP-GMR exhibit large coercivity which will reduce its accuracy as a sensor. Secondly, the epitaxial growth of this device was achieved using MgO substrate which is impractical for commercial use.

In chapter 5, an attempt to reduce the coercivity by alloying $Co_{50}Fe_{50}$ with Ni is described. Large reduction of coercivity is demonstrated at the cost of MR ratio value. Systematical structural analysis reveals crystal structure degradation of the Cu spacer with each addition of Ni. First-principles calculation also suggests the reduction of band matching.

In chapter 6, an attempt to fabricate epitaxial bcc-$Co_{50}Fe_{50}$/bcc-Cu-based CIP-GMR spin valve using industrially viable Si substrate is described. With the use of NiAl underlayer, epitaxial growth of $Co_{50}Fe_{50}$ is observed although not perfect. Structural analysis suggests the formation of additional phase other than bcc-Cu which negatively impact the MR ratio.

Finally, chapter 7 summarize all the works reported within this thesis.

Chapter 2: Experimental method

2.1. Sputter deposition

Sputter deposition or sputtering is one of the most used processes for thin film manufacturing due to its flexibility depositing various kind of materials and its large yield. Almost all thin film sample in this article were fabricated by this process. Sputtering uses energetic particles which will collide to source material, commonly called target. Surface atoms of the target then are scattered due to the collision and get deposited onto the substrate. Targets can be in the form of metals, alloys, semiconductors, or insulators. The energetic particles usually generated by ionizing gas such as Ar which under electric field will be accelerated towards the cathode target. Reactive gases such as O_2 or N_2 can also be used instead to produce oxide or nitride compounds.

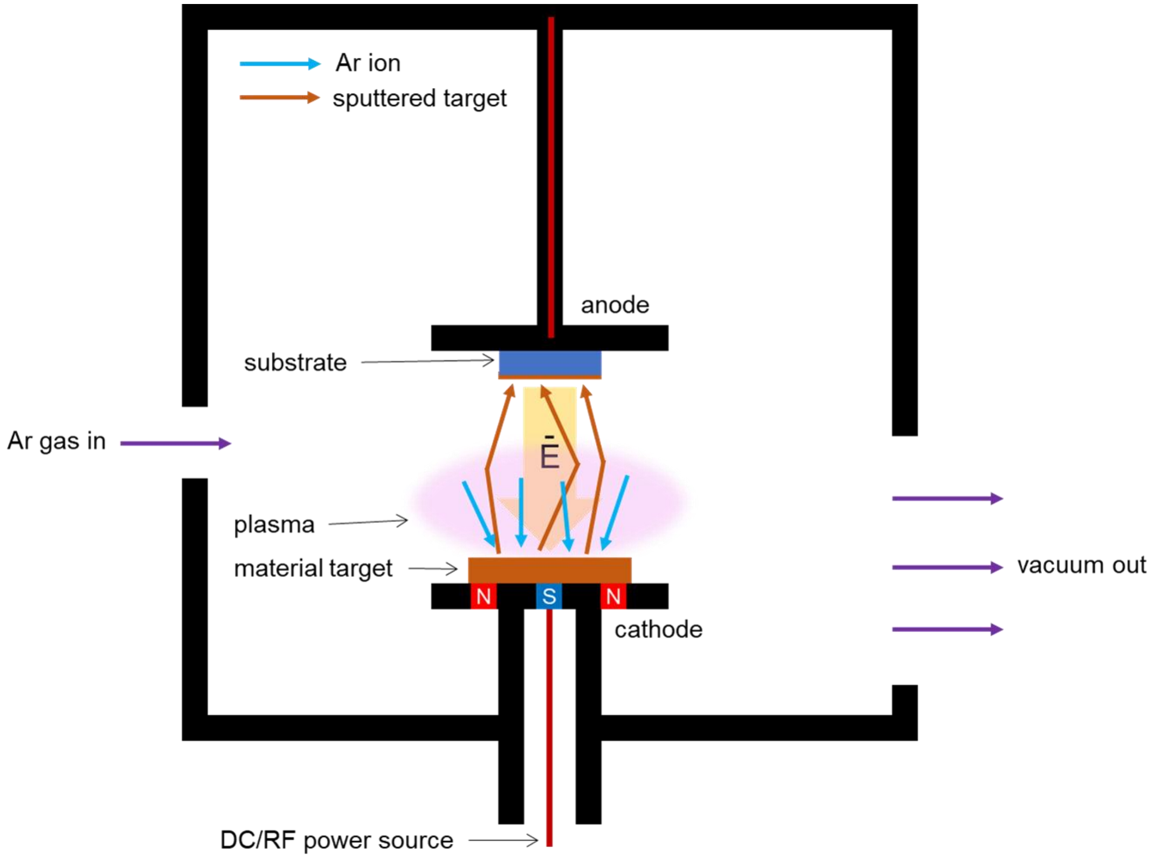

Figure 2.1 Schematic illustration of thin film fabrication by sputter deposition.

Magnetron sputtering system is an enhanced sputtering system which utilize permanent magnet near the cathode which is oriented in such way so that drifting electrons can be controlled to create a closed-loop. This effect increases the collision rate between electrons and sputtering gas further increasing sputter yield. Figure 2.1 illustrate basic sputter deposition. Ionized Ar ion generated due to the collision with electron, then accelerated by electric field towards material target. As the Ar ion hit material target, it transfers its momentum and sputter out the target atoms which will be deposited on the substrate above.

To create thin film with various composition, rather than changing target for each one, another system called co-sputter is used. In the co-sputter system, two or more targets can be deposited at once. Because deposition rate depends on the power used to accelerate ionic gas particles, the composition can be tuned by varying the power. To achieve more uniform deposition and to avoid contamination between targets, the distance between substrate and targets needs to be increased, thus the deposition rate in this system is much slower.

2.2. Microfabrication

To evaluate its electronic properties, thin film materials need to be transformed into devices with predetermined pattern. In this article, the devices are in the form of ribbons/strips with metallic contact at the end. The process involves several steps: coating thin film with photosensitive photoresist, patterning the photoresist using optical lithography, etch the thin film or deposit required layer outside the masked area and finally clean the photosensitive photoresist.

2.2.1. Optical Lithography

The optical lithography process utilizes the unique properties of photoresist which respond to light and become easier (for positive resist) or harder (negative resist) to remove. As illustrated in Figure 2.2, the process involves several steps including the coating of the photoresist, the exposure by high intensity UV light using predetermined pattern and the development of the pattern on the photoresist using developing agent. Pattern can be prepared using hard mask to prevent areas being exposed to light or by using optical scanning system exposing the pattern by pixel. After the development process, positive resist exposed area will be removed, for negative resist it will be retained instead. Once the pattern is ready, then deposition or etching can be performed depending on the needs. In this study, positive resist AZ5214E and negative resist ZPN1150 are used.

2.2.2. Ion etching

For common materials used in this study such as metals and oxides, physical dry etching method such as ion etching is commonly used. Like sputtering process, this method uses accelerated Ar ion to force atoms to be dislodged. However, instead of capturing sputtered target on a substrate, the film on the substrate itself is sputtered instead. This method can etch the film surface with etching rate depending on the materials. Rate and angle of the etching can also be controlled by changing the power used and the angle of the film in respect to the beam source.

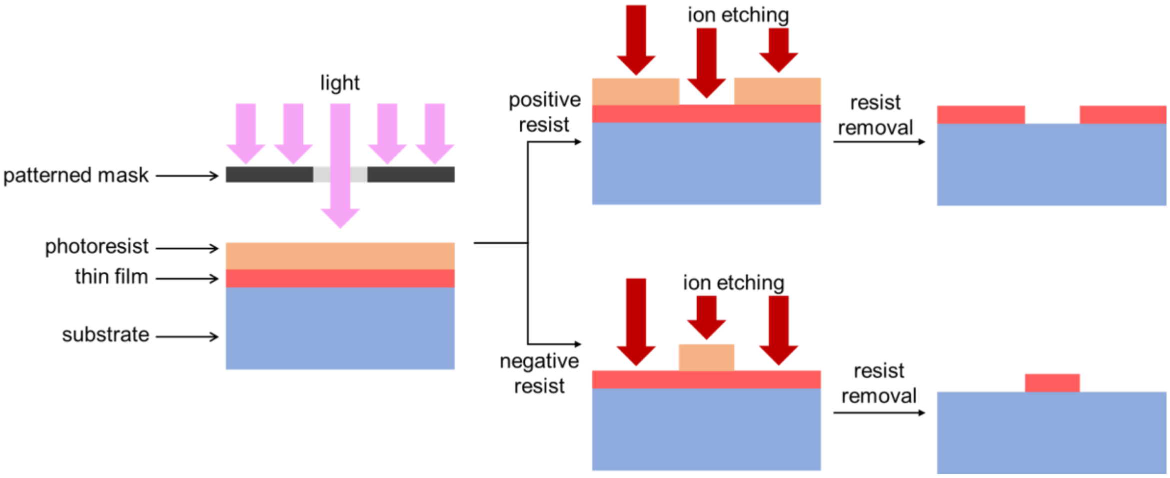

Figure 2.2 Flow diagram of optical lithography and ion etching. Pattern from the mask can be transferred into film using either positive or negative photoresist.

2.3. Electric and magnetic properties characterization

2.3.1. Vibrating-sample magnetometer (VSM)

Vibrating-sample magnetometer is a very useful and versatile tool to measure magnetization of a sample under sweeping magnetic field. As illustrated in Figure 2.3, a sample is put under uniform magnetic field and then vibrated perpendicularly in respect to the field. The moments of the sample create magnetic field which change as it is vibrating. This creates electric field which will be detected by the pickup coil and then measured. In this study, the result of magnetization measurements is used to analyze how the CIP-GMR device responds under magnetic field, especially during electrical measurements.

2.3.2. DC four-point probe

DC four-point probe method is used in this study to measure magneto-transport properties of CIP-GMR devices. After microfabrication, the CIP-GMR film will be in the form of thin strips with several contact points. These contact point then connected to probing device to be measured. The measurement is conducted with the device placed between electromagnets which generate external magnetic field. The current is injected through the device and then measured its resistance at any given field.

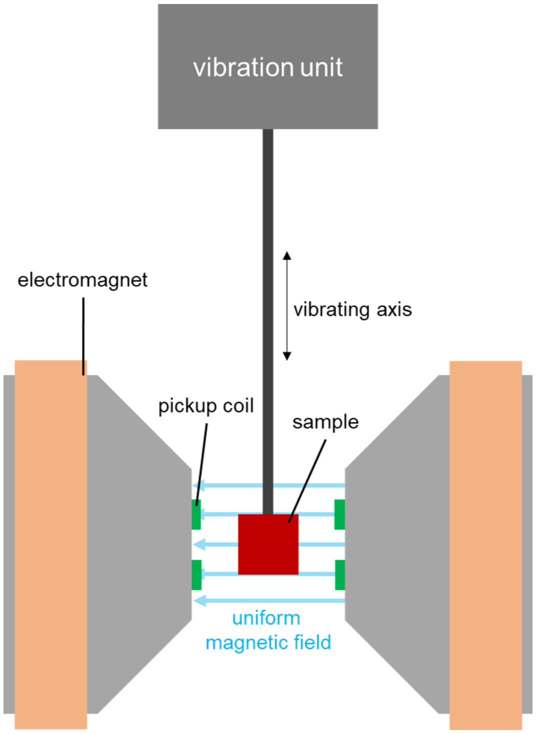

Figure 2.3 Schematics diagram of vibrating-sample magnetometer. Sample can be placed in-plane or out-of-plane towards magnetic field.

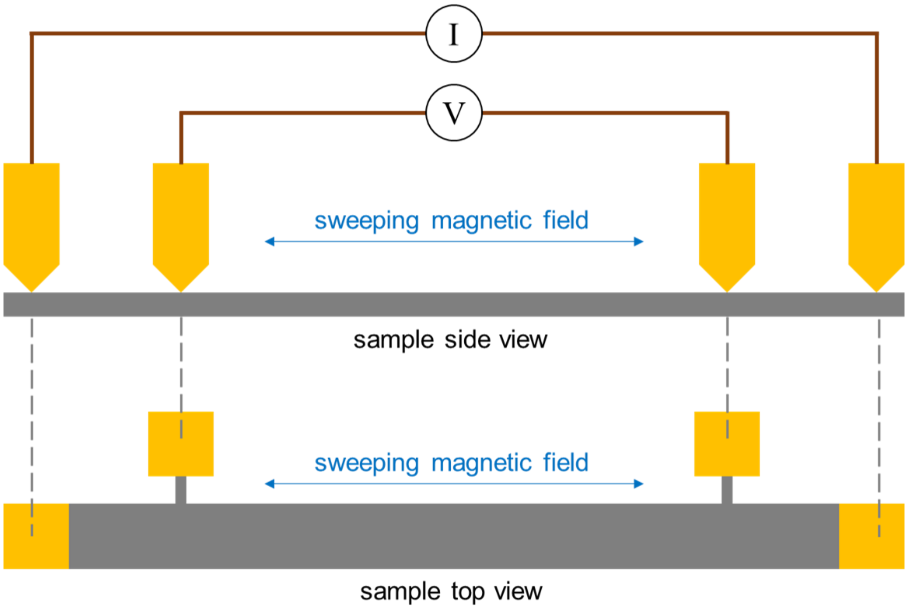

Figure 2.4 Schematics of four-point probe measurement. Current is passing through the sample and its resistance is measured while external magnetic field is swept from saturation state of the sample.

2.4. Structural properties characterization

2.4.1. Reflective high-energy electron diffraction (RHEED)

RHEED technique is performed by emitting high-energy electron beam towards the surface of a film so that diffraction pattern can be observed, usually on photoluminescent screen or CCD camera. The resulting diffraction can give several information such as crystal growth, crystallographic orientation, and surface roughness. Because the angle of the electron incident is shallow, this method is surface sensitive. This analysis needs high vacuum condition to avoid interference by gas molecules/atoms. In this study, RHEED is located inside the sputter deposition chamber and used after deposition of a material to check how the material grows. The schematic of RHEED setup can be seen in Figure 2.5.

2.4.2. X-ray diffraction (XRD)

XRD is a technique to identify crystal phase of a material and can also be used to measure lattice dimension. The X-ray beam generated from the source is beamed towards the sample. Then when the angle of the incident beam satisfies Bragg's Law ($n\lambda = 2dsin(\theta)$) the sample will produce constructive interference and X-ray can be detected. Out of plane XRD was used in this study with setup as seen in Figure 2.6. The XRD machine use Cu source X-ray with wavelength 1.54 Å. The detector can be changed from zero-dimensional (0D) to two-dimensional (2D) detector vice versa depending on the needs. The 2D detector has the benefit to include additional information such as diffraction from different angle at once during measurement at the cost of less sensitivity compared to 0D.

2.4.3. Transmission electron microscope (TEM)

Transmission electron microscope is a microscope which use electron beam instead of light which is beamed at the sample and take its transmitted electrons to visualize the sample. This analysis is done in high vacuum condition. Due to relying on transmitted electron passing through the sample, thin specimen ~100 nm is typically needed. In this study the TEM specimen is prepared by focused ion beam (FIB) to produce thin cross-section TEM specimen. Depending on the mode and the detector used in TEM, various information such as crystal structures, atomic resolution images, and individual composing elements.

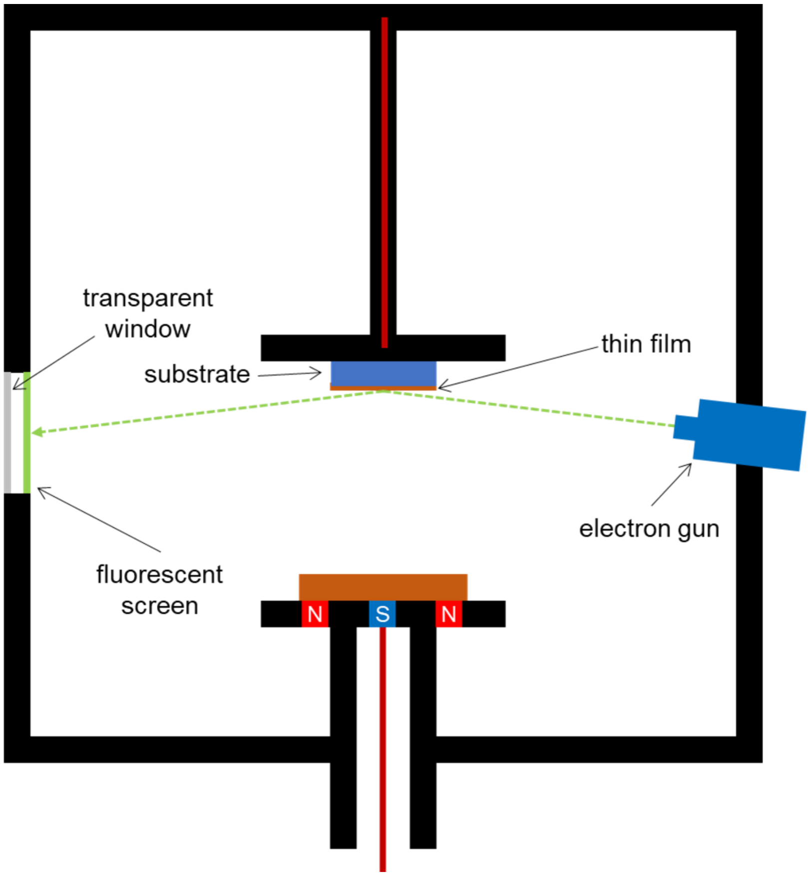

Figure 2.5 Schematic diagram for the RHEED setup located in the sputter deposition chamber.

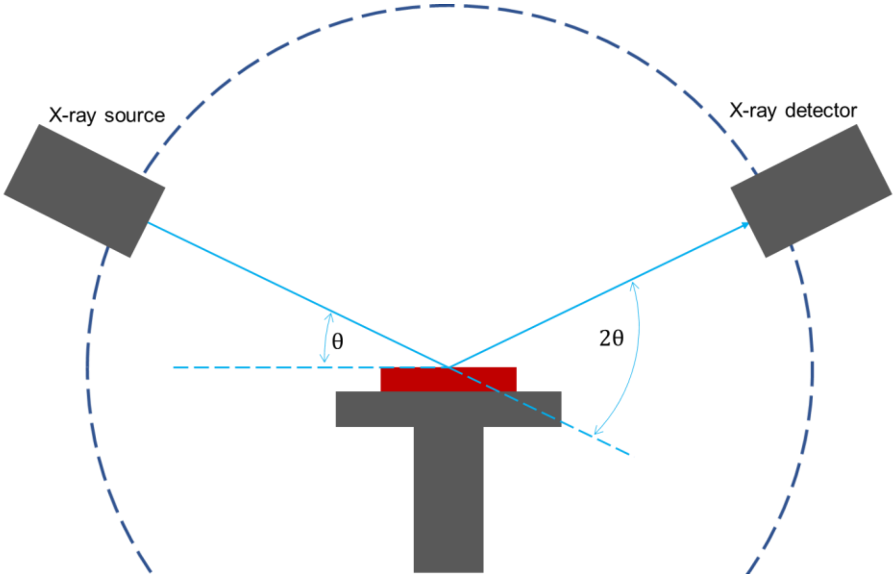

Figure 2.6 Schematic diagram of X-ray diffraction machine measuring from out-of-plane direction.

Chapter 3: Epitaxial current-in-plane giant magnetoresistance using $Co_2FeAl_{0.5}Si_{0.5}$ Heusler alloy

Spin dependent scattering is the origin of CIP-GMR. With larger spin polarization of an FM materials, more spin-polarized current can be generated. Thus, spin dependent scattering will occurs more often and MR ratio can be improved. Therefore, exchanging the FM materials into the one having larger spin polarization is a viable strategy to achieve larger MR ratio in CIP-GMR. Ferromagnetic material with large spin polarization means that the material has large density of state (DOS) at the Fermi level for one spin direction but very low DOS for the opposite spin. One class of material has many of its members were predicted to have large spin polarization, that is Heusler alloy[1,92]. Co-based Heusler alloy have attracted research interests for many spintronics application such as in tunnel magnetoresistance (TMR)[52,93] or current-perpendicular to plane (CPP)-GMR[66,74,75,94] devices.

There are also studies on the CIP-GMR devices using half-metallic Heusler alloy. For example, polycrystalline pseudo spin-valve (PSV) type CIP-GMR device Co_2FeAl/Cu/Co_2FeAl with specularly reflective nano oxide layer shows MR ratio up to 5.84% at room temperature[95]. Other devices such as Half Heusler NiMnSb-based spin valve (SV) with Mo and Cu spacer was reported to show MR ratio of 1.2%[76] and 0.2%[77] respectively at RT. Although these Heusler electrodes are expected to exhibit large bulk spin polarization, the MR ratio performances is much poorer than the devices with conventional alloys such as polycrystalline $Co_{90}Fe_{10}$ which shows MR ratio up to 25% at room temperature[33]. High lattice and band matching is required to obtain large MR ratio. However, in previous studies on Heusler alloy-based CIP-GMR device, above-mentioned two important issues, i.e., electronic band and lattice matchings at the Heusler/NM interfaces have not been carefully considered.

In this chapter, Heusler alloy with large spin polarization are used to increase MR ratio in CIP-GMR devices. Unlike previous studies in the past, in this study we want to start the selection of the materials considering the lattice and band matching. As for the options, $Co_2FeGa_{0.5}Ge_{0.5}$ (CFGG) was strongly considered. This material exhibits large spin polarization at RT[61]. When combined with Ag spacer, due to excellent lattice and band matching, MR ratio of CFGG in CPP-GMR device is very high, over 30% at RT[65]. Furthermore, by introducing NiAl at the CFGG/Ag interfaces, MR ratio can be improved further to over 80% at RT[66]. $Co_2FeAl_{0.5}Si_{0.5}$ (CFAS) is also considered due to exhibiting large spin polarization of 0.60 measured by point contact Andreev reflection method[96]. Large spin polarization in CFAS allows for high bulk spin asymmetry which reflected in the large MR ratio obtained in current-perpendicular-to-plane giant magnetoresistance (CPP-GMR) devices [68,69,74,75]. In addition, the use of Ag spacer adds large interfacial spin asymmetry due to having high lattice and band matching to CFAS which also contributes to the MR.

In this section, the performance of CIP-GMR device using CFAS as FM and Ag as NM spacer layers is described. Even though uncommon to use Ag in CIP-GMR structure, Ag was reportedly has better interface to CFAS compared to Cu which arguably will result in better MR ratio[97]. Epitaxial system is selected to realize ordered structure more easily, therefore single crystal MgO (001) substrate was used. For comparison, another spin valve device with $Co_{50}Fe_{50}$ (CoFe), a simpler alloy, as FM layer was also investigated to see the effect of increased spin polarization. In CIP-GMR, because any additional conductive layer negatively impacts MR ratio, any metallic buffer which was used in previous study of CFAS-based CPP-GMR was not implemented in this study. Structural and first-principles analysis was performed to understand the transport properties in the samples.

3.1. Experiments and Results

As described earlier, $Co_2FeGa_{0.5}Ge_{0.5}$ (CFGG) and $Co_2FeAl_{0.5}Si_{0.5}$ (CFAS) has good lattice and band matching to Ag that would be beneficial to be used in CIP-GMR spin valve with Ag as the spacer. Between these two materials, only CFAS shows proper CIP-GMR spin valve type response. Therefore, CFAS Heusler alloy–based CIP-GMR is discussed but not for CFGG. Thus, in this study a CFAS–based spin valve device with the structure of CFAS(6 nm)/Ag(3 nm)/CFAS(t_{CFAS})/CoFe(1 nm)/IrMn(8 nm)/Ta(3 nm) were fabricated. The composition of CFAS used is nearly stoichiometric (Co:Fe:Al:Si=50.83:25.55:12.50:11.12). Alongside this device, CoFe–based with the structure of CoFe(9.5 nm)/Ag(2.5 nm)/CoFe(t_{CoFe})/IrMn(6 nm)/Ta(3 nm) was fabricated as well. CoFe (50:50) is used as FM layer as this material has good lattice matching to Ag, similar with CFAS. This material is also good showcase to compare how spin polarization will affect GMR ratio, because CoFe has lower spin polarization compared to CFAS. The top FM thicknesses were varied with t_{CoFe}=2-10 nm and t_{CFAS}=0-8 nm. All samples are deposited on single crystal MgO(001) to obtain epitaxial growth. They will be referred as CoFe/Ag and CFAS/Ag spin valve (SV)s from here on. All deposition was done at room temperature (RT). For CFAS/Ag SV, in-situ annealing was done at 500°C just after the deposition of upper CFAS layer to achieve chemical ordering. Post annealing was performed for both samples at 250°C for 1h under 3 kOe external field to apply exchange bias field from the IrMn layer to the top FM layer.

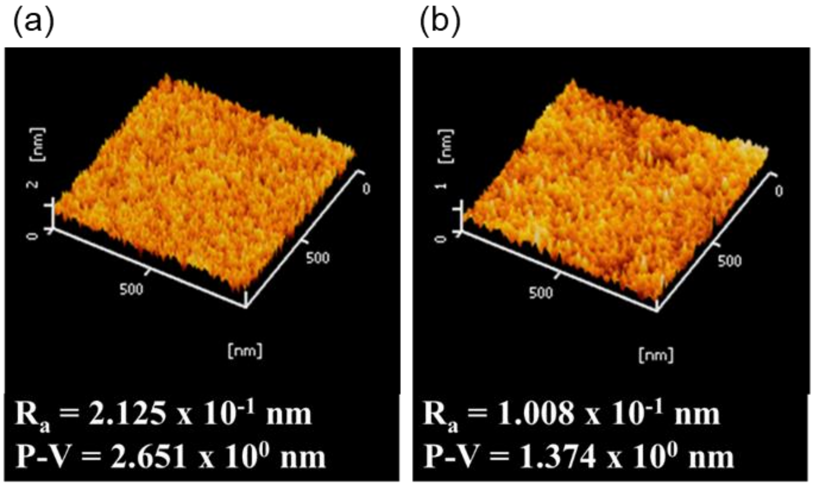

Figure 3.1 Averange surface roughness (R_a) and peak-to-valley value(P-V) for (a) CoFe/Ag and (b) CFAS/Ag spin valves measured by atomic force microscopy (AFM).

Interfacial roughness at the FM/NM interfaces is very important in CIP-GMR. Large interfacial roughness of this interface might introduce ferromagnetic coupling via orange peel mechanism[98] which resulting in the loss of MR effect. This is more worrying in CFAS/Ag spin valve as the large annealing temperature might add more mobility of the atoms leading to increased interfacial roughness which is common case[99]. Especially so because this sample is deposited without any buffer layers, common practice for depositing flat epitaxial Heusler thin films[70,100,101]. Figure 3.1 show the surface roughness of CoFe/Ag and CFAS/Ag measured by atomic force microscopy (AFM), which give some hint about the interfacial roughness at the FM/NM region. Roughness of both samples appears to be in the similar order. Surprisingly, the surface roughness of CFAS/Ag is lower compared to the CoFe/Ag. It is possible that the heat applied to CFAS/Ag helps flatten the surface instead of roughening it due to increased mobility of the atoms.

Microstructure of the spin valve devices is also important, especially in Heusler–based device. Crystal structures were analyzed by X-ray diffraction (XRD). Figure 3.2(a) shows the out of plane XRD patterns of the multilayer films. CoFe/Ag SV show 002 CoFe peak at 65.8° indicating (001)-oriented growth of this sample. Calculated from this peak resulting in lattice parameter of 2.84Å for CoFe layer. As for the Heusler alloy-based sample, it is important to identify the chemical ordering because it is heavily related to its properties. The degree of B2 ordering can be measured by comparing the intensity ratio of 002 and 004 peak of CFAS to the simulated ratio of perfect B2 order. CFAS/Ag SV show 004 peak and 002 superlattice peak at at 65.7° and 31.5°, respectively. I_{002}/I_{004} experimental to simulated ratio of CFAS/Ag SV is close to 1, indicating the complete B2 order of this film. Unfortunately, when CFAS/Ag were measured from <111> direction to observe 111 superlattice peak from $L2_1$ structure, no peak can be observed. It is concluded that L21 ordering was not achieved but complete B2 order is. Both samples also show 002 peak of IrMn which suggests the (001)-oriented growth of IrMn layer.

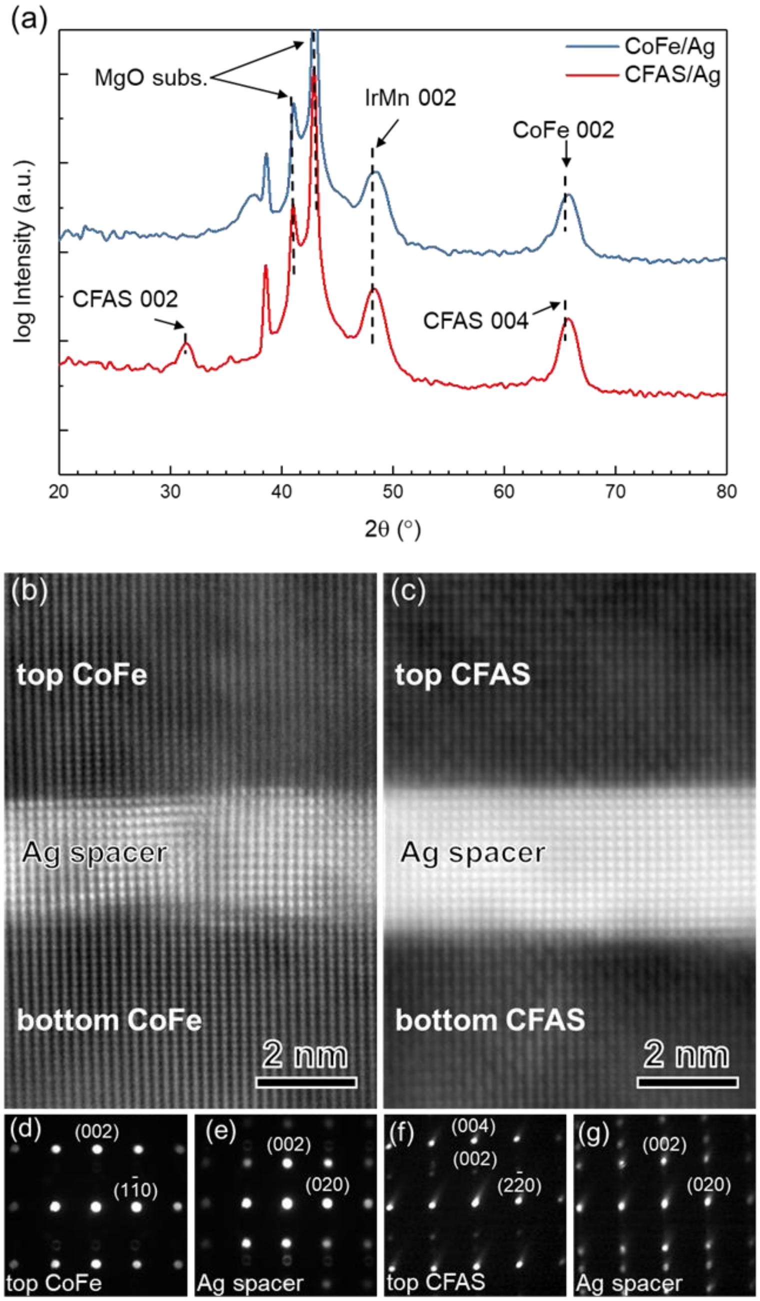

Figure 3.2 (a) Out of plane XRD graph for CoFe/Ag and CFAS/Ag SVs. HAADF-STEM images of (b) CoFe/Ag and (c) CFAS/Ag SVs with the electron diffraction pattern of (d) CoFe, (f) CFAS and (e and g) Ag layers.

Transmission electron microscope (TEM) image was also observed from both spin valve devices. Figure 3.2(b) and (c) show the HAADF-STEM image of CoFe/Ag and CFAS/Ag SVs taken from [110] zone axis of CoFe or CFAS layer. CoFe/Ag spin valve exhibit epitaxial growth even without applying high temperature annealing. B2 ordering of CoFe layer is difficult to observe due to the lack of contrast between Co and Fe atom in general. FM/NM interfaces of

CoFe/Ag spin valves are relatively smooth although some misfit dislocation can be observed caused by slight lattice mismatch between CoFe and Ag (~1.8% mismatch). Electron diffraction pattern of CoFe/Ag reveals that only single phase of bcc-CoFe and fcc-Ag was formed with the growth orientation between CoFe, and Ag is CoFe(001)[110]//Ag(001)[110]. Epitaxial growth of CFAS/Ag is also evident as seen in Figure 3.2(c) with visible columnar structures. The interface between CFAS and Ag appears to be atomically smooth with almost no misfit dislocation noticed. At this magnification CFAS/Ag seems smoother than CoFe/Ag which agrees with the result of the AFM measurement. We can consider that between CoFe/Ag and CFAS/Ag spin valves, no significant difference in growth quality and lattice matching exists.

Within the CFAS layer, alternating contrast can be seen between bright and dark which corresponds to Co and Fe/Al/Si layers respectively. The electron diffraction patterns confirm the XRD result with B2 structure of this layer. The lack of (111) reflections in the CFAS indicates the $L2_1$ ordered structure is not formed. The growth orientation between CFAS and Ag is CFAS(001)[110]//Ag(001)[110]. From above mentioned result, it is concluded that the crystal growth quality between CoFe/Ag and CFAS/Ag spin valves are similar. Because CFAS constitutes of four different elements, the ordering of the CFAS lattice affect the electronic properties of this alloy. Generally, $L2_1$ ordering is desired to get better properties from the Heusler layer, namely larger spin polarization. Mixing between Al or Si and Fe resulting in B2 structure which degrades the spin polarization. However, it was reported that the spin polarization of B2 ordered CFAS does not decrease too much compared to $L2_1$[96,102], therefore large spin polarization can still be expected even in the case of B2.

After annealing the sample at 250°C for 1h under 3 kOe external magnetic field, the GMR films were fabricated into sets of CIP-GMR spin valve device strips with the size of 200 μm × 3350 μm by photolithography and ion etching. Magnetotransport measurement was performed using four-point probe method after the patterning. Magnetic field was swept along the direction of the current. Figure 3.3 (a) show the variation of MR ratio as a function of FM thickness (t_{CoFe}, t_{CFAS}) from CoFe/Ag and CFAS/Ag SVs. CoFe/SV show increasing MR ratio as t_{CoFe} increases from 4.4 up to 8.4%. The general shape of this curve resemble the report from Dieny *et al.*[80] which argues that the increase of MR ratio is due to the decreased scattering of the majority-spin at the outer boundaries region. In this particular case, the outer region is CoFe/IrMn interface and bulk IrMn which has less spin scattering asymmetry compared to the bulk CoFe. With more CoFe thickness, electrons that are supposed to reach outer region will be scattered in the bulk of CoFe instead, thus increasing spin scattering contrast and increasing MR ratio. After t_{CoFe} reaches 9.5 nm, the reduction of MR ratio is observed. This decrease happens due to the shunting of the current in an area inside CoFe layer which does not get involved in GMR transport. Please note that GMR happen when spin-polarized electron from one FM layer pass through the other FM layer without any spin-flip. If the thickness of FM layer is larger than the mean free path of majority-spin, it will not contribute to GMR transport. Figure 3.3(b) shows the transfer curve of the CoFe/Ag spin valve for t_{CoFe}= 3, 5, 7, 9 and 9.7 nm. Antiparallel state can be observed from all thicknesses. Even at the largest thickness, the antiparallel state is well maintained. This also confirms that the reduction of MR ratio is not due to loss of antiparallel state but rather from shunting effect. Exchange bias strength of the CoFe layer decreases with the increase of t_{CoFe} which is common to be found in exchange-biased system as reported by Brown *et al*[103].

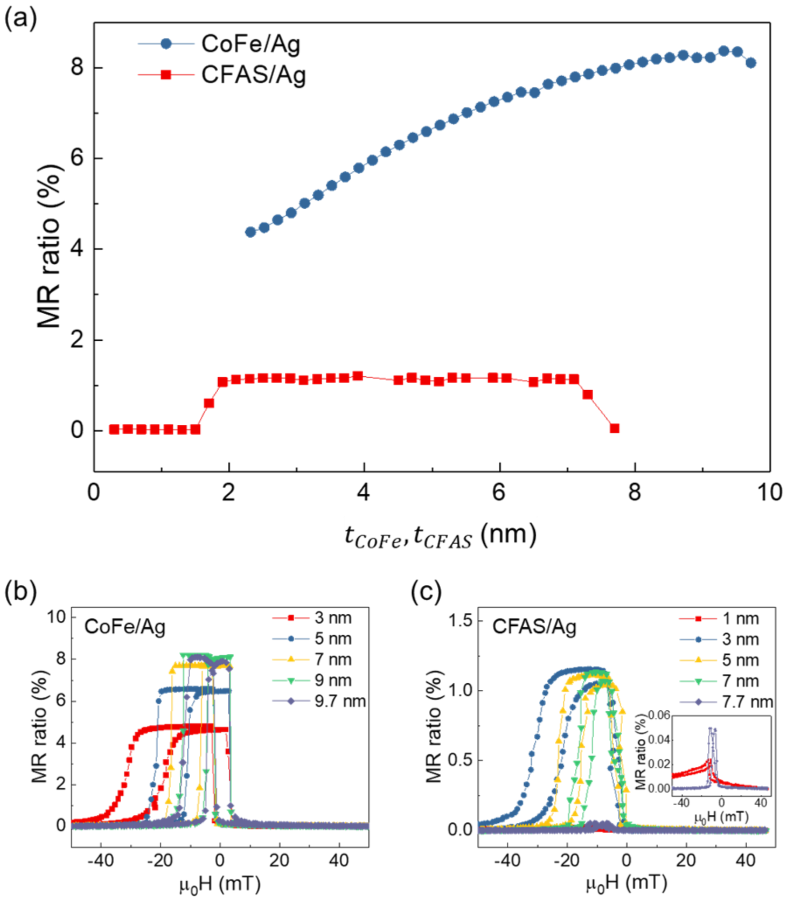

Figure 3.3 (a) Ferromagnetic thickness (t_{CoFe}, t_{CFAS}) dependence of MR ratio for CoFe/Ag and CFAS/Ag SVs and the magnetoresistance curves for select thicknesses (b-c).

In comparison, CFAS/Ag show much lower MR ratio with the maximum value of 1.2%. Interestingly, the way MR ratio changes with the function of t_{CFAS} is unique compared to CoFe/Ag or even spin valve device in general. MR ratio suddenly increases from almost zero to 1.2% at 2 nm and decreases again at 7 nm of t_{CFAS}. The poor MR ratio at low t_{CFAS} thickness could be explained by the poor quality of thin CFAS layer. In the early deposition stage at low thickness, deposition might not be homogeneous which impact the composition of CFAS, creating dead magnetic layer. Because this dead magnetic layer directly interfacing with Ag spacer, GMR cannot be obtained. Figure 3.3(c) shows the magnetoresistance transfer curve of CFAS/Ag spin valves for t_{CFAS} = 1, 3, 5, 7 and 7.7 nm. From the shape of the curve, it is confirmed that CFAS/Ag shows spin-valve-like response. Even at the low MR region, particularly t_{CFAS} = 1 and 7.7 nm, spin-valve-like shape can be seen with its unique uniaxial response. At the t_{CFAS} where MR ratio is large, CFAS/Ag show antiparallel state which can be seen gradually lost as the exchange bias from IrMn layer decreases. At

t_{CFAS} = 7.7 nm, the exchange bias is weak, and the spin valve cannot maintain its antiparallel state, therefore GMR cannot be obtained.

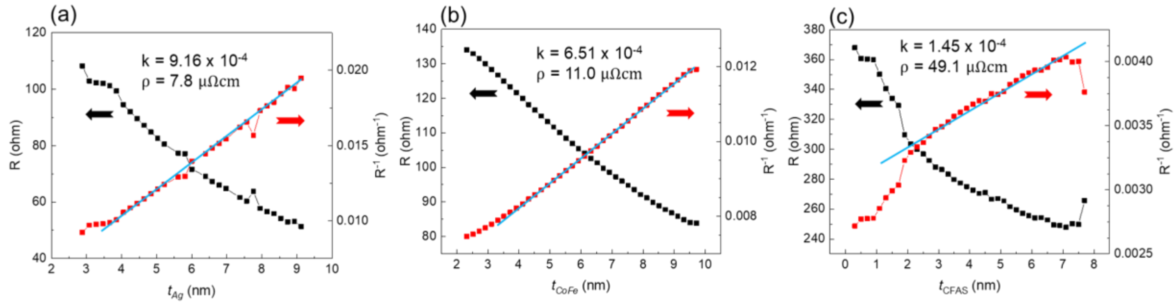

Figure 3.5 Ferromagnetic layer thickness (t_{Ag}, t_{CoFe} and t_{CFAS}) dependence of resistance and its reciprocal for SV with the structures as follows: (a) CoFe(10 nm)/Ag(t_{Ag})/CoFe(5 nm)/IrMn(10 nm)/Ta(3 nm) (b) CoFe(9.5 nm)/Ag(2.5 nm)/CoFe(t_{CoFe})/IrMn(6 nm)/Ta(3 nm) and (c) CFAS(6 nm)/Ag(3 nm)/CFAS(t_{CFAS})/CoFe(1 nm)/IrMn(8 nm)/Ta(3 nm).

Ending this part, before further into the discussion, one important parameter needs to be measured which is resistivity. Resistivity is a physical measure of how a material resist electric current which might give some hint for the poor MR ratio of CFAS/Ag compared to CoFe/Ag despite having similar crystal growth quality. The resistance and resistivity of NM and FM layers are measured and then compared. Figure 3.5 shows the layer thickness (t_{Ag}, t_{CoFe}, t_{CFAS}) dependence of resistance and its reciprocal value measured from spin valve devices. Using the assumption that each layer is a separate conduction channel that connect parallelly, linear relation of the reciprocal of the resistance and the thickness (t_{Ag}, t_{CoFe}, t_{CFAS}) can be deduced by the function $1/R(t) = k\,t + c$ with c as a constant. The slope k is defined as $k = w/(\rho \cdot l)$ with w and l is width and length of the device strips (200 and 2800 μm respectively). Then resistivity of a layer (ρ) can be obtained by calculating k value. Finally, the resistivity for Ag, CoFe and CFAS layers are obtained with value of 7.8, 11.0 and 49.1 μΩcm respectively.

3.2. Discussion

Here, the comparison of the electronic properties between CoFe/Ag and CFAS/Ag spin valves will be discussed. The XRD measurement confirms the B2 long-range ordering of CFAS, indicating that this layer has large spin polarization. It has been confirmed from the TEM in Figure 3.2(b) that CoFe/Ag and CFAS/Ag spin valves are close in terms of crystal growth quality. Both spin valves growth epitaxially well with only small amount of misfit dislocations at FM/NM interfaces. It can even be argued that CFAS/Ag is slightly better due to having less dislocations visible, at least within the observation zone. Having almost similar crystal quality, CFAS/Ag with larger spin polarization of CFAS layer should have shown larger MR ratio compared to CoFe/Ag spin valve. However, as shown in Figure 3.3, the MR ratio of CoFe/Ag spin valve is significantly larger than CFAS/Ag. This lower MR ratio exhibited by CFAS/Ag spin valve does not align with the initial expectation that larger spin polarization will results on larger GMR value. To understand why this is the case, the band matching between CFAS and Ag is calculated using first-principles calculation.

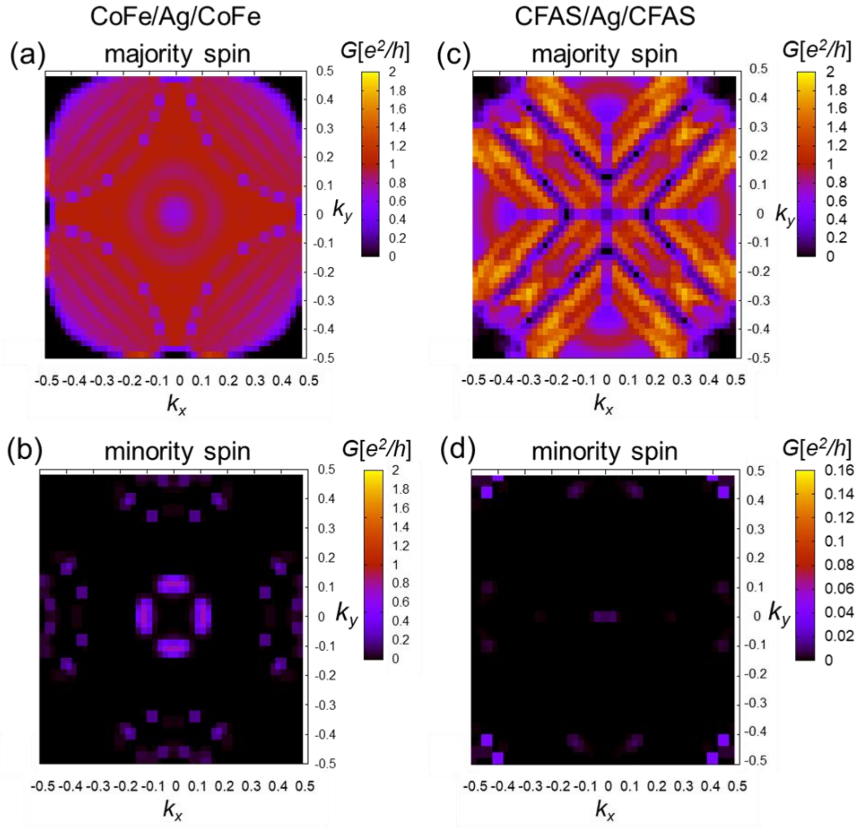

Figure 3.4 Electronic transmission at the Fermi level for the (a) majority- and (b) minority-spin in CoFe/Ag/CoFe and (c) majority- and (d) minority-spin in CFAS/Ag/CFAS layered structure along k_x and k_y. Magnetization configuration of the FM layers in these structures are set in parallel direction.

The spin-dependent electronic transport was calculated using generalized gradient approximation (GGA) within the QUANTUM espresso[104–107]. Superlattice cell was constructed in tetragonal space as CFAS/Ag/CFAS and CoFe/Ag/CoFe multilayers with 9 atomic layers of Ag and 15 atomic layers of CFAS or CoFe. The structure repeats in planar direction. Crystal orientation and lattice constant used in this calculation was taken from the experimental data obtained from both XRD and TEM. The crystal structure of CoFe is set to ideal B2 structure, whereas CFAS is set to ideal $L2_1$. Because the spin polarization between B2 CFAS and $L2_1$ CFAS is not largely different, we consider this approach is still valid. The transmittance was obtained by calculating the solution of the scattering equation from said boundaries; integrating electronic transmission from all k_z and then project it to in-plane wave vector (k_x, k_y) components.

This kind of transport calculation is commonly used to analyze, explain, and even predict the performance of CPP-GMR device by evaluating its spin-dependent transport at the interface[72,108–110]. Although uncommon, this calculation is also works to explain transport in CIP-GMR as well. This calculation show spin-dependent transport properties for electrons transmitting to perpendicular direction of the FM/NM/FM multilayer structure. In CIP-GMR, because magnetoresistance effect arises from the difference in scattering of the electrons passing through both FM layers without changing its spin direction, spin-dependent perpendicular transmittance through this structure is essential. In CPP-GMR, electrons with momentum perpendicular to plane are dominant. Transmittance of the electrons with this momentum $(k_x, k_y)\approx 0$ is more important. In CIP-GMR, it is the opposite. Most electron moves to in-plane direction, having in-plane momentum. In this calculation, transmittance around the zone boundaries, $(k_x, k_y)\approx(\pm 0.5, -0.5$ to $0.5)$ and $(k_x, k_y)\approx(-0.5$ to $0.5, \pm 0.5)$, corresponds to the incident electron almost parallel to the plane just like in CIP-GMR case.

In Figure 3.4(a) and (b), the conduction asymmetry of CoFe/Ag/CoFe structure is not large, especially around the zone boundaries ($\Delta G<1$). However, the contrast exists and can still contributes to GMR ratio, resulting in the MR ratio value of 8.4% which is considered small compared to more commonly used system like $Co_{90}Fe_{10}$/Cu (15% MR ratio) [111]. In the case of CFAS/Ag/CFAS, large conduction asymmetry ($\Delta G>1$) can be seen in Figure 3.4(c) and (d) almost on all regions. It is very apparent that the transmittance asymmetry of CFAS/Ag/CFAS is larger compared to CoFe/Ag/CoFe, including the edge of the zone boundaries. This emphasizes the good band matching between CFAS and Ag. Considering that according to the TEM the crystal structure and lattice matching between CoFe/Ag and CFAS/Ag is comparable, larger conduction asymmetry of CFAS/Ag/CFAS is promising to exhibit larger MR ratio for CFAS/Ag spin valve. This contradiction suggests that there is an additional parameters outside of lattice and band matching which is not yet considered outside of lattice but important in determining the magnetoresistance performance of CIP-GMR.

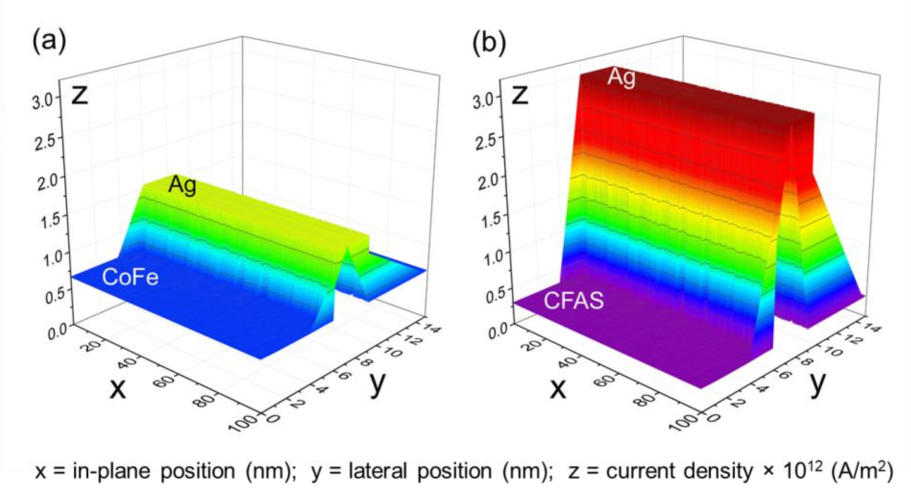

Figure 3.6 The current density distribution of (a) CoFe/Ag/CoFe and (b) CFAS/Ag/CFAS based on CoFe/Ag and CFAS/Ag, respectively. The x and y axes correspond to the coordinate at in-plane and laterally of the film.

To identify the reason why CFAS/Ag spin valve show lower MR ratio, current density distribution of CFAS/Ag/CFAS was simulated and then compared to CoFe/Ag/CoFe. The simulation was conducted using COMSOL Multiphysics software[112]. CFAS/Ag/CFAS and CoFe/Ag/CoFe multilayer with FM layer thickness of 6 nm and Ag of 3 nm are constructed. The size of the planar construct is 80 nm × 200 nm with extreme fine meshing. Gold electrodes are connected to the terminal surface of the construct. The resistivity values that were used for the current density distribution calculation was taken from experimental result in Figure 3.5. Constant current of 1 mA was passed through the structure from and towards the gold electrodes and then the current density was calculated.

The cross section current distribution in the middle of the structure is extracted as shown in Figure 3.6. Figure 3.6 (a) shows the current density distribution of CoFe/Ag/CoFe. The current density between Ag and CoFe is close with the value of 1.2×10^{12} and 6.6×10^{11} A/m^2 for Ag and CoFe layers respectively. These values are not much different, suggesting that currents are flowing inside the Ag spacer and CoFe layer rather equally. This is evident in Figure 3.3(a). Because the resistivity of CoFe allows for conduction in the bulk, electrons coming from the bottom CoFe can still come in deep into top CoFe without previously being scattered. As a result, MR ratio will vary as t_{CoFe} increases. As opposed to rather equal distribution of current in CoFe/Ag/CoFe structure, strong contrast for current density can be observed in CFAS/Ag/CFAS as seen in Figure 3.6(b) with the value of 3.0×10^{12} and 2.9×10^{11} A/m^2 for Ag and CFAS layer, respectively. This large current shunting inside Ag layer suggests that only small amount of electron is conducted through the CFAS layer. Lack of enough current passing through CFAS layer limits the generation of spin-polarized electrons. Small amount of spin-polarized current means that spin-dependent scattering does not work as effectively. As previously suggested by the first-principle calculations in Figure 3.4, interfacial spin-dependent transmission of CFAS/Ag/CFAS is excellent, indicating that this structure can potentially exhibit large MR ratio. However due to the limited amount of spin-polarized current, MR ratio becomes lower.

The effect of different current distribution between CoFe/Ag and CFAS/Ag spin valves is also reflected in how the MR ratio responds. As seen in Figure 3.3(a), both CoFe/Ag show different curvature compared to CFAS/Ag spin valve. In the case of CoFe/Ag, the MR ratio increases as t_{CoFe} increases up to 9.5 nm then start to decrease at larger thickness. This is very common CIP-GMR spin valve behavior[35,80]. The increase of MR ratio as t_{CoFe} increases indicates that the origin of the MR ratio in this system include spin-dependent scattering inside the bulk of CoFe as well. Suppose electron from the bottom CoFe layer will travel passing through Ag spacer then into the other CoFe layer. At low CoFe thickness, electron will arrive at the CoFe/IrMn interface sooner. The electron is either scattered, reflected back or diffuses into IrMn layer. The scattering at CoFe/IrMn interface and the bulk of IrMn is mostly spin-independent which makes sense that in this region MR ratio is low. As t_{CoFe} increases, the travel distance towards CoFe/IrMn interface increases as well. Electron which was supposed to arrive at CoFe/IrMn interface might experience spin-dependent scattering inside the bulk of the CoFe instead, which then contributes to magnetoresistance value. This effect from increasing t_{CoFe} has some limit. At certain point, if the thickness of CoFe is larger than the spin-diffusion length of the electron, number of spin-dependent occurrence does not increase anymore. However, current shunting start to dominates due to the increase of additional conduction channel. At this point, MR ratio degrades.

In CFAS/Ag spin valve case, the curvature of t_{CFAS} dependence of MR ratio is very different. At very low CFAS thickness, CFAS is not properly formed. Ferromagnetic properties of this layer are lost (magnetically dead), therefore GMR cannot be obtained. Resistivity of CFAS is much larger compared to Ag, which from Figure 3.6 it is confirmed that the current in this device mostly passing through the Ag spacer layer. Due to this large current shunting, GMR mostly happen at the CFAS/Ag interface as the mean-free path inside CFAS layer is very limited. Thus, any increase of tCFAS does not increase the number of spin-dependent scattering occurrence nor introduce current shunting through additional CFAS conductive channel. MR ratio then become unchanged even after increasing t_{CFAS}. At certain t_{CFAS}, exchange bias from the IrMn layer weakens and the magnetoresistance effect start to fade. To combat this effect, ferromagnetic material and its nonmagnetic spacer needs to have close value of resistivity just like in CoFe/Ag spin valve. CFAS currently has too large resistivity which negatively impact its MR ratio. In general, the resistivity of Heusler alloys is large, especially with high spin polarization. If one would want to utilize the large spin polarization of Heusler alloy, the resistivity needs to be reduced further. One of the way is improving the chemical ordering of Heusler alloy by increasing its annealing temperature.

3.3. Summary

In summary, spin valve multilayers with CoFe and CFAS as FM layers and Ag as spacer were investigated. Epitaxial growth is confirmed for both CoFe/Ag and CFAS/Ag spin valves with the latter showing almost perfect B2 ordering. First-principles calculation suggest significantly larger conduction asymmetry presents in CFAS/Ag compared to CoFe/Ag. However, the MR ratio of CFAS/Ag is inferior compared to CoFe/Ag with maximum value of 1.2% compared to 8.4% in the case of CoFe/Ag. The main reason of the poor MR ratio found in CFAS/Ag spin valve is due to large resistivity gap between CFAS and Ag layer. Because current flows mainly in the Ag spacer, only small amount of spin-polarized current can be generated from the CFAS. Additionally, the lack of current conduction inside CFAS also reduce the possibility of spin-dependent scattering inside bulk of CFAS. In comparison, CoFe has closer resistivity to Ag which allows for enough spin-polarized to be generated. The generated spin-polarized current then found its way to spin-dependent scattering center both in CoFe/Ag interfaces or bulk of CoFe resulting in larger MR ratio. In summary, high lattice and band matching are both important factors determining GMR ratio but will be rendered useless if the FM layer cannot generate spin-polarized current, in this case because of the large resistivity of CFAS layer. Lowering the resistivity gap between FM and NM layer is necessary to be considered in designing future CIP-GMR device.

Chapter 4: Epitaxial Current-in-plane giant magnetoresistance in $Co_{1-x}Fe_x/Cu/Co_{1-x}Fe_x$ multilayers

In the previous section, spin valve using CFAS as FM layer and Ag as NM spacer layer fails to deliver large MR ratio in CIP-GMR structure even though having high lattice and band matching and has been successfully obtained large MR ratio in CPP-GMR[96,100]. The reason is current shunting through Ag spacer driven by large resistivity gap between CFAS and Ag. In comparison, $Co_{50}Fe_{50}$/Ag show performs better due to having closer resistivity. The approach of using larger spin-polarization FM materials such as Heusler alloys should also consider its resistivity.

Going back to square one, different approach is considered. Historically, Co-Fe alloys has been extensively used as FM materials in combination with Cu spacer[35,81–87]. It is also a fact that most CoFe used in CIP-GMR which shows large MR ratio are having fcc phase. The reason for the use of fcc CoFe is its high lattice matching to Cu spacer. Although various composition is used, fcc CoFe only occupy small region in Co-Fe phase spectrum (Fe content < 30%), with the other stable phase is bcc CoFe (Fe content > 30%)[91]. The use of bcc CoFe in CIP-GMR is not well explored, thus systematic study on the Co-Fe composition dependence of MR ratio is necessary. In this chapter, the study of various composition of Co-Fe alloys in CoFe/Cu/CoFe CIP-GMR spin valves is described. Epitaxial sample is used to minimize external factors such as grain boundaries and other lattice imperfections. It is also worth mentioning that study on CIP-GMR epitaxial device is currently not common.

4.1. Experiment

Spin valve devices with the stacking of $Co_{1-x}Fe_x$(6 nm)/Cu(*t* nm)/$Co_{1-x}Fe_x$(6 nm)/IrMn(8 nm) were deposited on MgO (001) substrate at room temperature (RT). Different composition of $Co_{1-x}Fe_x$ films were used from ($x = 0.10, 0.25, 0.50, 0.67$ and 1.00). The Cu thickness were varied from 0 to 5 nm by depositing this layer into wedged shape using linearly moving shutter. Two additional samples based on interlayer exchange coupling were made with the intention to maximize MR ratio. Their structures are $Co_{50}Fe_{50}$(3 nm)/Cu(1.6 nm)/$Co_{50}Fe_{50}$(3 nm)/MgO(2 nm) and [$Co_{50}Fe_{50}$(3 nm)/Cu(1.6 nm)/$]_{33}$$Co_{50}Fe_{50}$(3 nm)/MgO(2 nm). All samples undergo annealing at 250°C with 3 kOe constant magnetic field. Microfabrication using photolithography and ion etching technique were performed to cut the films into thin strips. Measurement of MR ratio was performed by four-point prober at room temperature with constant current of 1 mA. For structure characterization, XRD and TEM were used. To aid with the analysis, the first-principles calculation on the spin-dependent electron transport were performed using QUANTUM Espresso code. Trilayer structures were constructed for this analysis; B2-$Co_{50}Fe_{50}$ (or Fe)/bcc-Cu/B2-$Co_{50}Fe_{50}$ (or Fe)(001) and fcc-$Co_{90}Fe_{10}$/fcc-Cu/fcc-$Co_{90}Fe_{10}$(110) with 9 atomic layers of Cu spacer and 15 atomic layers of ferromagnets.

4.2. Results and Discussion

Figure 4.1 shows the XRD patterns of the multilayer films. The films with the ferromagnetic layer of $Co_{75}Fe_{25}$, $Co_{50}Fe_{50}$, $Co_{33}Fe_{67}$ and Fe exhibits peak around 66° which is 002 bcc peak indicating the formation of (001)-oriented bcc phase for the FM layer. Peak positions are relatively the same suggesting that their lattice parameters are relatively unchanged. $Co_{90}Fe_{10}$ does not show this peak, which is expected considering it usually forms stable fcc phase for this composition. No other peak indicates the growth texture of $Co_{90}Fe_{10}$ layers. All films show 002 peak of IrMn at 48° including $Co_{90}Fe_{10}$, indicating (001)-oriented growth of IrMn which is not favorable orientation for AFM layer due to weaker exchange bias field caused by its spin structure[113].

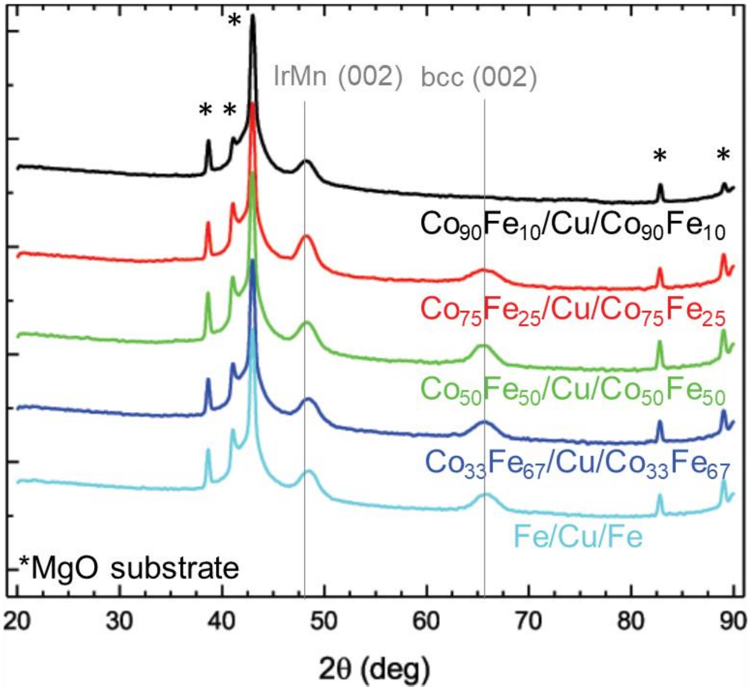

Figure 4.1 Out of plane XRD graph for $Co_{1-x}Fe_x$(6 nm)/Cu(t nm)/$Co_{1-x}Fe_x$(6 nm)/IrMn(8 nm) with (x = 0.10, 0.25, 0.50, 0.67, and 1.00).

Figure 4.2(a) and (b) shows the MR ratio as a function of Cu thickness (t_{Cu}) and composition (x) respectively. All compositions show typical behavior of CIP-GMR spin valve with increasing MR ratio as t_{Cu} decreases, as seen in Figure 1.5. At certain critical thickness, the MR ratio drops to almost zero. This can be understood as when the Cu spacer thickness is low enough, interlayer exchange coupling between FM layers starts to dominate. At such low thickness, both FM layers are ferromagnetically coupled, therefore GMR cannot be achieved[80]. As for the MR ratio value, all devices with Co-Fe alloys which have bcc structure show larger MR ratio compared to fcc $Co_{90}Fe_{10}$ and bcc Fe. The spin valve devices with bcc ferromagnetic layers of $Co_{75}Fe_{25}$, $Co_{50}Fe_{50}$ and $Co_{33}Fe_{67}$ exhibit large MR ratio with the maximum value of 23.4, 26.5, and 23.5% respectively. Fe and $Co_{90}Fe_{10}$ show lower maximum MR value of 5.4 and 10.3%. Poor performance of Fe device is similar to the one previously reported[44,114]. The value for $Co_{90}Fe_{10}$ device is also in agreement with previous reports but slightly lower compared to more optimized structure[33,86,87,115–117]. At the start of this chapter, it was mentioned that most CoFe-based CIP-GMR with large MR ratio value was using fcc-CoFe as FM layer instead of bcc. In this experiment, the result shows that bcc CoFe exhibit much larger MR ratio compared to fcc-CoFe which in this case is $Co_{90}Fe_{10}$. Fe which has similar bcc structure and lattice constant as other bcc CoFe have much lower MR ratio compared to the others which is also need explanation. MR ratio of CIP-GMR using $Co_{50}Fe_{50}$ is 26.5% which is currently largest MR ratio ever reported in CIP-GMR spin valve structure. Other interesting information is the different critical thicknesses for $Co_{75}Fe_{25}$, $Co_{50}Fe_{50}$ and $Co_{33}Fe_{67}$ compared to $Co_{90}Fe_{10}$ and Fe. Having lower Cu critical thickness is very beneficial because lower Cu thickness reduce the current shunting inside Cu, thus increasing MR ratio.

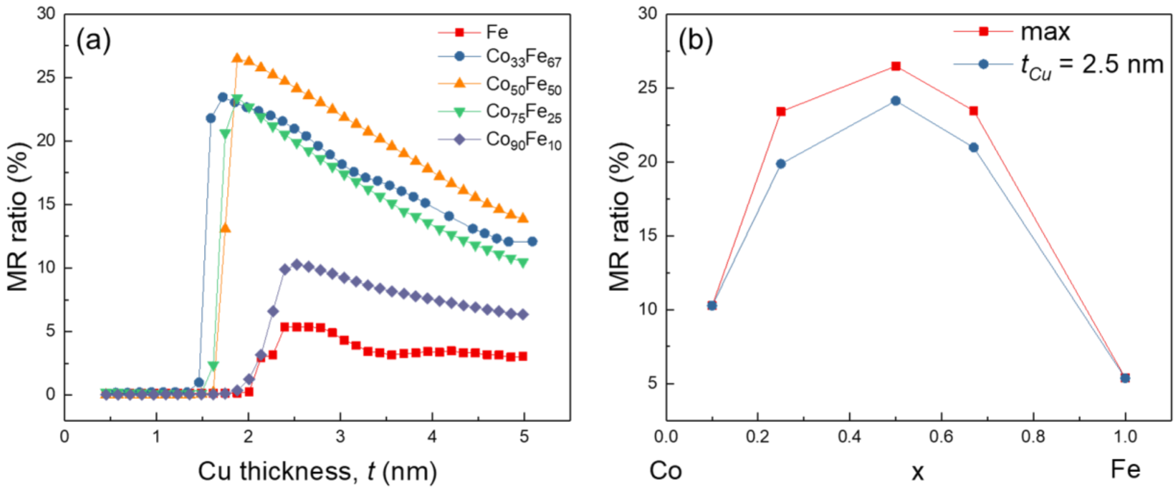

Figure 4.2 (a) Cu thickness dependence of MR ratio of the CIP-GMR spin valves for all $Co_{1-x}Fe_x$ compositions. (b) Composition (x) dependence of the MR ratio showing maximum MR ratio as well as at t_{Cu} = 2.5 nm for all compositions.

To understand the reason for difference in MR ratio, cross-sectional TEM analysis was performed for devices using $Co_{90}Fe_{10}$, $Co_{50}Fe_{50}$ and Fe. Figure 4.3 (a-c) show the high-angle annular dark field scanning transmission electron microscopy (HAADF-STEM) and bright field (BF) TEM images from the cross-section specimen of $Co_{90}Fe_{10}$, $Co_{50}Fe_{50}$ and Fe spin valve devices from [001] azimuth of MgO substrate. Nano beam electron diffractions of the FM and Cu layers are shown in the insets. $Co_{90}Fe_{10}$ device show epitaxial growth with visible atomic column spanning from bottom to top FM layers as seen in Figure 4.3(a). $Co_{90}Fe_{10}$ and Cu layer form fcc structure as seen from the NBED pattern with growth orientation of MgO(001)[100]//$Co_{90}Fe_{10}$(110)[111]//Cu(110)[111]. Lattice mismatching between $Co_{90}Fe_{10}$ to MgO and Cu are 3.1 and 1.8%. Interfaces between $Co_{90}Fe_{10}$ and Cu are difficult to determine due to lack of contrast between Co and Cu, thus interfacial roughness cannot be estimated. Strain marks can be noticed inside the Cu spacer, might be due to lattice mismatching to sandwiching $Co_{90}Fe_{10}$ structures. BF image shows misfit dislocations at $Co_{90}Fe_{10}$/MgO, $Co_{90}Fe_{10}$/Cu and $Co_{90}Fe_{10}$/IrMn interfaces. BF image also confirms the strain marks that can be noticed in the HAADF-STEM image. Overall, the structure is well grown and fit to show 10.3% of MR ratio which is common value for Co$_{90}$Fe$_{10}$/Cu-based CIP-GMR but slightly lower than more optimized structure[33,86,87,115–117]. In most cases, polycrystalline device was used in this system with larger MR ratio when it is (111)-oriented[118]. Because in this study, Co$_{90}$Fe$_{10}$ grows to (110) instead of (111), the MR performance might be compromised. Study on the comparison between (110)- and (111)-oriented growth is required for further understanding about this effect.

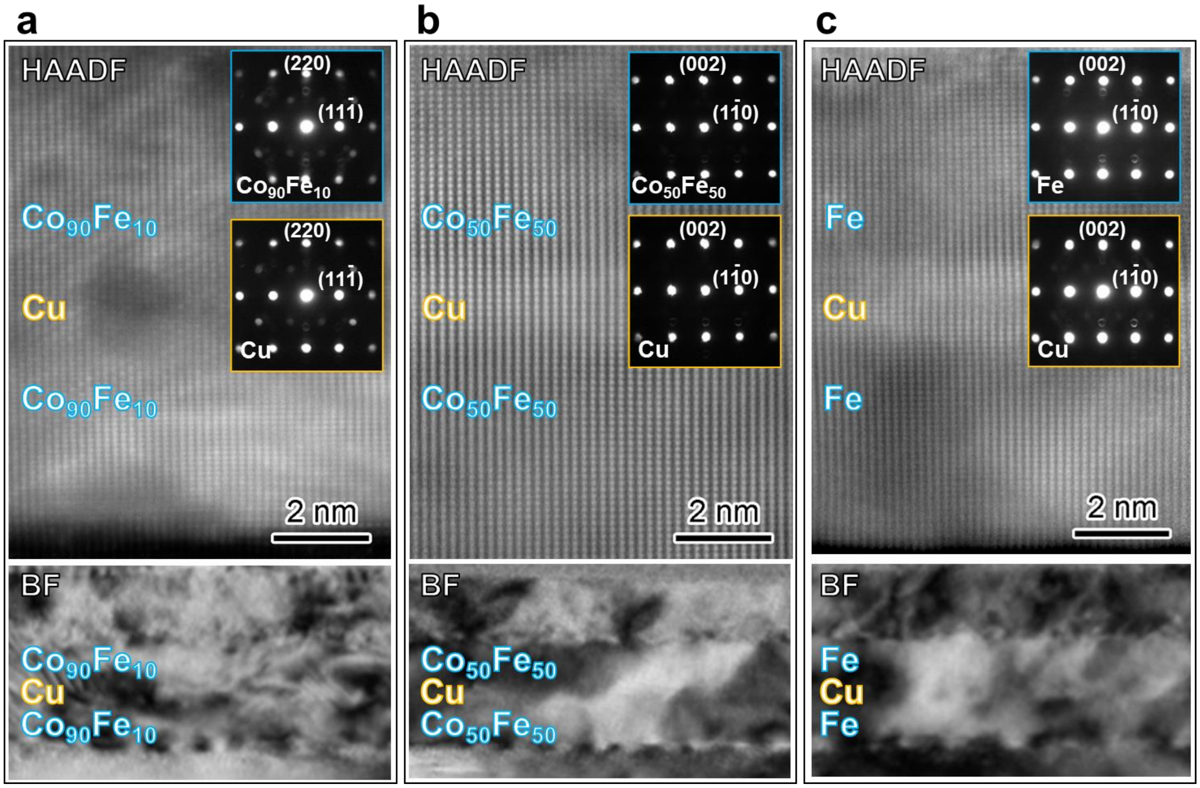

Figure 4.3 HAADF-STEM and BF-TEM images of (a) Co$_{90}$Fe$_{10}$, (b) Co$_{50}$Fe$_{50}$ and (c) Fe spin valve devices. The nanobeam electron diffraction pattern for respective layers are shown in the insets.

The HAADF-STEM image of Co$_{50}$Fe$_{50}$ (Fe) device also shows epitaxial growth with columnar structure across Co$_{50}$Fe$_{50}$ (Fe)/Cu/Co$_{50}$Fe$_{50}$ (Fe) structures coherently. NBED pattern indicate bcc structure of Co$_{50}$Fe$_{50}$ (Fe) layers. Co$_{50}$Fe$_{50}$ (Fe) grow on MgO substrate with the orientation of MgO(001)[100]//Co$_{50}$Fe$_{50}$ (Fe)(001)[110] and 5.0% (4.1%) lattice mismatch. Interestingly, the NBED pattern of Cu mimic the pattern of Co$_{50}$Fe$_{50}$ (Fe) which cannot be understood if Cu forms fcc structure. The only possibility is that Cu forms bcc structure similar to Co$_{50}$Fe$_{50}$ (Fe) layers that surrounds it due to strain. Similar phenomena have been reported by Heinrich *et al.* where Cu forms metastable bcc structure in an epitaxial multilayer of Fe/Cu/Fe grown on GaAs(001) substrate[119]. In this study, the lattice constant of bcc Cu is the same as the lattice constant of Co$_{50}$Fe$_{50}$ (Fe). Because Cu cannot stably form bcc structure without strained environment, comparison to stable lattice constant of bcc-Cu cannot be made. This metastable bcc-

Cu connect top and bottom layer of $Co_{50}Fe_{50}$ (Fe) seamlessly with almost no interfacial imperfection. This is supported by the BF image in which misfit dislocation can be found at $Co_{50}Fe_{50}$ (Fe)/MgO and $Co_{50}Fe_{50}$ (Fe)/IrMn interfaces due to lattice mismatching, but not $Co_{50}Fe_{50}$/Cu. Arguably small amount of misfit dislocation can be observed at Fe/Cu interfaces, but not as much as other interfaces.

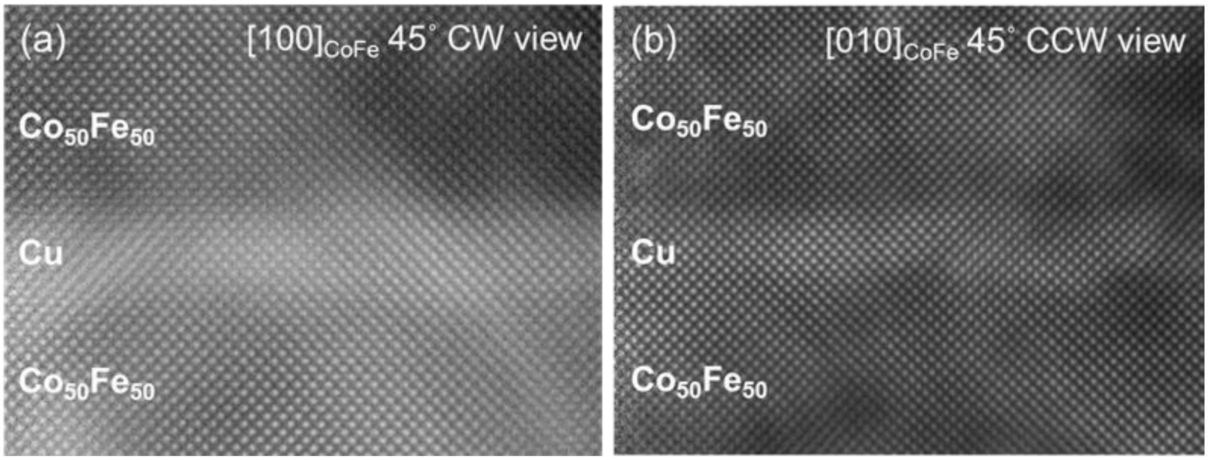

Figure 4.4 HAADF-STEM images of $Co_{50}Fe_{50}$ spin valve devices taken from (a) [100] and (b) [010] of $Co_{50}Fe_{50}$.

For more evidence that Cu grow on bcc structure, HAADF-STEM image of $Co_{50}Fe_{50}$ spin valve were taken from different viewing direction. Two different <100> zone axes of $Co_{50}Fe_{50}$ are chosen, [100] and [010]. The observation angle was planarly rotated clockwise (CW) or counterclockwise (CCW) along the film compared to previous TEM observation. In Figure 4.4(a) and (b), atomic column of Cu aligns perfectly with that of $Co_{50}Fe_{50}$ which is evidence that Cu and $Co_{50}Fe_{50}$ has similar structure with the same lattice parameter. Also, due to other composition with bcc structure i.e., $Co_{75}Fe_{25}$, $Co_{33}Fe_{67}$ and Fe, have their lattice constants close to $Co_{50}Fe_{50}$, it is concluded that similar bcc Cu also grow on those devices. The seamless interface between bcc-$Co_{50}Fe_{50}$ and bcc-Cu might be one of the reasons for large MR ratio in $Co_{50}Fe_{50}$ CIP-GMR device. However, it still cannot explain why Fe device exhibit much lower MR ratio despite having basically very similar structure to that of $Co_{50}Fe_{50}$. Small misfit dislocation found at Fe/Cu interfaces is not detrimental enough to explain the reduction of MR ratio compared to $Co_{50}Fe_{50}$.

To answer this question and to understand the behavior of MR ratio, we look at the band matching between $Co_{50}Fe_{50}$ and Fe and Cu layers using first-principles calculation. Figure 4.5 shows the calculated band structure of the bcc-$Co_{50}Fe_{50}$, bcc-Fe and bcc-Cu near Fermi level. The bcc-Cu shows dispersive *sp* band at the Fermi level with more localized *d* band fully occupied underneath, making this bcc-Cu highly conductive. The majority-spin of $Co_{50}Fe_{50}$ have very similar band profile to that of bcc-Cu with said *sp* band at the Fermi level and *d* band below. This allows great conduction between majority-spin channel of $Co_{50}Fe_{50}$ and bcc-Cu. Interestingly, the aligned band at the Fermi level occurs at *M*-*X* line which is the edge of the Brillouin zone. The implication of this fact will be discussed later. On the other hand, the Fermi level of minority-spin of $Co_{50}Fe_{50}$ is located at more localized *d* band. The more robust *d* band has larger effective mass, thus has lower mobility and conductivity. This do not match with bcc-Cu. This large difference in band structure profile between majority- and minority-spin of Co$_{50}$Fe$_{50}$ resulting in large spin-dependent scattering asymmetry at the Co$_{50}$Fe$_{50}$/Cu interfaces. This is potentially the reason for large MR ratio in Co$_{50}$Fe$_{50}$ CIP-GMR SV. In the case of Fe, both majority- and minority-spin band structure does not match with bcc-Cu. Even though the majority-spin band of Fe is similar to that of Co$_{50}$Fe$_{50}$, the Fermi level is located at slightly lower energy due to smaller number of valence electron compared to Co$_{50}$Fe$_{50}$. This cause unoccupied d band to exist around the Fermi level for the majority-spin of Fe. As a result, the Fe majority-spin band become not match to that of bcc-Cu and spin-dependent scattering asymmetry become lower. This explains why the MR ratio of Fe SV is inferior compared to Co$_{50}$Fe$_{50}$ SV despite having similar microstructure.

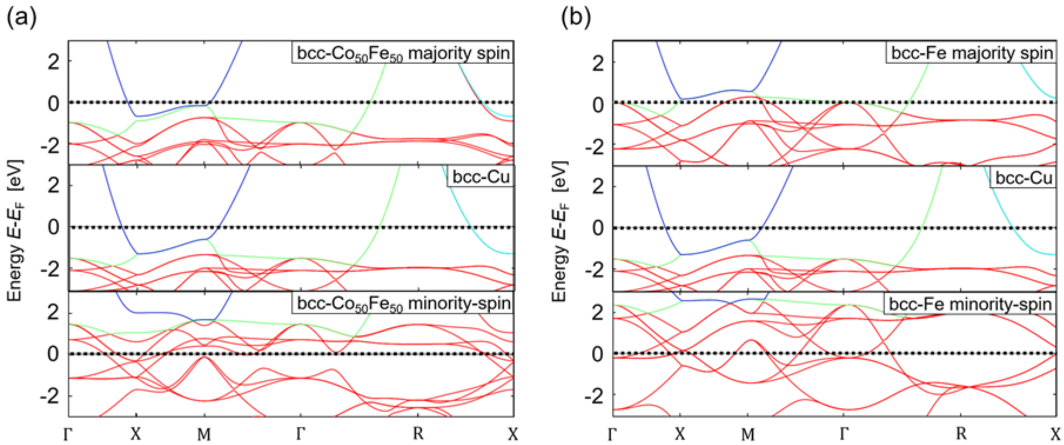

Figure 4.5 Calculated band structures for majority- and minority-spin of (a) bcc-Co$_{50}$Fe$_{50}$ and (b) bcc-Fe as well as bcc-Cu near the Fermi level.

To further understand the transport properties, spin-dependent electronic transmission was calculated in similar fashion to previous section. The structures consist of FM/NM/FM layers. FMs are 15 atomic layers of fcc-Co$_{90}$Fe$_{10}$, B2-Co$_{50}$Fe$_{50}$ and Fe with orientations taken from the TEM observation and lattice parameters taken from XRD. NM is 9 atomic layers of Cu with the structure matched for each FM, fcc for Co$_{90}$Fe$_{10}$ and bcc for Co$_{50}$Fe$_{50}$ and Fe. Figure 4.6(a-f) shows the in-plane wave-vector dependence of the transmittance for majority (a-c) and minority (d-f) spin electrons. Please note that in this calculation, the transmission around the zone boundaries, $(k_x, k_y)\approx(\pm0.5, -0.5$ to $0.5)$ and $(k_x, k_y)\approx(-0.5$ to $0.5, \pm0.5)$, are extremely important in the case of CIP-GMR transport because electron with this momentum is the one having momentum almost in-plane to the structure. In Figure 4.6(a), the majority-spin transmittance of Co$_{90}$Fe$_{10}$/fcc-Cu/Co$_{90}$Fe$_{10}$ show large transmittance especially at the edge of Brillouin zone. In comparison, its minority-spin transmittance is much smaller as shown in Figure 4.6(d), creating large spin asymmetry ($\Delta G>1$) for conduction electron parallel to the plane, resulting in larger MR ratio of this device. If the similar calculation is performed for (111)-oriented fcc-Co$_{90}$Fe$_{10}$/fcc-Cu, it is possible that larger asymmetry would be presents which will explain larger MR ratio in polycrystalline (111)-oriented fcc-Co$_{90}$Fe$_{10}$ devices[33,86,87,115–117].

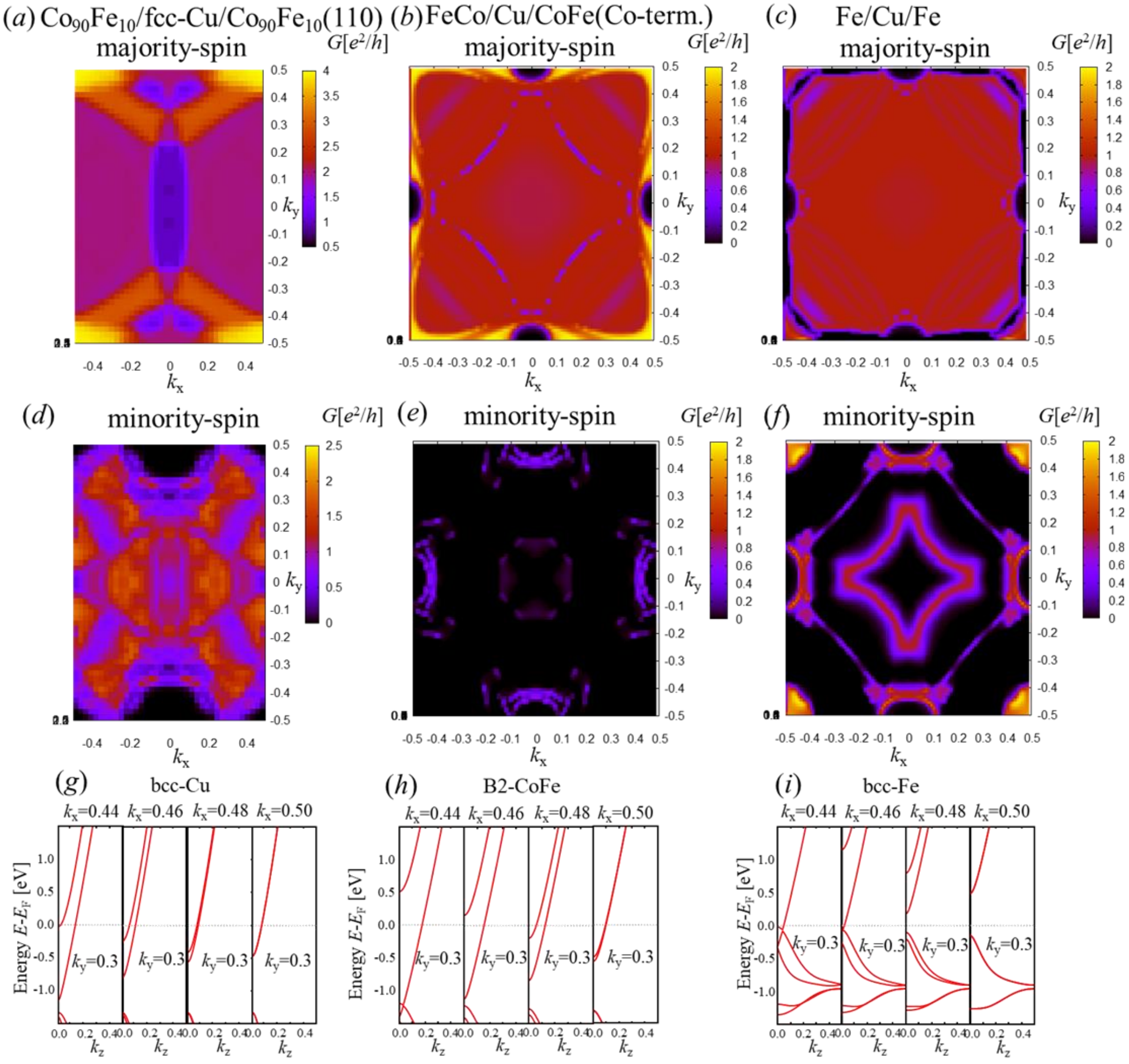

Figure 4.6 Spin-resolved in-plane wave-vector dependence of electronic transmittance for (a,d) $Co_{90}Fe_{10}$/fcc-Cu/$Co_{90}Fe_{10}$, (b,e) $Co_{50}Fe_{50}$/Cu/$Co_{50}Fe_{50}$ and (c,f) Fe/Cu/Fe. The majority-spin band structure of (g) bcc-Cu, (h) B2-$Co_{50}Fe_{50}$ and (i) bcc-Fe at $k_z = 0 - 0.5[2\pi/a]$, $k_y = 0.3[2\pi/a]$ and $k_x = 0.44$, 0.46, 0.48, 0.50$[2\pi/a]$.

In the case of majority-spin transmission of and $Co_{50}Fe_{50}$/bcc-Cu/$Co_{50}Fe_{50}$ in Figure 4.6(b), large transmission can be seen around the edges of the Brillouin zone. Compared to its minority spin around the same area the transmission is much lower. Therefore, the spin-dependent transmittance asymmetry of this structure is very large around the edge of the Brillouin zone. In CIP-GMR, most electrons move at glancing angle because current flows in-plane direction. There will be more population of electrons having momentum with large in-plane components $(k_x, k_y) \approx (-0.5$ to $0.5, \pm 0.5)$ compared to electrons having perpendicular conduction. In the case of $Co_{50}Fe_{50}$/bcc-Cu/$Co_{50}Fe_{50}$, large asymmetry is generated by electrons having momentum almost in-plane which is the electrons most of the case in CIP-GMR, meaning that most electron in this structure will experience large spin-dependence scattering. Thus, the MR ratio in this structure is large in the case of CIP-GMR.

The opposite it true as well. If the edge of the transmission map in Figure 4.6(b) and (e) corresponds electrons move at glancing angle, the center of the transmission map corresponds to electrons having less in-plane component (moves perpendicularly). This is similar to in the case of CPP-GMR, because in CPP-GMR electron move perpendicularly, travel through all of the layers. Because the transmission map shows large asymmetry only at the edge of the map but not the center, it means that the performance of the $Co_{50}Fe_{50}$/bcc-Cu/$Co_{50}Fe_{50}$ in CIP-GMR configuration might be larger compared to its CPP-GMR counterpart. Figure 4.7 shows the magnetoresistance curve for both CIP- and CPP-GMR of the $Co_{50}Fe_{50}$/bcc-Cu/$Co_{50}Fe_{50}$ stacking with similar nominal thickness of all layers. This sample shows large MR ratio of 26% in the case of CIP-GMR but only mere 5% for the CPP-GMR. This is somewhat uncommon to see. It is widely accepted that the performance of CPP-GMR is generally better compared to CIP-GMR with the same stacking. However, this demonstration shows otherwise. It is possible to make CIP-GMR ratio larger than the CPP-GMR as long as the material selected has large spin dependent scattering for electrons moving at glancing angle. Also, it is possible to explain and predict the behavior of certain combination of materials in either CIP- or CPP-GMR using this calculation.

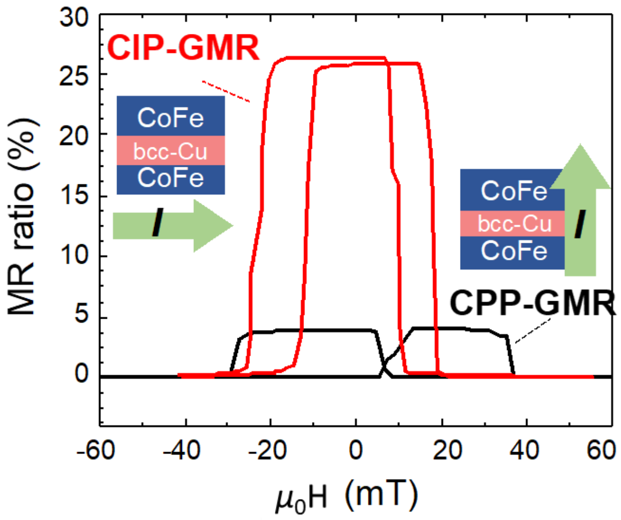

Figure 4.7 The magnetoresistance curves for CIP-GMR and CPP-GMR with the structure of $Co_{50}Fe_{50}$/bcc-Cu/$Co_{50}Fe_{50}$.

For Fe/bcc-Cu/Fe, the majority-spin electron transmission is low, and show sudden decrease near the edge of the Brillouin zone. As mentioned earlier, the edge of the Brillouin zone represents electron with momentum at a glancing angle which is the most populated in CIP-GMR system due to its in-plane nature. The decrease of transmission near the edge of the Brillouin zone decreases the asymmetry between majority- and minority-spin of Fe/Cu/Fe, considering the minority-spin also have low transmission. Thus, the spin-dependent transmittance asymmetry in Fe/Cu/Fe is much smaller compared to the other two devices. Figure 4.6(g)-(i) show k_z dependence of the band structure of bulk bcc-Cu, B2-$Co_{50}Fe_{50}$ and bcc-Fe at the edge of the Brillouin zone. The bcc-Cu show two conduction channel from the *sp* band which cross the Fermi level and at larger k_x start to coincide. The band structure of $Co_{50}Fe_{50}$ has similar profile compared to that of bcc-Cu, having similar conduction channel at the Fermi level. Similar band can be found in bcc-Cu but the Fermi level is located at the bottom of the said *sp* band. As k_x increases, the *sp* band coincides but no longer crossing the Fermi level which explain the reduction of electronic transmission at the edge of the Brillouin zone. This also explains the poor performance of Fe/Cu/Fe device despite having virtually similar structure to that of $Co_{50}Fe_{50}$.

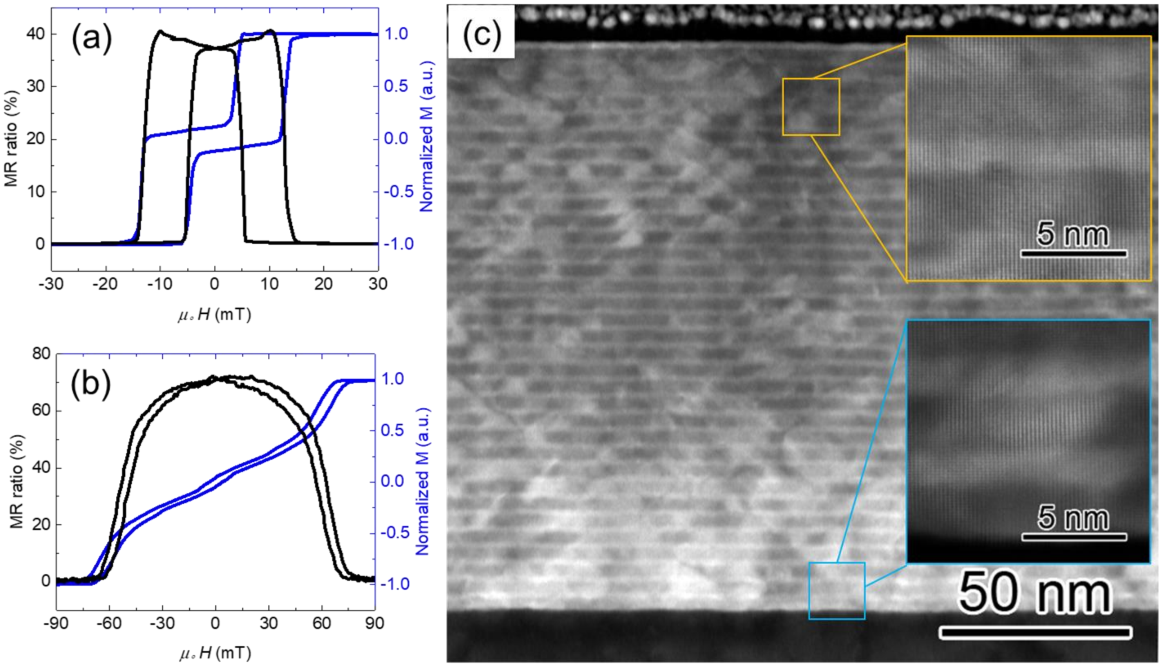

Figure 4.8 Magnetization and magnetoresistance curves of (a) $Co_{50}Fe_{50}$(3 nm)/Cu(1.6 nm)/$Co_{50}Fe_{50}$(3 nm)/MgO(2 nm) and (b) [$Co_{50}Fe_{50}$(3 nm)/Cu(1.6 nm)/]$_{33}$$Co_{50}Fe_{50}$(3 nm)/MgO(2 nm) with antiferromagnetic interlayer exchange coupling via Cu spacer. (c) HAADF-STEM image of the [$Co_{50}Fe_{50}$(3 nm)/Cu(1.6 nm)/]$_{33}$$Co_{50}Fe_{50}$(3 nm)/MgO(2 nm) with insets showing larger magnification of highlighted areas.

In addition to spin valve devices, interlayer exchange coupled devices were also investigated. Specular reflective layer is proven to be effective in increasing MR ratio value[47–49,51,120]. This is because electrons coming to the outer boundary is specularly reflected back into the main FM/NM/FM layers retaining most of the momentum instead of scattered by the FM/AFM or FM/underlayer interfaces. Figure 4.8(a) show the magnetization and magnetoresistance curve of $Co_{50}Fe_{50}$(3 nm)/Cu(1.6 nm)/$Co_{50}Fe_{50}$(3 nm)/MgO(2 nm). Antiparallel state is well-defined around zero field thanks to the antiferromagnetic interlayer exchange coupling between two $Co_{50}Fe_{50}$ layers. This structure exhibits large MR ratio of 40.5% at RT. This value is much larger than that of $Co_{50}Fe_{50}$ spin valve device which has maximum of 26.5%. The increase of magnetoresistance is attributed to the specular reflection of electrons at the $Co_{50}Fe_{50}$/MgO upper layer. The MgO layer reflect the conduction electrons with minimal change to its momentum, prolonging its travel without spin flip. This leads to additional spin-dependent scattering which will increase MR ratio. Similar principle can be applied on CIP-GMR magnetic multilayer structure because instead of outer boundaries, now most of the interfaces are that of FM/NM. The magnetization and magnetoresistance curve of magnetic multilayers $[Co_{50}Fe_{50}$(3 nm)/Cu(1.6 nm)/$]_{33}Co_{50}Fe_{50}$(3 nm)/MgO(2 nm) are shown in Figure 4.8(b). At zero field the magnetization is almost zero, indicating that the structure has fully antiparallel configuration. MR ratio of this structure is much larger compared to the spin valve and IEC devices with the value of 73.3% which signify the limitation of specular reflection layer in retaining the momentum of electron. With this kind of large structure, the stability of the structure especially the metastable bcc-Cu is questioned. HAADF-STEM image of the structure in Figure 4.8(c) shows coherent epitaxial growth throughout the structure. High magnification images in the inset show that whether it is at the bottom or the top, the structures remain the same which is important for consistently obtaining large MR ratio.

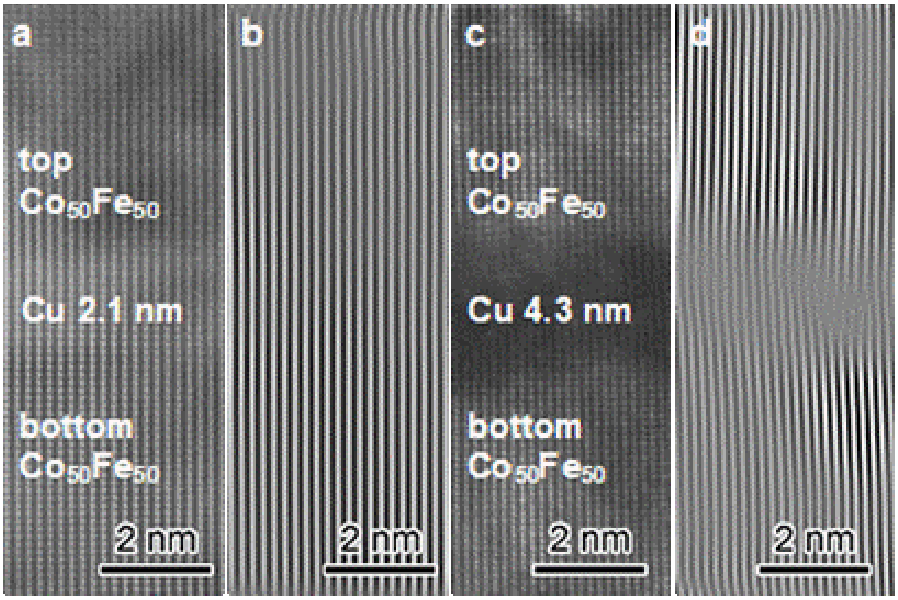

Figure 4.9 HAADF-STEM and IFFT images of $Co_{50}Fe_{50}$ SV with t_{Cu} = (a) & (b) 2.1 nm, (c) & (d) 4.3 nm.

The bcc-CoFe–based CIP-GMR spin valves including $Co_{33}Fe_{67}$, $Co_{50}Fe_{50}$ and $Co_{75}Fe_{25}$ as the FM layers all show large MR ratio. Upon microstructure investigation, the large MR ratio seen in those devices might be caused by the formation of bcc-Cu. Bcc-Cu is not a novel phenomenon. It has been reported previously to be formed in epitaxial Fe/Cu/Fe multilayers or as bcc-Cu precipitates inside Fe matrix[119,121]. In this study, the bcc-Cu formed due to the lattice strain exerted from both bcc-CoFe layers that sandwich the Cu layer. As a result of this strain, the metastable bcc-Cu phase can be stabilized. Because the formation is results of strain, the thicker Cu layer is the more difficult it is to stabilize.

As seen in Figure 4.9, comparing two different thickness of Cu spacer it is very apparent that the more Cu layer there is, the more it is to stabilize bcc phase of the Cu. This is also reflected in Figure 4.2(a) where the MR ratio of $Co_{33}Fe_{67}$, $Co_{50}Fe_{50}$ and $Co_{75}Fe_{25}$ SVs decreases more rapidly compared to $Co_{90}Fe_{10}$ and Fe SVs. This suggests that the reduction of MR ratio as the t_{Cu} increases is not only because of the effect of current shunting but also from the degradation of bcc-Cu.

Currently large improvement of MR ratio in CIP-GMR have been achieved by using $Co_{50}Fe_{50}$ as FM layer and bcc-Cu as spacer due to their high lattice and band matching is potential to be used as magnetic sensor. However, even though the improvement in MR ratio is evident over fcc-CoFe or NiFe-based CIP-GMR devices, the usability as sensor is currently more limited. Two different problems will be discussed further in this thesis. First is large coercivity of $Co_{50}Fe_{50}$ as free layer. As mentioned in section 1.2, coercivity of the magnetic sensor elements need to be small to reduce hysteresis. As it stands, $Co_{50}Fe_{50}$ free layer with the largest shown MR ratio exhibit large coercivity of 39 Oe which is unacceptable for use in linear sensor. Lower coercivity is necessary. This problem will be discussed in Chapter 5. The other problem is that currently the bcc-$Co_{50}Fe_{50}$/bcc-Cu structure is possible by epitaxially grow it on single crystal MgO (001) substrate. This substrate is impractical for commercial use due to can only be produced as small pieces and quite costly compared to for example Si or glass substrates. This problem will be discussed in Chapter 6.

4.4. Summary

In summary, CIP-GMR spin valve devices with Co_xFe_{1-x} were investigated. Devices using bcc $Co_{75}Fe_{25}$, $Co_{50}Fe_{50}$ and $Co_{33}Fe_{67}$ show relatively large MR ratio with the maximum of 26.5% whereas bcc Fe and fcc $Co_{90}Fe_{10}$ devices show lower maximum value of 5.4 and 10.3% respectively. Microstructure analysis was performed to $Co_{90}Fe_{10}$, $Co_{50}Fe_{50}$ and Fe spin valves devices. Although $Co_{90}Fe_{10}$ device show epitaxial growth, misfit dislocations are noticeably appeared due to lattice mismatch between fcc $Co_{90}Fe_{10}$ and fcc Cu (1.8%). On the other hand, epitaxial growth observed in $Co_{50}Fe_{50}$ and Fe devices with near perfect FM/NM interfaces due to the formation of metastable bcc-Cu. The high lattice matching, combined with high band matching between bcc-Cu and bcc-$Co_{50}Fe_{50}$ might be the origin of large MR ratio found in this spin valve. Despite having similar high lattice matching to bcc-Cu, Fe does not have the same level of band matching to bcc-Cu compared to that of bcc-$Co_{50}Fe_{50}$ resulting in poor MR performance. On the other hand, high band matching between fcc-Cu and fcc-$Co_{90}Fe_{10}$ is hindered by lattice defect that appear at the FM/NM interfaces of this device, reducing its MR ratio. Growth direction of $Co_{90}Fe_{10}$ is also (110) instead of the optimal (111) which is considered inferior in obtaining large MR ratio. In conclusion, both high lattice and band matching is important feature to achieve large magnetoresistance in CIP-GMR. Future development of CIP-GMR devices should consider this properties when selecting the materials.

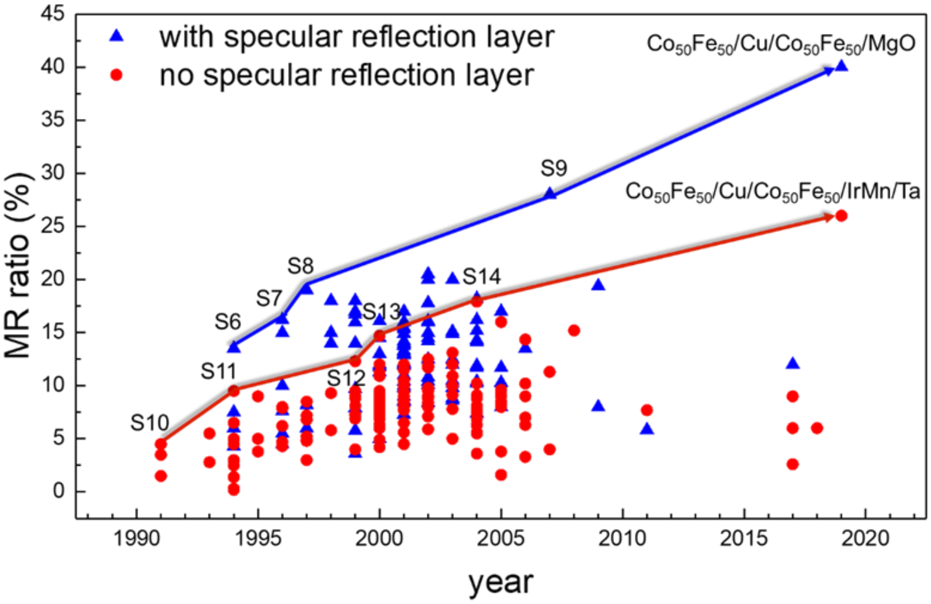

Figure 4.10 MR ratio values of CIP-GMR trilayer spin valves with and without specular reflection layer including recent result obtained in this chapter[33,80,111,115,117,122,123]. This marks new step of improvement in the history of CIP-GMR.

Chapter 5: Reduction of coercivity on epitaxial current-in-plane giant magnetoresistance using CoFeNi alloy

Soft magnetic properties are important in CIP-GMR. When used as free layer, magnetic switching becomes smooth, thus reducing hysteresis. Some materials like permalloy (Ni–rich NiFe) have been used for a long time since early development of CIP-GMR[122] due to the need for switching the magnetization at low external field.

The epitaxial (001) oriented $Co_{50}Fe_{50}$ (CoFe)-based spin valve (SV) device in the previous section show large hysteresis in its free layer which is unacceptable for sensor application. Reducing the coercivity of the $Co_{50}Fe_{50}$ as the free layer becomes necessity. In previous studies of CIP-GMR, it is common to use low-coercivity material as the free layer such as permalloy while keeping high spin polarization materials such as Co-Fe alloy interfacing with the spacer[49,81,86,90]. However, it is not as easy to be applied on $Co_{50}Fe_{50}$ alloy-based spin valve. In the case of $Co_{50}Fe_{50}$ alloy-based spin valve, because currently the structure is top-pinned, the free layer needs to have structure and lattice constant similar to that of $Co_{50}Fe_{50}$ to maintain epitaxial growth. Furthermore, the free layer should not negatively impact the MR ratio of the device while also having low coercivity.

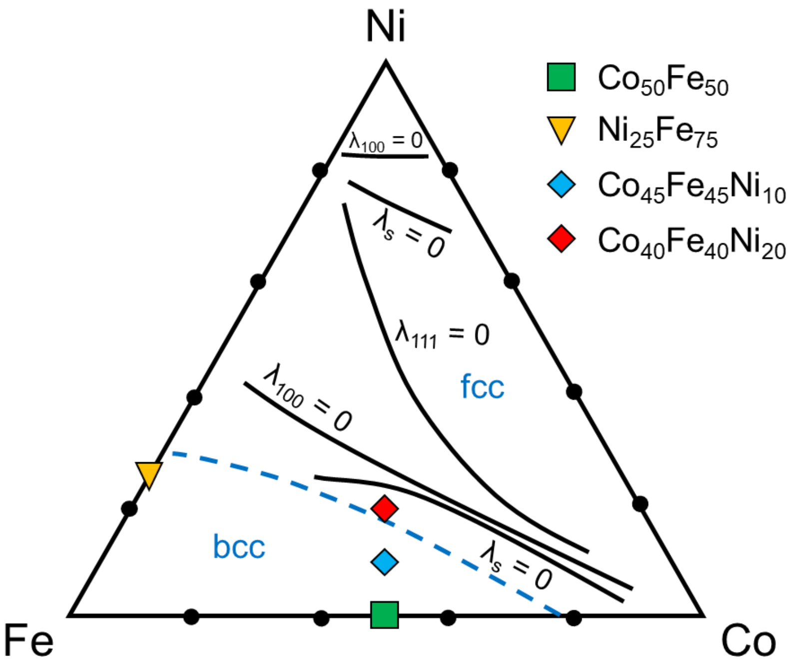

Figure 5.1 Ternary phase diagram of bulk Co–Fe–Ni alloy showing low magnetostriction compositions, adapted from Ishio *et al*[124]. Marked spots are the ferromagnetic materials used in this study, namely $Co_{50}Fe_{50}$, $Ni_{25}Fe_{75}$, $Co_{45}Fe_{45}Ni_{10}$ and $Co_{40}Fe_{40}Ni_{20}$.

To maintain the epitaxial growth of the structure, it is better to select free layer material by modifying $Co_{50}Fe_{50}$ slightly. Because coercivity is indirect result of having nonzero magnetostriction, reducing magnetostriction values for $Co_{50}Fe_{50}$ seems to be a viable option. Figure 5.1 shows the ternary phase diagram of Co–Fe–Ni with lines showing where zero magnetostriction materials can be found in which direction. When $Co_{50}Fe_{50}$ is mixed with Ni around 25%, it could reach the zero magnetostriction line. However, phase stability is concerning. As shown in Figure 5.1, area for zero magnetostriction is located beyond stable bcc phase. By only adding Ni slowly, we might be able to achieve low coercivity but also without sacrificing the bcc structure of $Co_{50}Fe_{50}$. In this section, Ni is introduced into $Co_{50}Fe_{50}$ which will reduce the magnetostriction and magnetocrystalline anisotropy so that the coercivity of the $Co_{50}Fe_{50}$ can be reduced[124]. Because adding Ni reduce the lattice constant of $Co_{50}Fe_{50}$, degradation of the structure is unavoidable, and the reduction of the MR ratio is present.

5.1. Epitaxial bcc-$Ni_{75}Fe_{25}$/Cu–based CIP-GMR spin valve

NiFe has been part of long history of CIP-GMR spin valve since its first introduction[17]. Past published works use Ni-rich NiFe such as permalloy due to its soft magnetic properties and easily textured to (111) direction with proper underlayer such as Ta or NiFeCr[12,50,79,122,125,126] despite showing poor magnetoresistance properties on its own. In most cases, Ni–rich NiFe layer are used in tandem with other fcc ferromagnets such as Co or Co–rich CoFe layer to obtain relatively large GMR ratio with low hysteresis.

In this study, $Ni_{75}Fe_{25}$ (NiFe) was tried as an alternative for CoFe as ferromagnetic material in bcc-Cu–based CIP-GMR spin valve. This material is selected due to certain criteria. First, it has stable bcc phase at room temperature in thin film forms with lattice constant similar to that of CoFe. Having bcc structure is important because otherwise, bcc-Cu cannot be formed. This also allows for combining this alloy into composite layer with CoFe if needed without degrading its microstructure. The other reason is its electronic properties. Because total valence electron of $Ni_{75}Fe_{25}$ is similar as CoFe, it expected that this material will also exhibit large MR ratio. Currently, there have not been any study using NiFe of this composition for CIP-GMR spin valve.

5.1.1. Experiments and Results

Four spin valve type CIP-GMR films were fabricated with either CoFe or NiFe as the pinned or free FM layers. The multilayer stackings are listed in the table below.

Table 5.1. List of all spin valve samples with the structure of
MgO substrate/free layer/Cu(0-5 nm)/pinned layer/IrMn(8 nm)/Ta(2 nm).

sample ID	free layer (*t* nm)	pinned layer (*t* nm)
CoFe-CoFe	$Co_{50}Fe_{50}(6)$	$Co_{50}Fe_{50}(6)$
NiFe/CoFe-CoFe	$Ni_{25}Fe_{75}(5)/Co_{50}Fe_{50}(1)$	$Co_{50}Fe_{50}(6)$
NiFe-CoFe	$Ni_{25}Fe_{75}(6)$	$Co_{50}Fe_{50}(6)$
NiFe-NiFe	$Ni_{25}Fe_{75}(6)$	$Ni_{25}Fe_{75}(6)$

All the multilayer stackings are deposited using sputtering from a single target for each layer at RT under high vacuum condition. The substrate used is (001)–oriented single crystal MgO substrate to induce epitaxial growth. Prior to deposition, MgO substrate was cleaned chemically using deionized water, acetone, then isopropyl alcohol in succession for 10 minutes each. Ar ion cleaning for 5 minute in-situ right before the deposition was performed to remove any surface contamination and make the surface of the substrates slightly smoother.

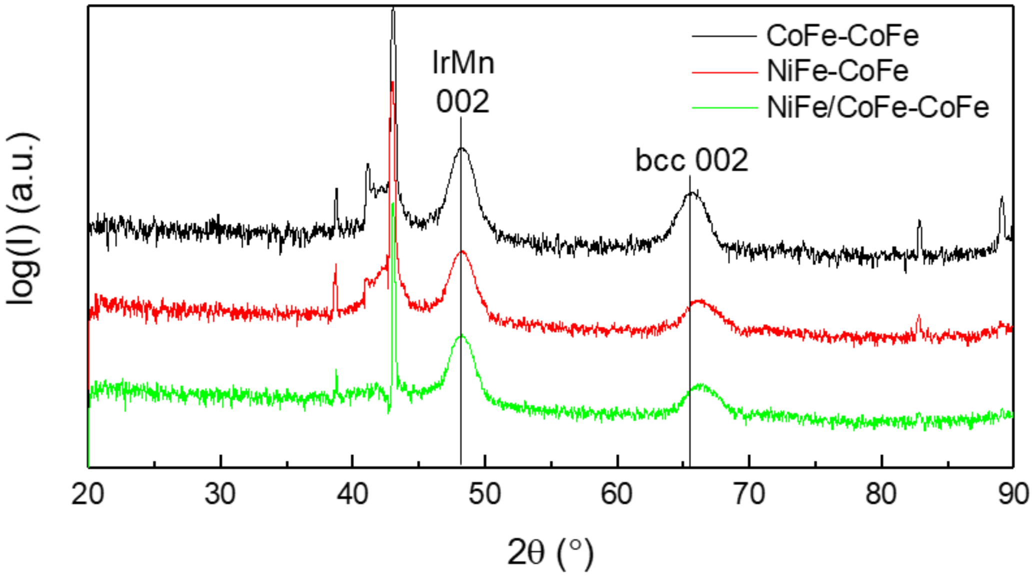

Figure 5.2 The out of plane XRD profile of CoFe-CoFe, NiFe-CoFe and CoFe/CoFe-CoFe SVs.

Crystal structure of the CoFe-CoFe, NiFe-CoFe and CoFe/CoFe-CoFe SVs were evaluated using out-of-plane XRD measurement; the XRD profile is plotted in Figure 5.2. CoFe-CoFe spin valve show CoFe 002 peak at 66° and IrMn 002 peak at 48°, indicating (001)–oriented growth of this multilayer. The other multilayers show similar feature with IrMn 002 and bcc 002 peak. The bcc 002 peak is slightly shifted to larger angle due to slightly smaller lattice constant of NiFe layer. In fact, the bcc 002 peak is the overlap between NiFe and CoFe layer, as they have close lattice constant. Overall, as designed, the bcc structure and the crystal growth orientation are preserved even after changing part of the FM layers into NiFe. Also, because the observation in Chapter 4 confirms the epitaxial growth of CoFe/Cu/CoFe CIP-GMR, this is also be expected from these samples too, including the formation of bcc-Cu.

After the deposition by sputtering, the samples were annealed at 250°C for 1h in low vacuum. The annealing was performed under constant 3 kOe magnetic field to align the magnetization of the FM layers and induce pinning from the IrMn layer. The multilayer films then were fabricated into sets of small strips with the size of 200 μm × 3350 μm using photolithography technique. With the Cu thickness is not flat/wedged, after making the spin valve film into small strip devices, each device effectively will have Cu with almost flat thickness.

Figure 5.3(a) shows the t_{Cu} dependence of MR ratio for CoFe-CoFe, NiFe/CoFe-CoFe, NiFe-CoFe and NiFe-NiFe SVs. All samples show typical spin valve behavior with increasing MR ratio as t_{Cu} decreases. Down to certain critical thickness, the FM layers start to show stronger ferromagnetic interlayer exchange coupling which prevents antiparallel state formation that effectively diminish MR ratio. CoFe-CoFe SV show largest maximum MR ratio among all samples with the maximum value of 24.9%. In the opposite side, NiFe-NiFe show lowest maximum MR ratio of 6.8%. Interestingly, when certain part of NiFe is swapped into CoFe, MR ratio largely increases. Changing the pinned layer completely into CoFe layer increases max MR ratio into 10.7%. Further swapping from 1 nm of NiFe near Cu into CoFe increases maximum MR ratio further into 18.5%.

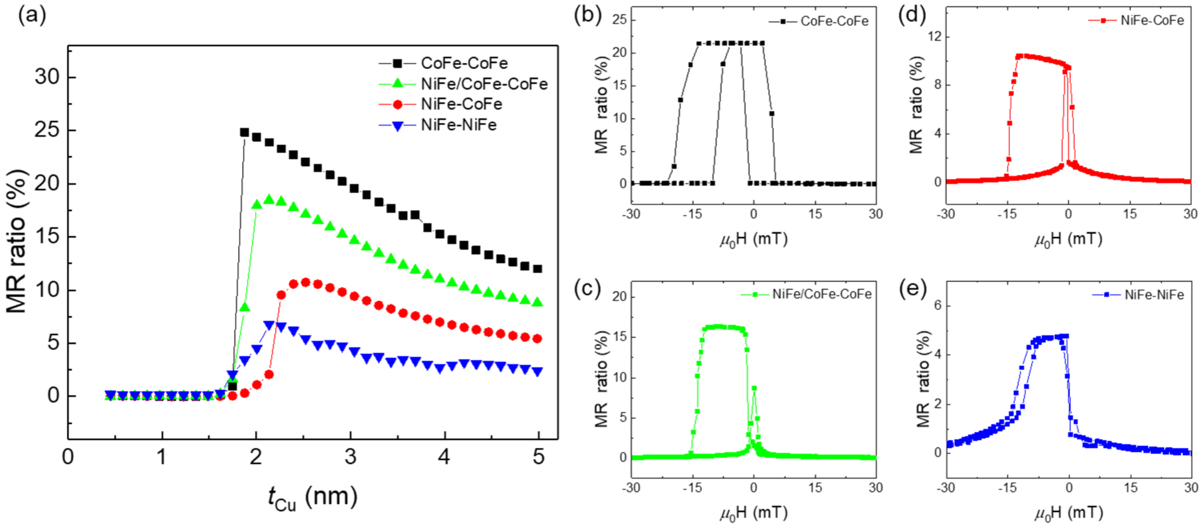

Figure 5.3 (a) The t_{Cu} dependence of MR ratio for CoFe-CoFe, NiFe/CoFe-CoFe, NiFe-CoFe and NiFe-NiFe SVs. The magnetoresistance curves for (b) CoFe-CoFe, (c) NiFe/CoFe-CoFe, (d) NiFe-CoFe and (e) NiFe-NiFe SVs at t_{Cu} = 2.6 nm are included.

The magnetoresistance curves of the CoFe-CoFe, NiFe/CoFe-CoFe, NiFe-CoFe and NiFe-NiFe SVs are depicted in Figure 5.3. At t_{Cu} = 2.6 the MR ratio of CoFe-CoFe SV is as large as 21.5%. Coercivity of the free layer from this sample is quite large with the value of 6.4 mT. Again, on the opposite side is NiFe-NiFe SV with the lowest MR ratio of 4.8% at the same t_{Cu}. However, the coercivity is remarkably small, down to 0.4 mT. As CoFe layer is introduced into NiFe-NiFe, MR ratio and the coercivity increases. NiFe-CoFe SV shows MR ratio of 10.4% with 1.6 mT coercivity whereas NiFe/CoFe-CoFe SV shows MR ratio of 16.3% with 2.4 mT coercivity. NiFe does decrease the coercivity of the bcc-CoFe/Cu–based CIP GMR spin valve but costing the MR ratio of the device.

5.1.2. Discussion

NiFe with bcc structure, which in this case has nominal composition of $Ni_{25}Fe_{75}$, has rarely been used in spintronic devices. In this study, it is particularly important to use such material. From Figure 5.2, it has been established that swapping CoFe layer into NiFe does not degrade the crystallographic orientation of the multilayer spin valve. It is strongly suggesting that even after the introduction of NiFe layer, bcc-Cu is still formed. Now, the more important thing is the MR ratio and the coercivity. The coercivity reduction can be simply understood as the NiFe has much softer ferromagnetic properties compared to CoFe. Therefore, as the NiFe is introduced more into the system, the coercivity got reduced, especially the coercivity of the free layer.

The MR ratio values of the SV devices show interesting behavior which could tell some story about the transport inside the CIP-GMR SVs. CoFe-CoFe SV show large MR ratio as seen in Chapter 4 due to good lattice and band matching between bcc-CoFe and the metastable bcc-Cu. NiFe-NiFe show much lower MR ratio with maximum of 6.8%. Because the lattice matching is similar to the case of CoFe-CoFe, it can be said that this lower MR ratio is due to poor band matching. When the pinned layer changed from NiFe into CoFe layer, it becomes half NiFe and half CoFe spin valve as seen in NiFe-CoFe SV. The maximum MR ratio then increases to 10.7%. Interestingly, when 1 nm of the NiFe layer close to Cu is swapped into CoFe, maximum MR ratio increases dramatically to 18.5% which should not be the case. This phenomena suggests that the performance is not linear to the NiFe:CoFe thickness ratio. CoFe at the FM/Cu interfaces is the most important one which provide large spin-dependent scattering which dramatically increase MR ratio even just with small number of thickness. This is similar with the case introduced by Parkin *et al*[127]. When Co is added at Py/Cu interfaces in Py–based CIP-GMR spin valve, MR ratio dramatically increases from 2.9 to 6.4%. It was argued that the spin dependent scattering at the interface of Co/Cu is much more effective compared to NiFe/Cu. In CIP-GMR, because most electrons move in-plane direction, scatterings at the interface are the one most likely to occur. Therefore, the additional spin-dependent scattering at the interface due to Co insertion can increase MR ratio. Similarly, in this study due to more effective spin-dependent scattering of CoFe/Cu interfaces compared to NiFe/Cu, the addition of CoFe at the interface increase MR ratio largely even though it is just 1 nm thick. This method of making composite FM layer as free layer using low MR ratio material having low coercivity and large MR ratio material at the FM/NM interface might be viable strategy to keep MR ratio high while reducing the coercivity of the free layer.

5.2. Epitaxial bcc-CoFeNi/Cu–based CIP-GMR spin valve

Learning from the result of bcc-NiFe/Cu–based CIP-GMR in the previous section, two things need to be emphasized. First, bcc-NiFe do have lower coercivity compared to bcc-CoFe. However, the use of this material substituting CoFe so far negatively impacts the MR ratio. There is a need to obtain a material which not only reduce coercivity but also not too much reducing the MR ratio. Secondly, although NiFe degrades the MR ratio of CoFe–based CIP-GMR, the use of composite NiFe/CoFe layer as free layer suppress the reduction of the MR ratio.

The material that will be used in this section is Co–Fe–Ni alloy that is directly derived from $Co_{50}Fe_{50}$ with the intention of keeping the properties as close as possible to $Co_{50}Fe_{50}$ while also reducing its coercivity. As seen in Figure 5.1, there is zero magnetostriction zone that is close to $Co_{50}Fe_{50}$ around 25% Ni content. However too much Ni will transform the phase into fcc instead of the necessary bcc structure. Therefore, in this study $Co_{50}Fe_{50}$ is mixed with Ni to form $(Co_{50}Fe_{50})_{100-x}Ni_x$ alloy. Ni content (x) was adjusted to 10 and 20%.

5.2.1. Experimental and Results

Five different CIP-GMR spin valve devices were deposited on single crystalline MgO (001) substrates with the structure of MgO substrate/free layer/Cu(3 nm)/pinned layer/IrMn(8 nm)/Ta(2 nm). Free layer and pinned layer for each samples are listed on Table 5.2.

Table 5.2. List of all spin valve samples with the structure of MgO substrate/free layer/Cu(3 nm)/pinned layer/IrMn(8 nm)/Ta(2 nm).

sample ID	free layer (*t* nm)	pinned layer (*t* nm)
A	$Co_{50}Fe_{50}(6)$	$Co_{50}Fe_{50}(6)$
B1	$Co_{45}Fe_{45}Ni_{10}(5)/Co_{50}Fe_{50}(1)$	$Co_{50}Fe_{50}(6)$
B2	$Co_{45}Fe_{45}Ni_{10}(6)$	$Co_{45}Fe_{45}Ni_{10}(6)$
C1	$Co_{40}Fe_{40}Ni_{20}(5)/Co_{50}Fe_{50}(1)$	$Co_{50}Fe_{50}(6)$
C2	$Co_{40}Fe_{40}Ni_{20}(6)$	$Co_{45}Fe_{45}Ni_{10}(6)$

The spin valve A is the control sample with $Co_{50}Fe_{50}$ as both the pinned and the free ferromagnetic layer. Sample B1 and C1 use $Co_{50}Fe_{50}$ as the pinned FM layer. The free layer is the composite of 1 nm of $Co_{50}Fe_{50}$ interfacing with Cu spacer and the rest of the free layer is 5 nm of $Co_{45}Fe_{45}Ni_{10}$ or $Co_{40}Fe_{40}Ni_{20}$ for B1 and C1 respectively. Spin valve B2 and C2 uses $Co_{45}Fe_{45}Ni_{10}$ and $Co_{40}Fe_{40}Ni_{20}$ respectively for both pinned and free layer.

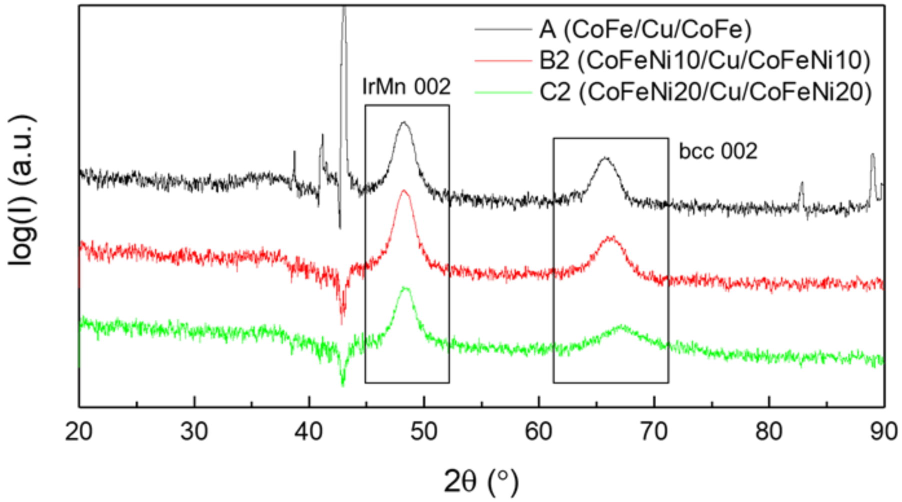

Figure 5.4 Out of plane XRD profile for spin valve A, B2 and C2.

Crystal structure analysis was performed by X-ray diffractometer (XRD). Figure 5.4 shows the XRD plot for spin valve A, B2 and C2. All samples show similar IrMn 002 peak which confirms their (001)-oriented growth. Unfortunately, for this orientation the exchange coupling from IrMn is weaker, which will result in lower exchange bias field. Spin valve A, B2 and C2 show bcc 002 peak at at 65.7°, 66.1° and 67.2° which belong to their FM layers: $Co_{50}Fe_{50}$, $Co_{45}Fe_{45}Ni_{10}$ and $Co_{40}Fe_{40}Ni_{20}$ respectively. The calculated lattice constants for $Co_{50}Fe_{50}$, $Co_{45}Fe_{45}Ni_{10}$ and $Co_{40}Fe_{40}Ni_{20}$ are 2.838, 2.825 and 2.784 Å respectively. It is interesting to note that the bcc peak for spin valve C2 has weaker intensity and much broader compared to other two spin valves.

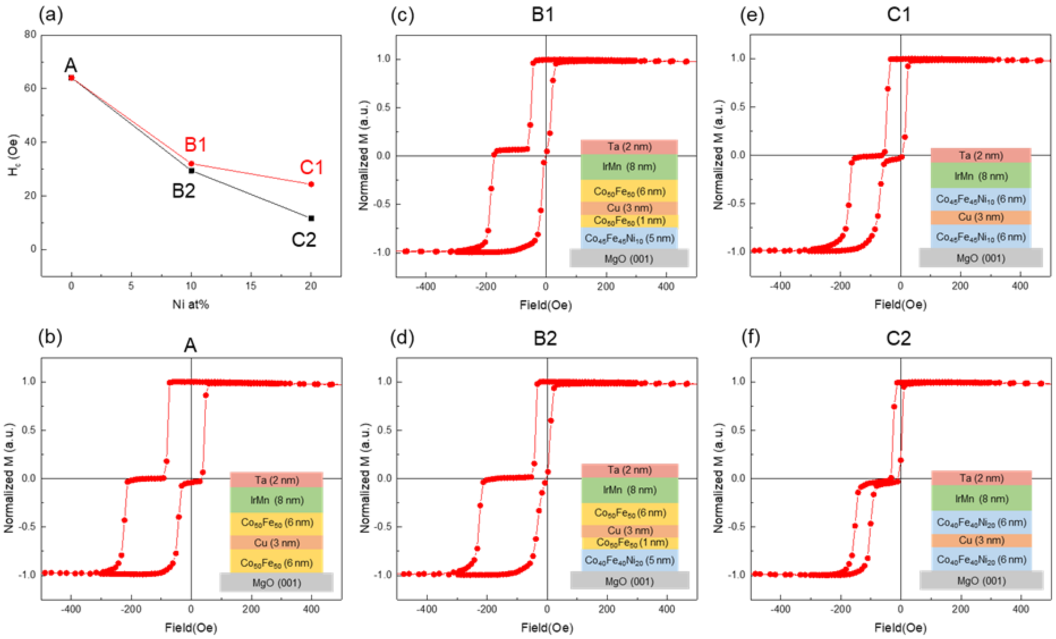

Figure 5.5 The magnetization curves for spin valve (b) A, (c) B1, (d) B2, (e) C1 and (f) C2. The value of their free layer coercivities are summarized in (a).

The measurement of magnetization curve was done using vibrating-sample magnetometer (VSM). Figure 5.5 shows the magnetization curves for all samples. Spin valve A which contains $Co_{50}Fe_{50}$ for its free and pinned layer show large coercivity of 64 Oe. Spin valve B1 and C1 both has its free layer partly changed from $Co_{50}Fe_{50}$ to $Co_{45}Fe_{45}Ni_{10}$ and $Co_{40}Fe_{40}Ni_{20}$ respectively. As a result, coercivity reduces significantly to 32 and 24 Oe for spin valve B1 and C1 respectively. When both free and pinned layer changed to $Co_{45}Fe_{45}Ni_{10}$ and $Co_{40}Fe_{40}Ni_{20}$ as seen in spin valve B2 and C2, further reduction of coercivity is observed down to 29 and 12 Oe respectively.

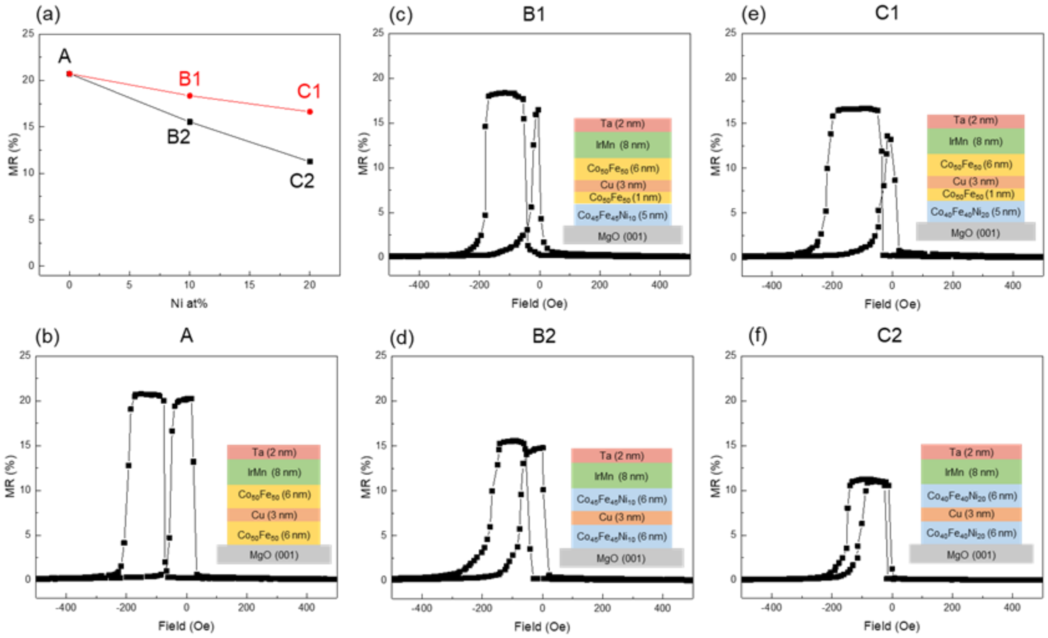

Figure 5.6 The magnetoresistance curves for spin valve (b) A, (c) B1, (d) B2, (e) C1 and (f) C2. The value of their MR ratio are summarized in (a).

After deposition, the multilayer film was annealed at 250°C for 1h under 3 kOe constant magnetic field to introduce exchange bias from the IrMn AFM layer. The multilayer film then microfabricated to make 200 μm × 3350 μm device strips to be measured its magnetotransport properties. Figure 5.3 shows the magnetoresistance curves for all samples. Spin valve A exhibit large MR ratio of 20.7%. With each replacement of $Co_{50}Fe_{50}$ into $Co_{45}Fe_{45}Ni_{10}$ or $Co_{20}Fe_{20}Ni_{20}$, the MR ratio further reduced. For $Co_{45}Fe_{45}Ni_{10}$, free layer replacement, B1, reduces MR ratio to 18.4% whereas total replacement, B2, resulting in MR ratio of 15.5%. For $Co_{45}Fe_{45}Ni_{10}$, MR ratio reduction is much more severe with free layer replacement, C1, reduces MR ratio to 16.6% whereas total replacement, C2, resulting in MR ratio of 11.3%. Exchange bias field for all samples are relatively similar but the values are small, 100-150 Oe, which is expected due to IrMn show (001)-oriented growth. (001)-oriented IrMn have much weaker exchange coupling energy instead of commonly used (111)-orientation due to its spin structure. This exchange bias value is large enough to pin the magnetization of the pinned layer effectively so that antiparallel state can be established. It is interesting to note that due to different in coercivity between B1 and C1, perfect antiparallel state is achieved only for one direction of sweep but not the other. Larger exchange bias field will likely solve this issue. From this result, each addition of Ni into $Co_{50}Fe_{50}$ is successfully reduces coercivity, but also negatively impact MR ratio.

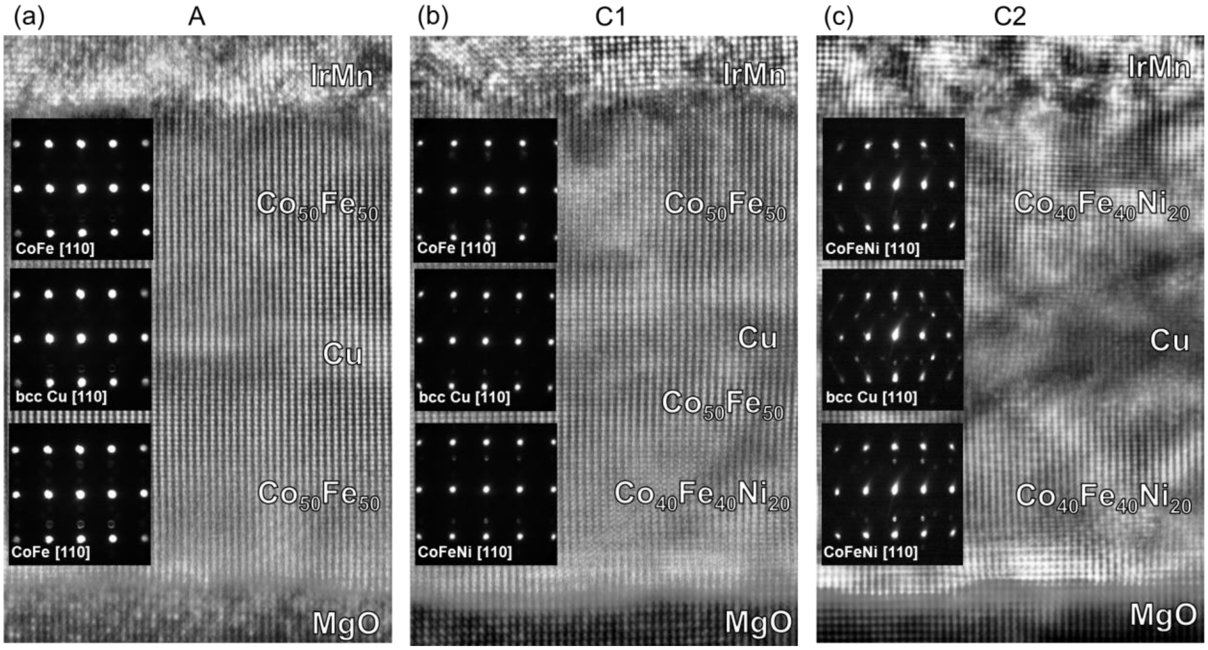

Figure 5.7 HAADF-STEM images of spin valve (a) A, (b) C1 and (c) C2 with nanobeam electron diffraction (NBED) pattern for respective layers are shown in the insets.

To understand the reason behind such reduction on magnetoresistance, STEM analysis was performed along <100> azimuth of MgO. In this case only devices with $Co_{50}Fe_{50}$ and $Co_{40}Fe_{40}Ni_{20}$ are compared. Figure 5.7 shows the HAADF-STEM image for spin valve A, C1 and C2 along with the nanobeam electron diffraction pattern (NBED) for select layers. Spin valve A show epitaxial growth with atomic column across CoFe and Cu layers. Misfit dislocation can be noticed at the $Co_{50}Fe_{50}$/MgO and $Co_{50}Fe_{50}$/IrMn interfaces but does not seem to affect CoFe/Cu interfaces. NBED pattern show bcc phase for $Co_{50}Fe_{50}$ and Cu layer with growth orientation of is MgO(001)[100]//CoFe(001)[110]//bcc-Cu(001)[110] and similar lattice constant. Spin valve C1 has similar stacking with A but with 5 nm of $Co_{40}Fe_{40}Ni_{20}$ replacing $Co_{50}Fe_{50}$. Overall, the structure is similar with spin valve A with epitaxial growth of the structure, stably forming bcc-Cu. As suggested by the XRD, lattice constant of $Co_{50}Fe_{50}$ is reduced when Ni is added; from 2.838 Å in $Co_{50}Fe_{50}$ to 2.784 Å in $Co_{40}Fe_{40}Ni_{20}$. This slight change in lattice constant increase the lattice mismatch to the outer layer, namely MgO substrate from 5% in $Co_{50}Fe_{50}$ to 7% in $Co_{40}Fe_{40}Ni_{20}$. As a result, much more misfit dislocation can be noticed at the $Co_{40}Fe_{40}Ni_{20}$/MgO interface. Furthermore, due to lattice mismatch between $Co_{50}Fe_{50}$ to and $Co_{40}Fe_{40}Ni_{20}$, stacking fault inside $Co_{40}Fe_{40}Ni_{20}$ can be noticed as well. The NBED pattern is closely resemble that of spin valve A suggesting that Cu spacer region does not seem to be heavily affected and still maintain its bcc structure. It is very likely that the reason for the decreased MR ratio in the case of C1 is something else.

5.2.2. Discussion

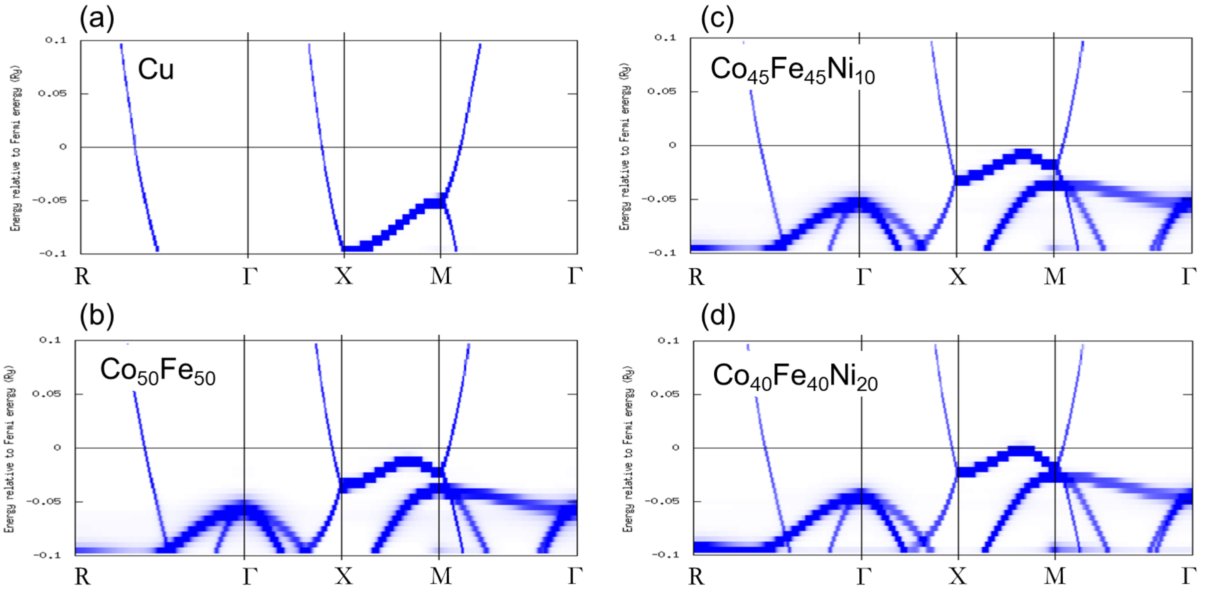

Figure 5.8 Band structure of (a) Cu and majority-spin of (b) $Co_{50}Fe_{50}$, (c) $Co_{45}Fe_{45}Ni_{10}$ and (d) $Co_{40}Fe_{40}Ni_{20}$ along high symmetry points.

In spin valve C2 the structure is much more degraded especially the Cu spacer. Multiple set of reflection can be noticed from the NBED pattern of Cu suggesting there are multiple phases (or orientation) of Cu presents. This might be the main reason for the MR ratio reduction in this case. However, the structure between spin valve A and C1 is very close both visually in the HAADF-STEM image and structurally from the NBED pattern. Thus, the reason for the degradation of MR ratio from spin valve A to C1 might be beyond structural only. For further understanding to the effect of Ni addition to the intrinsic properties, electronic band calculation for Cu as well as majority-spin of $Co_{50}Fe_{50}$, $Co_{45}Fe_{45}Ni_{10}$ and $Co_{40}Fe_{40}Ni_{20}$ was conducted. According to rigid band model[128], each addition of Ni content increase the total valence electron of $Co_{50}Fe_{50}$ thus driving the Fermi level further from the *d* bands. This will increase the band matching towards bcc-Cu and potentially increase MR ratio. However, Figure 5.5 suggest the opposite. Each addition of Ni (0, 10 and 20%) show the decrease of Fermi level closer to the valence *d* bands. In this study each addition of Ni reduces the lattice constant of $Co_{50}Fe_{50}$. With the decrease of lattice constant, interatomic distance reduces as well. Consequently, *s*–*d* interaction become stronger and *d* band moves towards the Fermi level. This is especially apparent at $X-M$ line which is the edge of the Brillouin zone. As discussed in earlier section, edge of the Brillouin zone is especially important in CIP-GMR where most electron flows to in-plane direction. The *d* band is much more robust and therefore has lower mobility. The crossing of the *d* band at the Fermi level reduces the scattering contrast between majority- and minority-spin at the FM/NM/FM interfaces, thus reducing MR ratio. Indeed, k_z-dependence of band structure is required to understand more information about the band matching. However, the trend revealed in Figure 5.8 is an indication that addition of Ni into $Co_{50}Fe_{50}$ impact negatively towards the MR ratio of CIP-GMR.

5.3. Summary

In summary we have deposited five spin valves with the structure as seen in Table 5.1 and 5.2. The substitution of $Co_{50}Fe_{50}$ into either NiFe or CoFeNi alloys does have its benefit by having its coercivity reduced from 64 Oe to 4 Oe for $Ni_{25}Fe_{75}$, 29 Oe for $Co_{45}Fe_{45}Ni_{10}$ and to 12 Oe for the $Co_{40}Fe_{40}Ni_{20}$. Unfortunately, this effect is followed up by the reduction of MR ratio quite severely from 20.7 to 4.8% in the case of $Ni_{25}Fe_{75}$, 15.5% in the case of $Co_{45}Fe_{45}Ni_{10}$ and to 11.3% in the case of $Co_{40}Fe_{40}Ni_{20}$. STEM analysis reveals that spin valve C2 which has lowest MR ratio has its structure degraded, possibly due to increased lattice mismatching to MgO. Its Cu spacer is noticeably having multiple phases which might be the main reason for the large reduction in MR ratio. This is somewhat alleviated in spin valve C1. By only having the free layer changed into $Co_{40}Fe_{40}Ni_{20}$, the structure is stabilized by $Co_{50}Fe_{50}$ resulting in much coherent epitaxial growth compared to C2. The bcc-Cu is also confirmed without any sign of other phases. However, MR ratio is still reduced to 16.6% in the case of spin valve C1. First-principles calculation on the band structure reveal that band matching of the FM to bcc-Cu is reduced as Ni content increases. Overall, this approach produces mixed result. In the positive side, coercivity does see reduction. However, the MR ratio is reduced as well. Optimization of the Co-Fe-Ni composition is necessary to find the suitable compound exhibiting both large MR ratio and low coercivity. The use of composite free layer can also suppress the reduction of CIP-GMR.

Chapter 6: Epitaxial bcc-Cu-based current-in-plane giant magnetoresistance on Si substrate

In previous sections, spin valves with various combination of materials have been investigated. Ultimately, epitaxial spin valve device with the combination of bcc-$Co_{50}Fe_{50}$ and bcc-Cu is the one that lead to huge improvement of magnetoresistance at room temperature. However, this epitaxial device can only be grown on single crystalline MgO (001) substrate. This substrate currently is considered impractical due to can only be produced in small size and relatively expensive. More industrially viable substrate such as Si or glass substrates can be used as an alternative.

Si substrate or the thermally oxidized variant is commonly used in the chip industry. Unlike MgO, Si wafer can come with various size up to the larger 30 mm diameter size. It is also common to see Si substrates used in CIP-GMR devices. In the early development time of CIP-GMR spin valve, Ta seed layer is used on top of thermally oxidized Si substrate to orient the growth direction of the fcc FM (NiFe, CoFe) and AFM (FeMn, PtMn or IrMn) layers towards (111) direction[45,81,129–131]. Additionally, the wettability of Ta on thermally oxidized Si substrate is relatively good, resulting in relatively smooth surface roughness and sizeable grain size (~10 nm) of this seed layer. Later improvement introduces NiFeCr seed layer which has similar but better properties to Ta. It quickly becomes seed layer of choice used in tandem or even substituting Ta entirely in the GMR spin valve stacking[126,132–136]. NiFeCr has tendency to grow to (111) direction which is suitable to grow various fcc FM and AFM layers. Wettability on oxide substrates such as AlO_x or SiO_x is excellent, which make the grain size of this layer very large (~50 nm).

Due to the discovery of CoFe/MgO TMR device, the research on obtaining epitaxial growth of CoFe on Si substrate gain some interests. For example, CoFe was deposited on Si (111) substrate using optimized molecular beam epitaxy (MBE) with great success resulting in highly (111)–oriented epitaxial CoFe layer[137]. Seed layer such as Fe_3Si and Ge were also used to grow epitaxial CoFe layer on Si (111) substrate[138]. The deposition of Mg/MgO underlayer using electron beam evaporation on Si (100) has successfully grow highly (100)–oriented CoFe layer[139]. Recently, Chen *et al.* has successfully obtained fully epitaxial CPP-GMR device using NiAl seed layer with magnetoresistance properties close to the one grown on single crystal MgO substrate[140,141]. Similar method was also used by Yakushiji *et al.* to obtain epitaxial TMR device with spinel-type Mg-Al-O tunnel barrier with large TMR ratio of 240% at RT[142]. These examples show that it is possible using Si substrate to obtain epitaxial growth of bcc-CoFe layer which is the main FM layer in the bcc-CoFe/Cu spin valve described in this thesis.

6.1. Preliminary work: The bcc-Cu-based CIP-GMR on amorphous SiO_x substrate

To start the substitution of the substrate from MgO to other—more industrially viable—substrates, a baseline/benchmark needs to be established. Excellent magnetoresistance properties were shown by bcc-CoFe/Cu–based CIP-GMR devices grown on MgO substrate, therefore when the substrate is changed, how far the performance is and a method of how to overcome this gap need to be thought. In this section, amorphous thermally oxidized Si (SiO_x) substrate was used instead of single crystal MgO substrate. This substrate is selected because it is suitable for CIP-GMR devices due to its insulating properties. Oxide surface with very smooth surface roughness of the substrate also provide some sort of specular reflective properties which may enhance MR ratio.

6.1.1. Experiments and Results

A pre-study of how CoFe layer grows on SiO_x was conducted. First sample is 6 nm of CoFe deposited at RT on bare SiO_x substrate by sputtering, whereas subsequent samples are grown with 5, 10 and 20 nm of MgO seed layer. MgO is naturally oriented to (001) direction when grown on amorphous substrate which is suitable to be used as seed layer to induce (001)–oriented growth of CoFe layer. Prior to deposition, SiO_x substrates was cleaned using deionized water, followed by acetone and isopropyl alcohol for 10 minutes each.

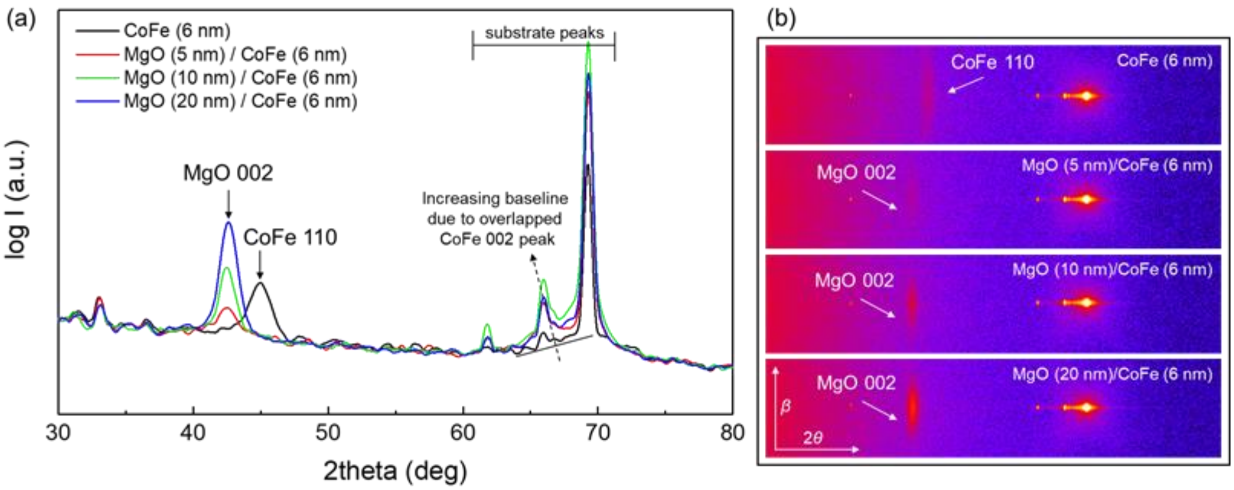

Figure 6.1 (a) XRD profiles for 6 nm of CoFe layer grown on SiO_x substrate with 0, 5, 10 and 20 nm MgO seed layer. (b) The two-dimensional XRD image along 2θ and β direction is also included.

CoFe show natural (110)–oriented growth when grown directly on SiO_x substrate indicated by the appearance of CoFe 110 peak at 45° as shown in Figure 6.1(a). Figure 6.1(b) shows the spread of this peak along β direction which indicate polycrystalline growth of this layer. MgO seed layer on amorphous SiOx substrate naturally grows to (001) orientation, similar orientation to the single crystal MgO substrate used in epitaxial CIP-GMR device in Chapter 4. The 110 peak of CoFe completely disappear and 002 peak of MgO start to appear at 2θ of 42° with increasing intensity as the MgO thickness increases. The β spread is also less compared to CoFe 110 peak in the case without seed layer which indicate polycrystalline with more textured growth of the MgO layer. CoFe 002 peak which is expected to appear around 65° cannot be found. This might be due to overlap with substrate peaks around the same region. However, some noticeable increase of baseline can be noticed for samples with MgO seed layer around 65° which might be from 002 peak of CoFe layer or just from imperfect background correction. This result shows that with just amorphous substrate CoFe will grows oriented to (110) direction. However, with the help of MgO seed layer, (001)–oriented growth of CoFe can be obtained.

Then, bcc-CoFe/Cu–based CIP-GMR devices was deposited on amorphous SiO_x substrate and then compared with the one grown on single crystal MgO substrate. The stacking structure of the samples are as follows:

1. MgO (sub): MgO(sub)/ CoFe(6 nm)/ Cu(t_{Cu} nm)/ CoFe(6 nm)/ IrMn(8 nm)/ cap
2. SiO_x(sub): SiO_x(sub)/ CoFe(6 nm)/ Cu(t_{Cu} nm)/ CoFe(6 nm)/ IrMn(8 nm)/ cap
3. SiO_x(sub)/MgO: SiO_x(sub)/ MgO(10 nm)/ CoFe(6 nm)/ Cu(t_{Cu} nm)/ CoFe(6 nm)/ IrMn(8 nm)/ cap

Cu thickness (t_{Cu}) of all films is varied from 0–5 nm. The SiO_x(sub)/MgO spin valve act as a bridge between (110)–oriented polycrystalline growth of bare amorphous SiO_x substrate and (001)–oriented epitaxial growth of single crystal (001)–oriented MgO substrate. All samples are deposited at room temperature and then annealed at 250°C for 1 hour under 3 kOe constant external magnetic field.

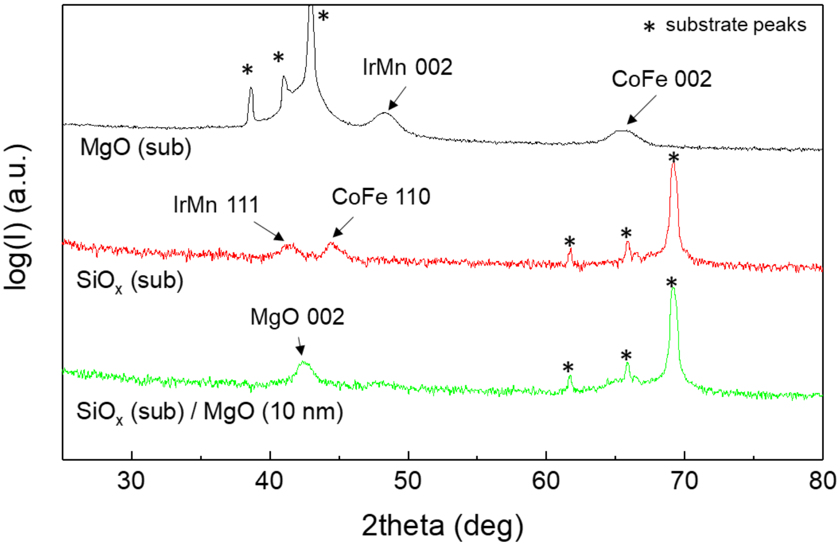

Figure 6.2 The 2θ XRD profiles of MgO (sub), SiO_x (sub) and SiO_x (sub)/MgO spin valves. Substrate peaks from MgO and SiO_x substrates are marked with asterisks.

Figure 6.2 shows the 2θ XRD profiles of all three spin valve devices. MgO (sub) spin valve shows (001)–oriented growth indicated by IrMn 002 and CoFe 002 peak at 48° and 65°, respectively. Almost all peak from this sample, especially peaks from IrMn 002 and CoFe 002 mentioned earlier are absent from the SiO_x (sub) multilayer. Instead, IrMn 111 and CoFe 110 appears indicating the difference in growth orientation between MgO (sub) and SiO_x (sub) films. SiO_x(sub)/MgO spin valve film shows (001)–oriented growth indicated by the peak of MgO 002 around 42° similar to what happened to MgO(10 nm)/CoFe(6 nm) in Figure 6.1. Peak of IrMn and CoFe in this sample is barely noticeable. Very weak bump/broad peak can be found around 48° and 65° which might be attributed to weak out-of-plane texturing of IrMn 002 and CoFe 002 peak.

After microfabrication process, the film becomes sets of 200 μm × 3350 μm strips. The magnetoresistance properties then measured at RT with four-point prober. Figure 6.3(a) shows spin valve–type behavior on all devices with increasing MR value as t_{Cu} decreases. At certain critical thickness, MR ratio starts to go down towards zero due to increased ferromagnetic exchange coupling at low t_{Cu}. MgO (sub) spin valve show largest maximum MR ratio value of 24.9% at t_{Cu} = 1.9 nm. SiO_x (sub) and SiO_x (sub)/MgO spin valves have similar maximum MR ratio of 13.4 and 12.6% at t_{Cu} = 2.9 and 4.3 nm, respectively. The MR curve of MgO (sub) spin valve at t_{Cu} = 3 nm in Figure 6.3(b) exhibit MR ratio of 20.1% with narrow antiparallel state due to relatively small exchange bias field of 5.5 mT. Although the MR ratio is smaller, only at 13.2%, SiO_x (sub) spin valve at t_{Cu} = 3 nm in Figure 6.3(c) show larger exchange bias of 16.9 mT. The coercivity of both free and pinned layer in SiO_x (sub) spin valve is larger compared to MgO (sub) spin valve which can be explained due to domain wall pinning in the case of polycrystalline device.

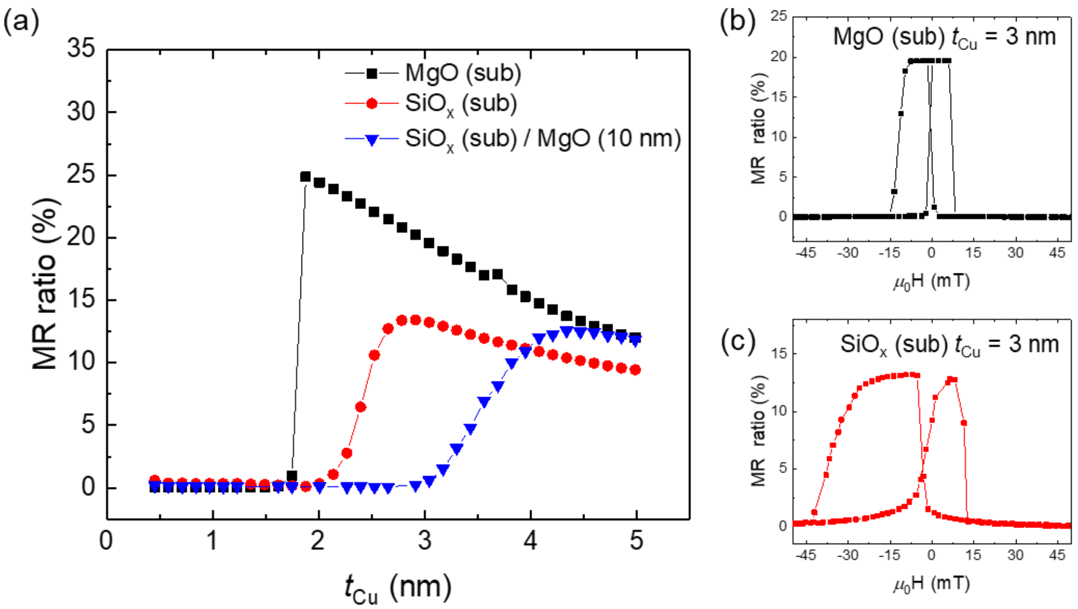

Figure 6.3 (a) Cu thickness (t_{Cu}) dependence of MR ratio for MgO (sub), SiO_x (sub) and SiO_x (sub)/MgO spin valves. Magnetoresistance curve of (b) MgO (sub) and (c) SiO_x (sub) spin valves with t_{Cu} = 3 nm are shown as well.

6.1.2. Discussion

To obtain large MR ratio found in the epitaxial (001)–oriented bcc-CoFe/Cu–based CIP-GMR device, two things need to be achieved, namely (001)–oriented and epitaxial growth. In bcc-CoFe/Cu–based CIP-GMR device, both attributes are the driving force of the formation of bcc-Cu which is the main reason for the observed large MR ratio. Figure 6.1 shows that although CoFe naturally grow (110)–oriented, it can be directed towards (001) with the help of

(001)–oriented MgO seed layer. This is also reflected in the 2θ XRD profile of the spin valve devices in Figure 6.2 where CoFe 110 peak from the spin valve film grown directly on SiO_x substrate disappear after the use of MgO seed layer. CoFe 002 seems to appear on SiO_x (sub)/MgO spin valve, but the intensity is rather weak and overlapped with the background substrate peaks. Thus, we have three different sets of spin valve devices: (001)–oriented epitaxial device called MgO (sub) spin valve, (110)–oriented polycrystalline device called SiO_x (sub) spin valve and (001)–oriented polycrystalline device called SiO_x (sub)/MgO spin valve.

The magnetoresistance values of all three spin valve devices are compared in Figure 6.3(a). SiO_x (sub) spin valve show much lower MR ratio compared to MgO (sub) spin valve, possibly due to both not having (001)–oriented and epitaxial growth. The epitaxial device has the benefit of not having grain boundaries which also reduces interlayer defects especially around FM/NM/FM. Because electrons move in-plane direction, grain boundaries and interfacial defects become extra scattering center which does not always spin-dependent. This is what drives down the MR ratio value in polycrystalline device such as SiO_x (sub) spin valve. Slight improvement can be seen in SiO_x (sub)/MgO spin valve. Even though maximum MR ratio is slightly smaller compared to SiO_x (sub) spin valve, the MR ratio values at the same t_{Cu} are larger. The MR ratios are even almost comparable to MgO (sub) spin valve at $t_{Cu} > 4.5$ nm. This might be due to improved growth orientation with the help from 10 nm of MgO seed layer. Other possibility is MgO seed layer make the grain size of subsequent CoFe layer larger which reduce the amount of grain boundaries, thus improving MR ratio[134,143]. However, the critical thickness when of SiO_x (sub)/MgO spin valve the MR ratio start to decline is rather large at $t_{Cu} = 4.3$ nm. Large critical thickness is commonly seen when the multilayer interfacial roughness is high. Rough interfaces of FM/NM/FM induce orange-peel-like coupling[144,145] which increase ferromagnetic interlayer exchange coupling between FM layers. If both FM layers are coupled ferromagnetically, antiparallel state cannot be obtained, and then magnetoresistance effect will fail to appear. The extra 10 nm of MgO seed layer possibly resulted in rougher surface compared to bare MgO or SiO_x substrates which consequently increase this critical thickness. The critical thickness of SiO_x (sub) spin valve is larger at $t_{Cu} = 2.9$ nm compared to 1.9 nm in the case of MgO (sub) spin valve due to similar reason. In the MgO (sub) spin valve, MR ratio reduces from maximum value to almost zero immediately which indicate the homogeneity of the layer thickness and better interfacial smoothness for this device.

The coercivity of the FM layers in SiO_x (sub) spin valve is larger compared to MgO (sub) spin valve which is due to domain wall pinning via grain boundaries. Large coercivity of the free layer is not desired because it introduces error when the device is used as sensor. It is also worth noting that the SiO_x (sub) spin valve exhibit significantly larger exchange bias field compared to MgO (sub) spin valve. This might be related to the growth orientation of IrMn, because in general the pinning strength of IrMn is the largest when it has (111)–oriented growth[103,113].

In summary, MR ratio of the polycrystalline devices are much lower compared to the epitaxial one. Partly because the reduction of MR ratio due to grain boundaries and interfacial defects, also due to much larger critical thickness. The increase of MR ratio at the same t_{Cu} after the addition of MgO seed layer also signify the importance of having (001)–oriented growth.

6.2. Epitaxial bcc-Cu-based current-in-plane giant magnetoresistance on Si substrate

As seen in previous section, there is still long distance to overcome in terms of increasing MR performance of the device grown on amorphous substrate. The biggest hurdle is suppressing factors that reduce MR ratio such as grains and crystal defects in polycrystalline device by growing epitaxial device instead with still using industrially viable substrate. In this section, such attempt is described, namely epitaxial growth of bcc-CoFe/bcc-Cu-based CIP-GMR device on Si (001) substrate by using NiAl as underlayer. The use of NiAl underlayer on top of Si substrate is inspired by previous work from Chen et al. on CPP-GMR which results in MR ratio close to the one deposited on single crystal MgO substrate[71,146]. Similar method was also used to fabricate TMR device resulting in the formation of spinel-type single crystal Mg-Al-O tunnel barrier with MR ratio up to 240% at RT[142]. This method is also promising for CoFe-based CIP-GMR because NiAl and CoFe has similar bcc structure with small lattice mismatch (<2%). However, modification of the method has to be made. Because any conductive layer which does not contributes to CIP-GMR will reduce MR ratio, insulating the GMR layers from the seed layer is extremely important. In this work, MgO insulation layer and microfabrication was used to make sure that only conduction inside GMR layers is measured.

6.2.1. Experiments and Results

To obtain epitaxial NiAl layer, optimization of the deposition condition is necessary. 20 nm of NiAl layers were deposited on Si substrate at deposition temperature (T_d) of 300, 400, 500 and 600°C. The Si substrate used were chemically cleaned from surface oxide using dilute 3% HF solution prior to deposition. To check whether the deposited NiAl was epitaxial or not, its surface was measured by reflection high-energy electron diffraction (RHEED) in-situ after the deposition. To check the growth orientation, XRD was measured.

At T_d = 300°C, NiAl has (110)–oriented growth indicated by the NiAl 110 peak at 44° as shown in Figure 6.4(a). This peak also appears as a widely spread to β direction in the 2D XRD image which together with the ring-like pattern of RHEED pattern in Figure 6.4(b) suggest the polycrystalline growth of NiAl. At T_d = 400°C, (001)-textured NiAl layer start to form indicated by the increasing intensity of NiAl 001 and NiAl 002 peaks. Its RHEED pattern start to show spots which indicate textured growth although the ring-like pattern is still noticeable. At T_d = 500 and 600°C, intensity of NiAl 001 and NiAl 002 peaks become stronger, all ring-like pattern in the RHEED image disappear which suggests complete epitaxial growth of NiAl layer.

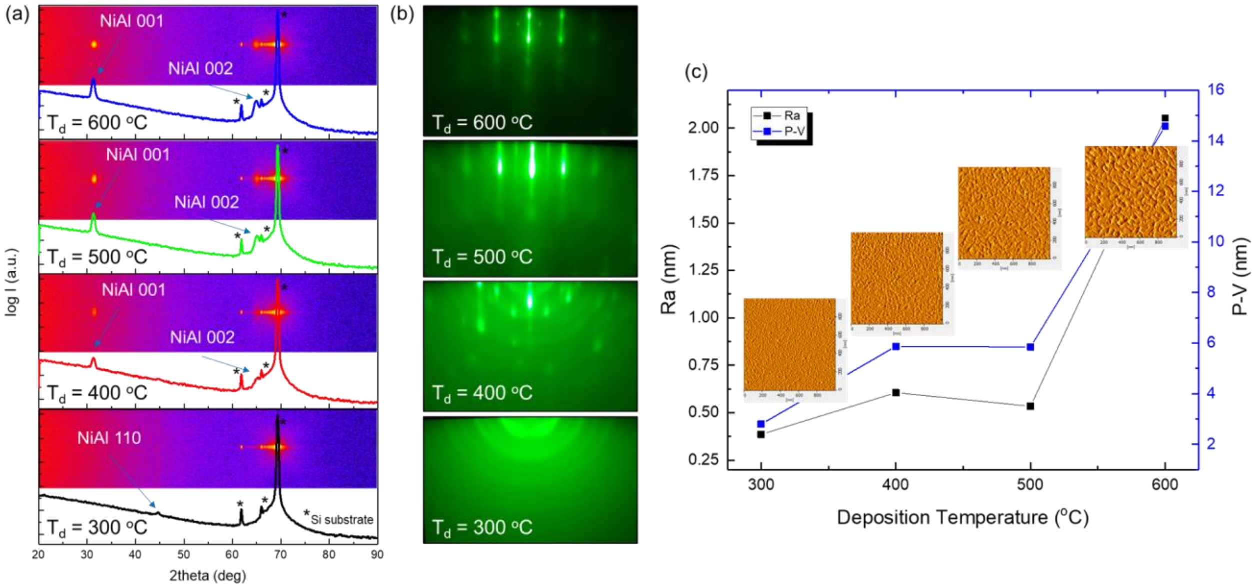

Figure 6.4 (a) Two-dimensional XRD pattern and its profile for NiAl deposited at 300, 400, 500 and 600°C. (b) RHEED pattern on the surface of NiAl taken after the deposition. (c) Average surface roughness, Ra, and peak-to-valley value, P-V, of NiAl for each deposition temperature.

As learned from the work on polycrystalline CIP-GMR devices described in previous section, large roughness for an underlayer in CIP-GMR is detrimental because it will lead to larger interfacial roughness at FM/NM interface. This will induce stronger ferromagnetic coupling via Néel's orange peel mechanims[145] which might results in large critical thickness. Therefore, the surface roughness of NiAl layer become part of consideration beside the epitaxial growth when choosing the deposition parameters. The surface roughness of the 20 nm single layer NiAl deposited at T_d = 300, 400, 500 and 600°C were measured using an atomic force microscope (AFM). Figure 6.4(c) shows the increase of surface roughness as T_d increases which is direct result of having increased atomic mobility at larger temperature. Balance between high textured growth and low surface roughness is necessary. Therefore 500°C temperature is selected for the deposition of NiAl layer.

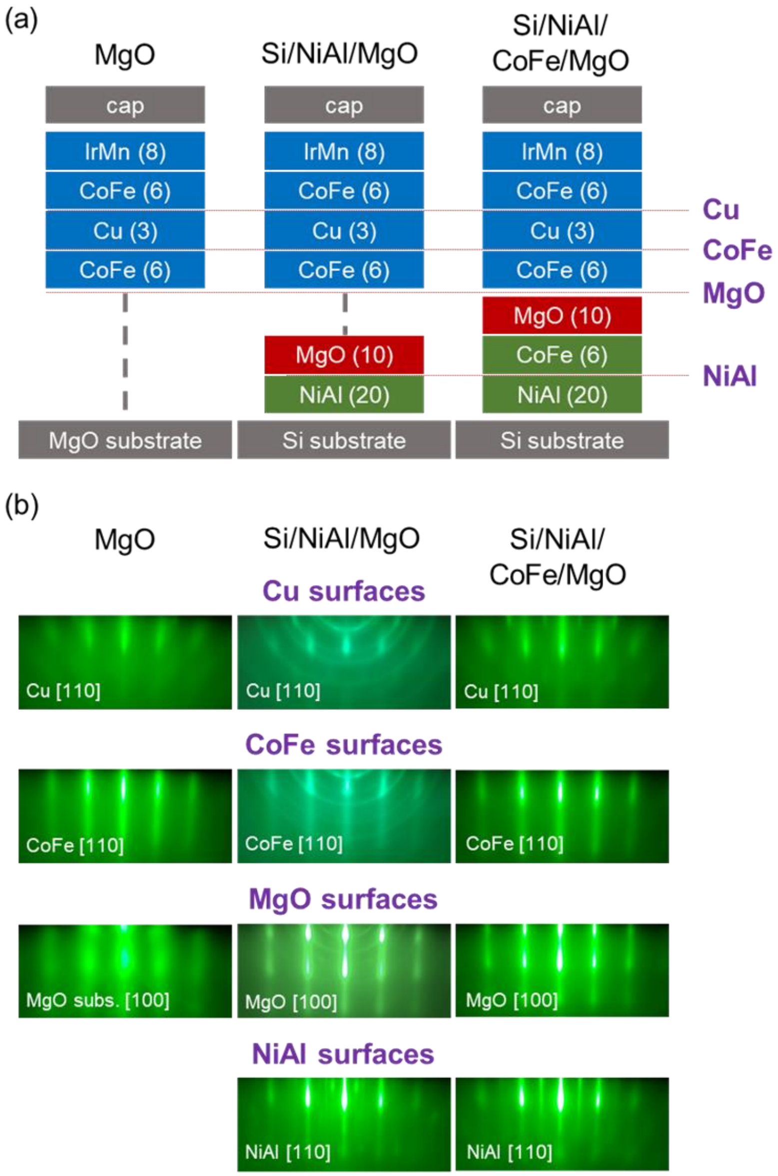

Figure 6.5 (a) Schematic illustration of MgO, Si/NiAl/MgO and Si/NiAl/CoFe/MgO SVs. (b) RHEED patterns from select layers are presented.

The next step is realizing the epitaxial spin valve device on Si substrate by using optimized NiAl deposition condition. However, it is not as straightforward as putting CIP-GMR stacking on epitaxial NiAl layer. In CIP-GMR devices, it is important to control the amount of metallic layers involved in the electronic transport. Because of its in-plane nature, any additional conductive channel which does not contributes spin-dependent scattering will reduce magnetoresistance, in this case is the 20 nm NiAl layer. Therefore, applying insulation to avoid shunting through the underlayer is necessary. Thus, three different spin valves were designed and fabricated as follows:

1. MgO: MgO (001) substrate/CoFe(6 nm)/Cu(3 nm)/CoFe(6 nm)/IrMn(8 nm)/cap

2. Si/NiAl/MgO: Si (001) substrate/NiAl(20 nm)/MgO(10 nm)/CoFe(6 nm)/Cu(3 nm)/CoFe(6 nm)/IrMn(8 nm)/cap
3. Si/NiAl/CoFe/MgO: Si (001) substrate/NiAl(20 nm)/CoFe(6 nm)/MgO(10 nm)/CoFe(6 nm)/Cu(3 nm)/CoFe(6 nm)/IrMn(8 nm)/cap

In this study, the MgO layer in Si/NiAl/MgO and Si/NiAl/CoFe/MgO SVs have a role to prevent current conduction through the conductive seed layers. Note that all samples have the core CIP-GMR of CoFe(6 nm)/Cu(3 nm)/CoFe(6 nm)/IrMn(8 nm) as depicted in Figure 6.5(a) by blue color. Substrates are chemically cleaned using deionized water, acetone and then isopropyl alcohol in subsequent order. MgO substrate was etched by Ar ion milling whereas Si substrates were chemically etched by dilute 3% HF solution for 15s prior to deposition. All samples were deposited at room temperature except for NiAl layers which were deposited at optimal 500°C to achieve epitaxial growth. After finishing each deposition, RHEED patterns were taken from [100] azimuth of MgO substrate/layers. All samples were annealed at 250°C for 1h under 3kOe magnetic field. XRD was also measured to check its growth orientation.

Figure 6.5(b) shows the RHEED pattern of the surface of NiAl, MgO, CoFe and Cu. MgO SV show streak patterns for all layers which indicating (001)-oriented epitaxial growth. NiAl layers of Si/NiAl/MgO and Si/NiAl/CoFe/MgO SVs show streak pattern suggesting (001)-oriented growth of this layer. Afterwards all other layers of Si/NiAl/MgO and Si/NiAl/CoFe/MgO SVs very similar streak pattern to that of MgO SV with some caveat. Although the pattern on Si/NiAl/CoFe/MgO SV is very clean, that Si/NiAl/MgO SV show the streak pattern mixes with ring-like patterns. It is worth noting that the ring-like pattern only appear for the deposition after NiAl layer in Si/NiAl/MgO SV. These ring-like pattern suggests the polycrystalline growth of Si/NiAl/MgO SV whereas both MgO SV and Si/NiAl/CoFe/MgO SV grow epitaxially.

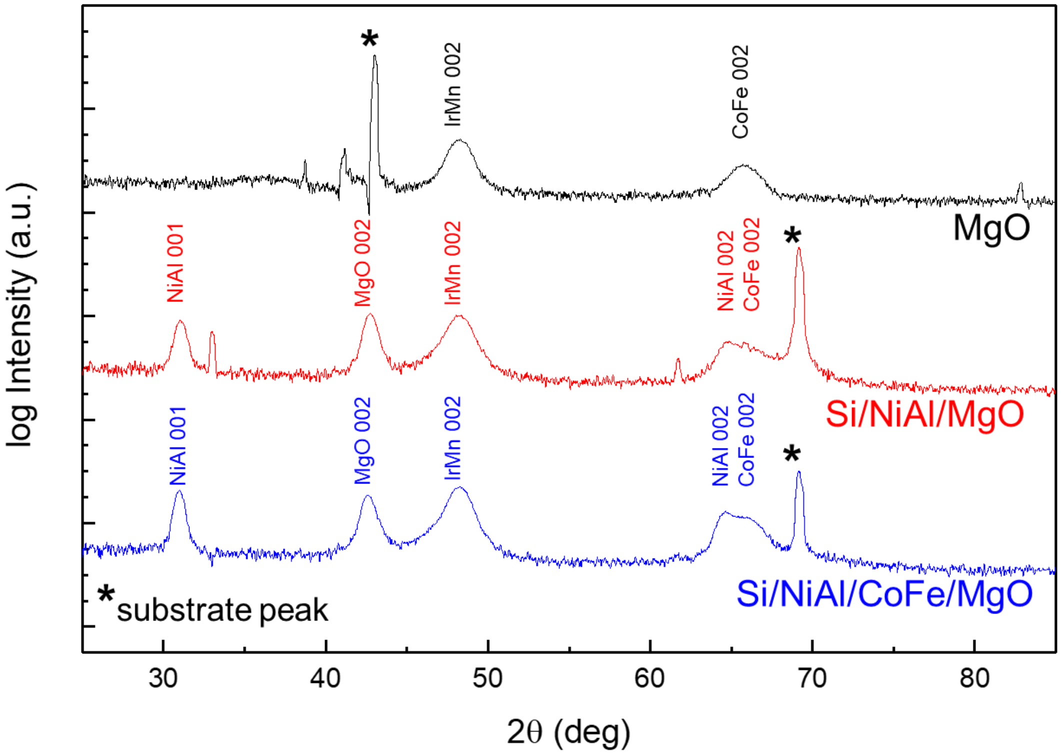

Figure 6.6 XRD graph for MgO, Si/NiAl/MgO and Si/NiAl/CoFe/MgO SVs.

The XRD profiles of the samples shown in Figure 6.6 confirm the (001)-oriented growth of MgO, Si/NiAl/MgO and Si/NiAl/CoFe/MgO SVs. All samples show 002 IrMn at 48.2° suggesting that different underlayers does not impact lattice parameters of the subsequent layers. The 002 CoFe peaks presents at 65.8° for all samples although the one from Si/NiAl/MgO and Si/NiAl/CoFe/MgO SVs are overlapped with the 002 NiAl peak due to similar lattice constant. The presence of NiAl 001, NiAl 002 and MgO 002 peak further support the textured growth of Si/NiAl/MgO and Si/NiAl/CoFe/MgO SVs.

The multilayer films were then fabricated into sets of 200 μm × 3350 μm strips using optical lithography, sputter deposition and Ar ion etching. Because four-point probe measurement which is used to measure MR properties uses probes which might penetrate through 10 nm MgO layer, the insulation is further enhanced by depositing SiO_2 layer during microfabrication. Figure 6.7(a) show the HAADF-STEM and EDS image of Si/NiAl/CoFe/MgO SV at the edge of the film after applying microfabrication. By design, the ion milling process should completely remove all layers down to substrate level. Unfortunately, after ion milling only GMR layers are completely removed at the edge of the device due to the slow etch rate of MgO layer and shadowing effect by the resist. However, this remaining MgO layer actually protect the GMR device from shunting via redeposited metal which can be seen as spike figure. Because MgO layer is retained, redeposited metal does not connect upper GMR layer and the NiAl seed layer. For the measurement, prober should not directly penetrate on top of GMR layer but should use Au contact on the further side where the remaining films completely disappear which is shown in Figure 6.7(b). Even if the prober penetrates this area, shunting will not happen, thus current will only pass the GMR layer.

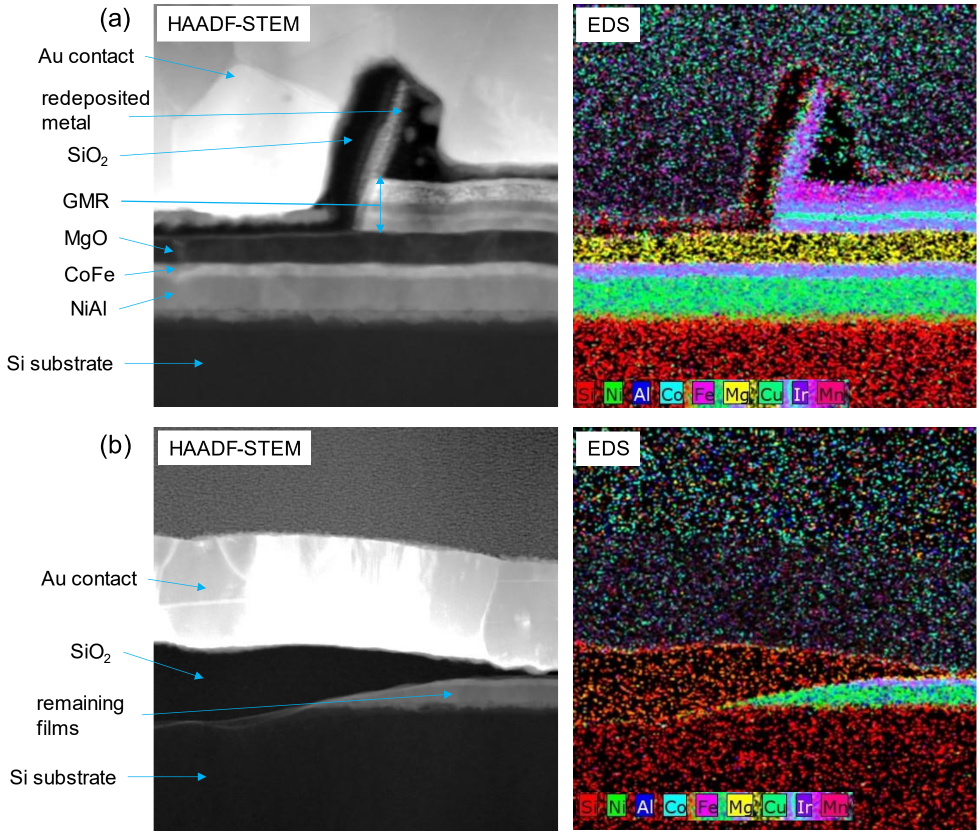

Figure 6.7 HAADF-STEM image and EDS mapping of Si/NiAl/CoFe/MgO SVs at (a) the edge and (b) the far side of a SV device after microfabrication.

The spin valves were measured for both their magnetization and magnetoresistance as shown in Figure 6.8(b). MgO SV show large MR ratio of 20.8% and parallel state resistance (R_P) = 160.3 Ohm. Exchange bias strength is relatively large with the value of 13.4 mT. In the case of Si/NiAl/MgO and Si/NiAl/CoFe/MgO SVs, two structures are examined as seen in Figure 6.8(a), one of them having insulation structure is called isolated device, the other one that does not have insulation structure is called shunted device. Si/NiAl/MgO (Si/NiAl/CoFe/MgO) SV shows increased R_P value from 40.6 (38.5) Ohm in shunted device to 167.2 (138.3) Ohm in isolated device. This increase in resistance indicates that the SiO_2 barrier has successfully prevented the current shunting through the conductive underlayers (NiAl and CoFe). MR ratio of Si/NiAl/MgO (Si/NiAl/CoFe/MgO) also increases from 4.8% (4.5%) in shunted device to 12.0% (15.6%) in isolated device. This significant increase in MR ratio value emphasizes the importance of isolating GMR layers electrically from its supporting conductive underlayers to prevent current shunting. Exchange bias of Si/NiAl/MgO SV is relatively large with the value of 11.2 mT, in contrast to Si/NiAl/CoFe/MgO SV with only 5.4 mT. It is also worth mentioning that the coercivity of both pinned and free layer for Si/NiAl/MgO SV is much larger compared to two other devices. This is related to the polycrystalline characteristic of this device which increase its coercivity via domain pinning at the grain boundaries.

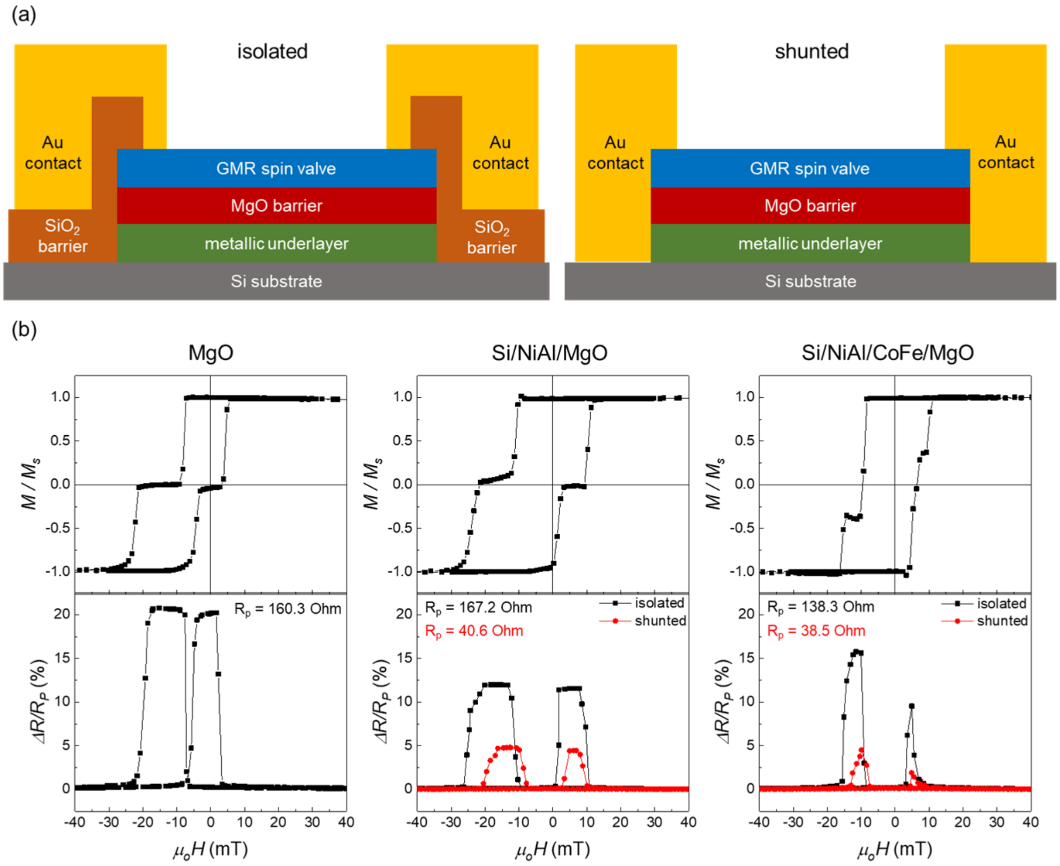

Figure 6.8 (a) Schematic illustration of both isolated and shunted devices. (b) Magnetization and magnetoresistance curve for MgO, Si/NiAl/MgO and Si/NiAl/CoFe/MgO SVs.

Currently, epitaxial bcc-CoFe/bcc-Cu based CIP-GMR has been successfully fabricated on Si substrate as seen in Si/NiAl/CoFe/MgO SV indicated by the lack of ring-like pattern on RHEED image similar to MgO SV. However, the MR ratio is still far from that of MgO SV. To understand the reason for this difference in MR ratio value, more detailed information about the structure is needed, especially about the epitaxial growth of the GMR film and the formation of bcc-Cu. Vertical slice of the sample was made using focused-ion beam (FIB) and then thinned down to 30-50 nm before then observed under the TEM. The plane of observation is from the [100] azimuth of MgO substrate (layers) in the case of MgO (Si/NiAl/MgO and Si/NiAl/CoFe/MgO) spin valve. High resolution high-angle annular dark field scanning TEM (HAADF-STEM) images at high and low magnification were obtain from each spin valves. Nano-beam electron diffraction patterns (NBED) were also checked to determine the crystal structure and the orientation of each layer. Energy dispersive X-ray spectroscopy (EDS) were performed at low magnification to check the elemental distribution and interdiffusion if there is any.

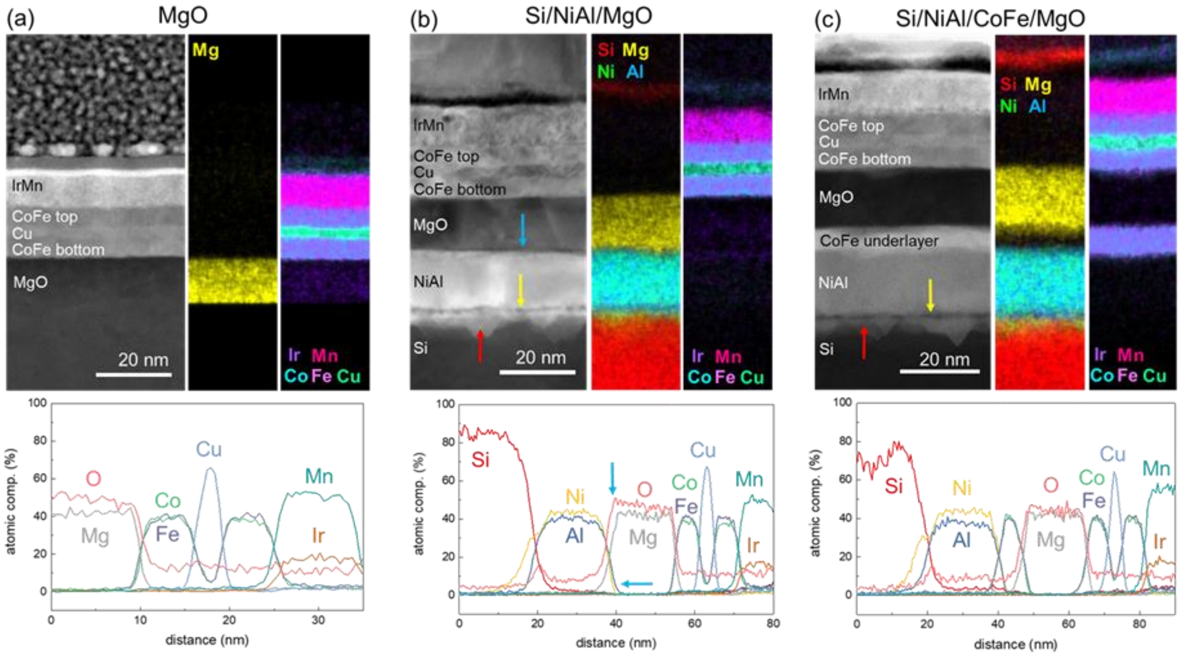

Figure 6.9 HAADF-STEM image as well as EDS mapping and line profile of (a) MgO, (b) Si/NiAl/MgO and (c) Si/NiAl/CoFe/MgO SV.

Figure 6.9 show the high-angle annular dark field scanning TEM (HAADF-STEM) as well as energy dispersive X-ray spectroscopy (EDS) elemental mapping and line profile for MgO, Si/NiAl/MgO and Si/NiAl/CoFe/MgO SVs. MgO SV show smooth interface with no noticeable interdiffusion. Si/NiAl/MgO and Si/NiAl/CoFe/MgO SVs also grow similarly especially the GMR layers. The composition of each layer also seems to be correct, for all samples in this case. However, there are few notable differences compared to MgO SV. Firstly, both Si/NiAl/MgO and Si/NiAl/CoFe/MgO SVs show the formation of nickel silicide at the Si/NiAl interfaces due to the reaction between Ni and Si which are visible as gray contrasts in HAADF-STEM image and EDS, indicated by red arrows in Figure 6.9(b) and (c). This is caused by the diffusion of Ni into Si matrix as seen in the EDS line profile, driven by the heat treatment performed during NiAl deposition. The diffusion rate of Ni into Si is larger than the opposite, mostly almost one–way, which cause deficiency of Ni in the NiAl layer. This deficiency of Ni in the NiAl creates thin Al–rich layer as shown by yellow arrow in Figure 6.9(b) and (c). This Kirkendall void–like feature is very similar to what was reported by Chen et al[71,146,147]. The formation of nickel silicide also roughens the bottom interface of NiAl layer. However, this does not seem to affect the surface of NiAl layer prior to the deposition of the next layer. As seen from the figures, the top interface of NiAl and consequently the subsequent layers in both Si/NiAl/MgO and Si/NiAl/CoFe/MgO SVs are relatively flat. Another point worth noting is that in the Si/NiAl/MgO SV, there appear to show small mixing of Al and O at the NiAl/MgO interface, pointed by blue arrows in Figure 6.9(b). This feature is unique for Si/NiAl/MgO SV and cannot be seen in the other two samples.

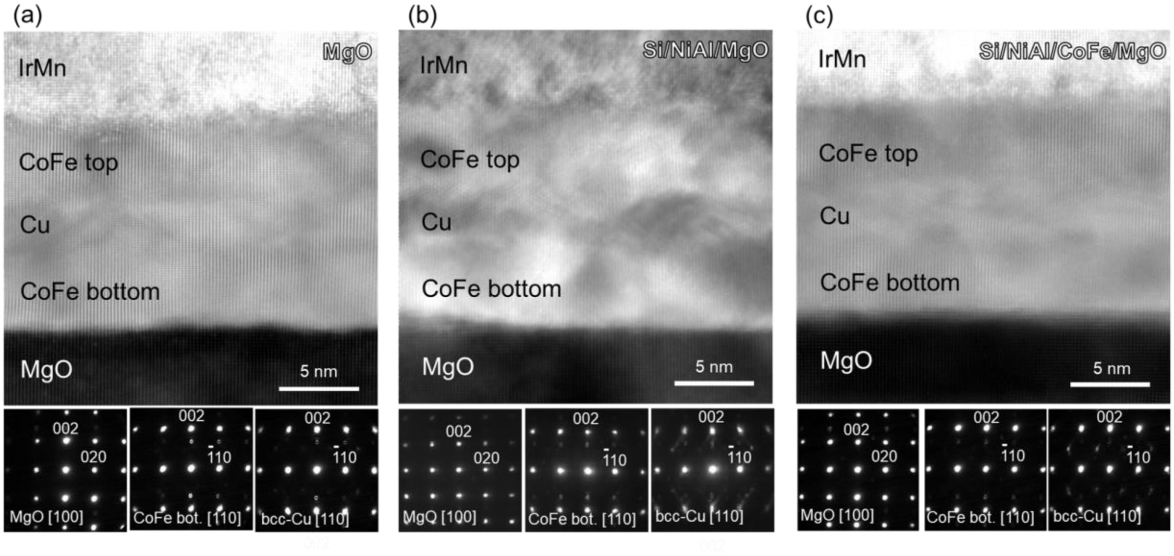

Figure 6.10 HAADF-STEM images of (a) MgO, (b) Si/NiAl/MgO and (c) Si/NiAl/CoFe/MgO SV with the NBED pattern for MgO, CoFe and Cu layers.

Next, the microstructure of the SV samples is described. Please note that the MR ratio of MgO SV is much larger compared to both Si/NiAl/MgO and Si/NiAl/CoFe/MgO SVs. It means that any difference in the structure of Si/NiAl/MgO and Si/NiAl/CoFe/MgO SVs from MgO SV might be the reason of the reduction in MR ratio values. Figure 6.10 shows the HAADF-STEM image of MgO, Si/NiAl/MgO and Si/NiAl/CoFe/MgO SVs with NBED pattern of MgO, CoFe bottom and Cu layers. All samples show (001)-oriented growth of CoFe layers as demonstrated by the XRD and RHEED patterns. The growth orientation in general across all samples is MgO(001)[100]//CoFe(001)[110]//bcc-Cu(001)[110]. The HAADF-STEM images of MgO SV and Si/NiAl/CoFe/MgO SV in Figure 6.10(a) and (c) respectively confirms the epitaxial growth of these devices. Atomic column are presents seamlessly spanning across CoFe/Cu/CoFe in both devices with very minimal to no defects. Overall, both samples show very similar looks in terms of structure from the HAADF-STEM image. However, some differences can be noticed somewhere else. The NBED pattern of MgO and CoFe layers are similar in both samples. However, despite all the similarities between both samples, the NBED pattern of Cu from Si/NiAl/CoFe/MgO SV is different. It shows additional reflections which does not belong to bcc-Cu which does not present in MgO SV. This might be the reason for reduced MR ratio in Si/NiAl/CoFe/MgO SV.

As for Si/NiAl/MgO SV, it shows poor growth as seen in Figure 6.10(b) which agrees with previous result of RHEED pattern suggesting the polycrystalline growth of this spin valve. Similar to Si/NiAl/CoFe/MgO SV, the NBED pattern of MgO and CoFe bottom layer is similar to the MgO SV. However, the NBED pattern of Cu spacer in this sample is very different from the other two devices. On top of expected bcc reflections from the bcc-Cu, it has many visible strain marks. This appears possibly from the twinning or stacking faults caused by grain boundaries and lattice mismatches in this device.

6.2.2. Discussion

MgO SV shows large MR ratio with the value of 20.8% at RT. This can be achieved due to the formation of bcc-Cu and excellent epitaxial growth of this device as seen in Figure 6.10 which has been discussed in Chapter 4. Both Si/NiAl/MgO and Si/NiAl/CoFe/MgO SVs show much lower MR ratio which is closely related to the difference in the microstructure of both samples compared to MgO SV.

Si/NiAl/MgO SV show polycrystalline growth, which introduce many imperfections inside the structure and negatively impacts MR ratio. This polycrystalline growth still happened despite the NiAl layer in this sample already grow epitaxially as seen in the RHEED pattern in Figure 6.5(b). The cause of this polycrystalline growth is hinted by the mixing of Al and O elements in the EDS line profile from Figure 6.9(b). This mixing can be explained as the formation of Al–O compound at NiAl/MgO interface which appear as thin–dark contrast in the HAADF-STEM image at NiAl/MgO interface. The Al–O forms due to the exposure of Al elements in NiAl to the O plasma during the deposition of MgO. Because Ni is less prone to oxidation compared to Al, only Al forms oxide layer[148,149]. Al–O might have poor lattice matching to MgO or even have amorphous structure which cause MgO cannot grow epitaxially on it like when it grows directly on NiAl. Thus, MgO grow polycrystalline which cause the GMR layer also grow as such. This effect is somehow alleviated with the addition of CoFe at NiAl/MgO interface like in Si/NiAl/CoFe/MgO SV. Similar to Ni, both Co and Fe are also not as easy to oxidize compared to Al which consequently keep the epitaxial growth of the subsequent layers.

Not only Si/NiAl/MgO SV, but also both spin valves in previous section which were deposited on amorphous substrates that show polycrystalline growth, namely SiO_x (sub) and SiO_x (sub)/MgO SVs. Thus, it is interesting to compare their MR ratio. According to its multilayer stacking and crystal structure, Si/NiAl/MgO SV is very similar to SiO_x (sub)/MgO SV with (001)–oriented polycrystalline growth. The thin Al–O at the NiAl/MgO interface works more or less the same way with the amorphous SiO_x substrate. However, GMR effect can be seen in full effect for SiO_x (sub)/MgO SV at $t_{Cu} > 4.3$ nm, thus direct comparison at $t_{Cu} = 3$ nm cannot be done. Even so, MR ratio of SiO_x (sub)/MgO SV is larger with 12.6% at $t_{Cu} = 4.3$ nm compared to 12.0% in the case of Si/NiAl/MgO SV. They are slightly below the MR ratio of SiO_x (sub) SV at the same $t_{Cu} = 3$ nm with the value of 13.2%. Because device size and multilayer stacking during measurement is similar between Si/NiAl/MgO, SiO_x (sub) and SiO_x (sub)/MgO SVs, the resistance when the magnetization is parallel (R_P) can be compared. Si/NiAl/MgO, SiO_x (sub) and SiO_x (sub)/MgO SVs show R_P = 167.2, 114.7 and 133.9 Ohm respectively. Larger R_P in Si/NiAl/MgO SV can be caused by many things, notably interfacial roughness, grain size and internal lattice defects especially inside Cu spacer[134,143,150,151]. Electron travelling can be scattered at the scattering center such as grain boundaries or any point defects which reduce mean–free path of the electron, thus increasing resistivity. Lower MR ratio in Si/NiAl/MgO compared to other polycrystalline devices is most likely due to this problem as well. Additional scattering center that is not spin-dependent will increase the R_P value but not the ΔR, resulting in lower MR ratio.

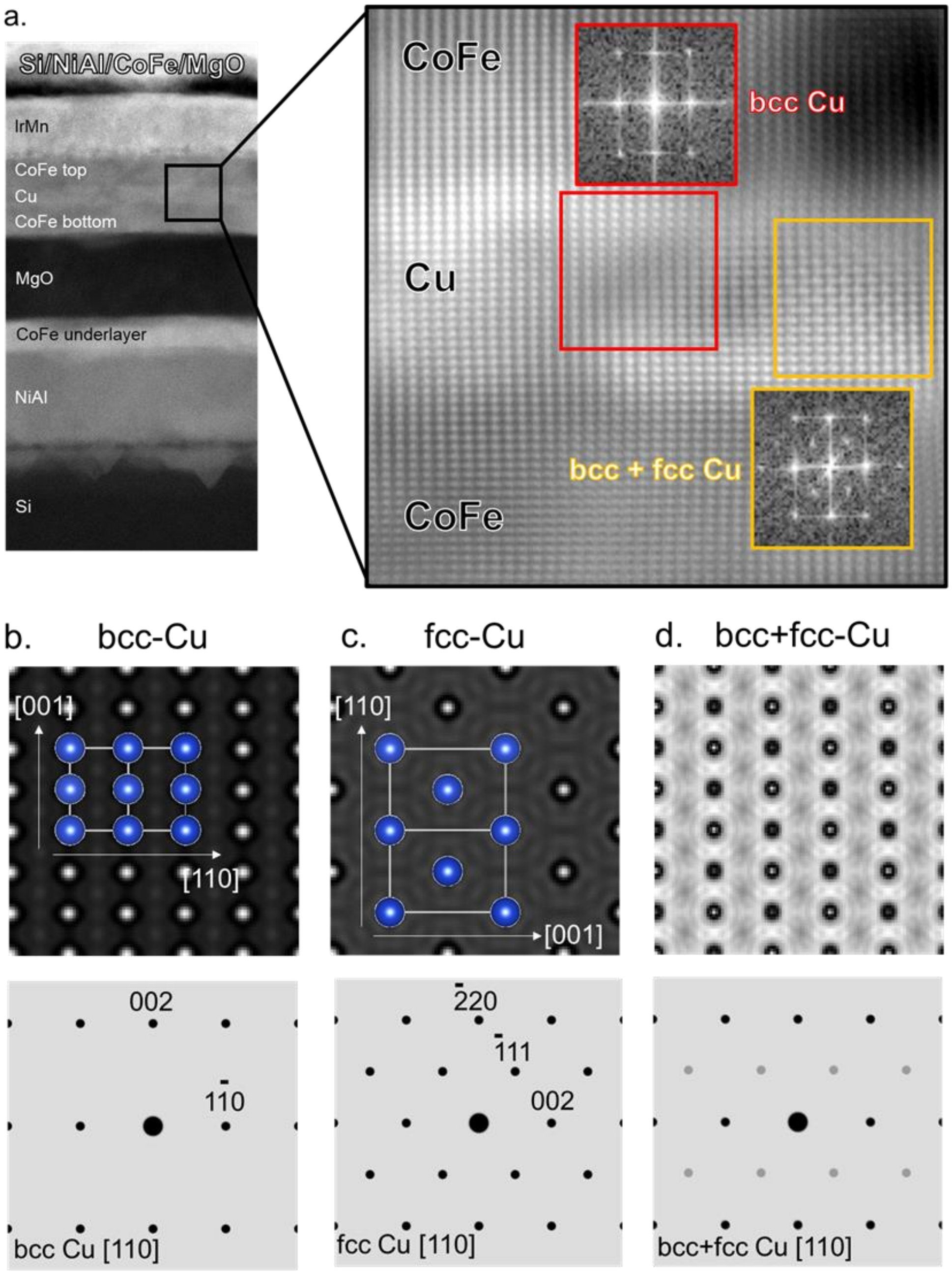

Figure 6.11 (a) Magnified HAADF-STEM image of Si/NiAl/CoFe/MgO SV showing two different area with their FFT patterns. Simulated STEM and diffraction pattern of (b) bcc-Cu, (c) fcc-Cu and (d) their overlays are presented.

More important comparison is between MgO and Si/NiAl/CoFe/MgO SVs. Even though both show epitaxial growth, MR ratio of Si/NiAl/CoFe/MgO SV is much lower compared to MgO SV. In terms of microstructure, difference between two samples can be spotted in the NBED pattern of Cu layer in Si/NiAl/CoFe/MgO SV. Ideally bcc-Cu is desired to obtain large MR ratio in this bcc-CoFe/Cu system as seen in MgO SV. However, NBED pattern of Si/NiAl/CoFe/MgO SV show additional reflection which does not belong to bcc-Cu. To understand the origin of this reflection, detailed analysis is performed. Figure 6.11(a) show larger magnification HAADF-STEM image of Si/NiAl/CoFe/MgO SV. Two area in the figure, exhibit different feature which is indicated by different Fast-Fourier Transformation (FFT) pattern. In the red inset, bcc-Cu is shown in both DF and FFT images. On the other hand, the one in the yellow inset show the additional reflection seen in NBED image of Cu in Figure 6.10(c). It is identified that the extra reflections come from fcc-Cu in which its lattice is expanded to match lattice constant of bcc-Cu and bcc-CoFe with the orientation of (001)[110]bcc-Cu//(110)[001]fcc-Cu. Figure 6.11(b-d) show simulated STEM images and diffraction pattern for bcc-Cu and fcc-Cu. The diffraction pattern of fcc-Cu falls exactly in the spot where the extra reflection appears. The STEM simulation suggests that in the STEM image from fcc-Cu in this orientation will looks like bcc-Cu with voids in between. TEM specimen of this sample which thickness is ~100 nm is most likely enough to contain more than one phase which overlaps to each other. Overlapping the bcc and fcc Cu will create checkerboard-like contrast which resemble the image in the yellow inset in Figure 6.11(a). In this orientation, normally fcc-Cu has ~10% lattice mismatch to either bcc-CoFe or bcc-Cu. In this case, Cu lattice constant is expanded so that it will fit inside the bcc matrix.

This additional fcc phase is the only difference which can be spotted between MgO and Si/NiAl/CoFe/MgO SV. Currently there is no proof either experimentally or by simulation that fcc-Cu would exhibit lower MR ratio. However, it has been established by earlier chapter that bcc-CoFe/Cu system could achieve large MR ratio and this data shows it experimentally that the formation of fcc-Cu among bcc-Cu degrades MR ratio. Therefore, this formation needs to be suppressed. The formation of bcc-Cu is result of having sandwiching CoFe layers around the Cu spacer. The strain from the surrounding bcc-CoFe stabilize the bcc phase of Cu, thus thinner Cu is favorable. Currently Cu thickness used in the Si/NiAl/CoFe/MgO SV is 3 nm. This Cu can be decreased down to reach critical thickness ~2 nm in order to stabilize bcc phase of Cu and suppressing fcc-Cu formation. At the same time, shunting will be reduced further due to less conductive channel which will also increase MR ratio.

6.3. Summary

Comparing the GMR performance of polycrystalline and epitaxial CoFe/Cu–based CIP-GMR give some glimpse of how better it is epitaxial (001)–oriented device is. Not only it has the benefit of larger spin-dependent scattering which potentially increase MR ratio but also it gives stability to keep the antiparallel state at low spacer thickness. Lower spacer thickness minimizes current shunting through the metallic spacer which maximize MR ratio value. Thus, attempting to grow epitaxial device despite the substrate limitation is necessary.

Epitaxial bcc-CoFe/bcc-Cu-based CIP-GMR device deposited on Si has been successfully fabricated. The shunting effect from the metallic underlayer has been nullified thanks to the insulating barrier, resulting in MR ratio of 12.0% and 15.6% for Si/NiAl/MgO and Si/NiAl/CoFe/MgO SVs respectively. As a comparison, MgO SV which was deposited on MgO substrate show larger MR ratio of 20.8% which is larger than both Si/NiAl/MgO and Si/NiAl/CoFe/MgO SVs. The lower MR ratio of Si/NiAl/MgO and Si/NiAl/CoFe/MgO SVs is due to the inferior crystal quality compared to MgO SV where Si/NiAl/MgO SV show polycrystalline growth and Si/NiAl/CoFe/MgO SV have unwanted fcc phase in its Cu spacer. Although it is still far from the destination, the development of the epitaxial CIP-GMR device on Si is on the right direction. Further improvement has to be done, for example by reducing Cu thickness to increase the stability of bcc-Cu which will suppress the formation of unwanted fcc phase. This study shows that growing epitaxial CIP-GMR on Si substrate is possible. This study also demonstrates the possibility of having any metallic underlayer for CIP-GMR with proper insulation.

Chapter 7: Summary and future directions

7.1. Summary

The works written in this thesis is intended to improve the magnetoresistance (MR) ratio of current-in-plane giant magnetoresistance (CIP-GMR) devices. Among the approaches and optimization that have been carried out, several important results that have been described in this thesis will be summarized.

1. The highly spin-polarized CFAS Heusler alloy was investigated in combination with Ag nonmagnetic (NM) layer. Epitaxial growth with B2-ordering which suggests high spin-polarization of bulk CFAS and high spin asymmetry of electronic conductance at the CFAS/Ag interfaces have been achieved. However, relatively low magnetoresistance (MR) ratio only up to 1.2% at room temperature (RT) were observed. After comparing it with a device using commonly used CoFe as FM, it is shown that high resistivity of CFAS suppress the generation of spin-polarized electron inside the bulk which ultimately reduce MR ratio.
2. Epitaxial $Co_{1-x}Fe_x$/Cu/$Co_{1-x}Fe_x$/IrMn was investigated ($x = 0.10, 0.25, 0.50, 0.67, 1$). Large MR ratio up to 26.5% have been achieved on $Co_{50}Fe_{50}$/Cu/$Co_{50}Fe_{50}$/IrMn. Microstructure analysis suggests the occurrence of bcc-Cu sandwiched between bcc-$Co_{50}Fe_{50}$. The bcc-Cu copy the lattice parameter of bcc-CoFe which make them almost identical. As a result, bcc-Cu can grow seamlessly with no interface defect at CoFe/Cu interfaces. Additionally, spin-dependent transmittance calculation reveals that bcc-Cu and bcc-CoFe are highly band matched which resulting in large MR ratio of this spin valve.
3. Large MR ratio in CoFe/Cu still comes with large hysteresis which is unwanted on the free layer. To reduce coercivity without much compromise to MR ratio and structure, CoFe and Ni were alloyed (CoFe: Ni = 80:20). After alloying with Ni for both pinned and free layer, MR ratio goes down from 20.8% in CoFe/Cu/CoFe to 11.2% in CoFeNi/Cu/CoFeNi. This reduction is attributed to the degradation of microstructure especially around Cu layer. This degradation can be avoided after changing only part of the free layer into the alloy. As a result, degradation of the microstructure can be avoided. However, despite having very similar structure close to CoFe there is still big MR ratio difference, suggesting that reduction of MR ratio may not only come from crystal structure but also from electronic band matching.
4. The success of bcc-CoFe combined with bcc-Cu in achieving large MR ratio comes with a price. Namely MgO (001) substrate is usually needed to grow this material epitaxially which is still considered impractical. More industrially viable approach using NiAl seed layer were investigated. Epitaxial bcc-CoFe/bcc-Cu CIP-GMR device deposited on Si substrate was demonstrated. MR ratio up to 15.6% at room temperature (RT) is exhibited by the device having NiAl/CoFe/MgO underlayer. Note that original spin valve device using MgO substrate exhibit 20.8%. Microstructure analysis suggests that the MR ratio difference stem from the existence of extra phase of Cu that is not bcc-Cu inside the device.

7.2. Future directions

So far, highly spin-polarized Heusler alloy does not seem to be the correct path to take in order to enhance the MR ratio in CIP-GMR. Heusler alloy has high resistivity which does not work well in CIP-GMR setup. Current shunting through the spacer or other layer will always become problem because of this. Also, Heusler alloy generally requires high temperature annealing to achieve chemical ordering. This high temperature annealing potentially roughen the FM/NM interfaces, reducing the critical thickness or even the MR ratio.

The use of bcc-CoFe/Cu–based CIP-GMR can be considered as one of many potential directions to obtain large MR ratio in CIP-GMR. Currently, despite having large MR ratio, there are still problems that has not been solved yet. One of them including large coercivity of the free layer. The addition of Ni into CoFe to approach zero magnetostriction line works well to reduce the coercivity, but the MR ratio reduction is still severe. This MR ratio reduction mostly caused by the degradation of the microstructure due to change in the lattice constant. Adjusting the composition of Co–Fe–Ni might be the required in this case. Other elements can also be added to stabilize the bcc structure.

Other place that needs improvement is the epitaxial growth on Si substrate. Even though the result is close to successful, it is still not perfect. Cu still have phase other than the desired bcc-Cu. This can be suppressed by changing the thickness of Cu spacer. Usually, lower Cu thickness may lead to more stable bcc-Cu phase. The process also needs to be more simplified. The use of high temperature annealing causes unwanted reaction between NiAl and the Si substrate. While it is not a problem in this study, it surely become a problem if this method will be used for large scale production.

There is still plenty room for improvement to enhance GMR properties. Metastable structure like bcc-Cu which improve interfacial lattice and band matching significantly can be discovered and then applied. First-principles calculation can be a powerful tool to evaluate or even predict the properties of CIP-GMR structure even before fabricating the sample.

References

[1] K. Elphick, W. Frost, M. Samiepour, T. Kubota, K. Takanashi, H. Sukegawa, S. Mitani, A. Hirohata, *Sci. Technol. Adv. Mater.* **2021**, *22*, 235.

[2] W. Thomson, *Proc. R. Soc. London* **1857**, *8*, 546.

[3] Binasch, Grünberg, Saurenbach, Zinn, *Phys. Rev. B. Condens. Matter* **1989**, *39*, 4828.

[4] M. N. Baibich, J. M. Broto, A. Fert, F. N. Van Dau, F. Petroff, P. Eitenne, G. Creuzet, A. Friederich, J. Chazelas, *Phys. Rev. Lett.* **1988**, *61*, 2472.

[5] N. F. Mott, *Adv. Phys.* **1964**, *13*, 325.

[6] C. H. Tsang, R. E. Fontana, T. Lin, D. E. Heim, B. A. Gurney, M. L. Williams, *IBM J. Res. Dev.* **1998**, *42*, 103.

[7] A. Hirohata, K. Takanashi, *J. Phys. D. Appl. Phys.* **2014**, *47*.

[8] W. P. Pratt, S.-F. Lee, J. M. Slaughter, ' R Loloee, P. A. Schroeder, J. Bass, *Phys. Rev. Lett.* **1991**, *66*, 3060.

[9] J. S. Moodera, L. R. Kinder, T. M. Wong, R. Meservey, *Phys. Rev. Lett.* **1995**, *74*, 3273.

[10] T. Miyazaki, N. Tezuka, *J. Magn. Magn. Mater.* **1995**, *139*, L231.

[11] J. E. Lenz, *Proc. IEEE* **1990**, *78*, 973.

[12] J. Heremans, *J. Phys. D. Appl. Phys.* **1993**, *26*, 1149.

[13] R. S. Popovic, J. A. Flanagan, P. A. Besse, *Sensors Actuators, A Phys.* **1996**, *56*, 39.

[14] L. Jogschies, D. Klaas, R. Kruppe, J. Rittinger, P. Taptimthong, A. Wienecke, L. Rissing, M. Wurz, *Sensors* **2015**, *15*, 28665.

[15] C. Zheng, K. Zhu, S. Cardoso de Freitas, J.-Y. Chang, J. E. Davies, P. Eames, P. P. Freitas, O. Kazakova, C. Kim, C.-W. Leung, S.-H. Liou, A. Ognev, S. N. Piramanayagam, P. Ripka, A. Samardak, K.-H. Shin, S.-Y. Tong, M.-J. Tung, S. X. Wang, S. Xue, X. Yin, P. W. T. Pong, *IEEE Trans. Magn.* **2019**, *55*, 1.

[16] B. Dieny, V. S. Speriosu, B. A. Gurney, S. S. P. Parkin, D. R. Wilhoit, K. P. Roche, S. Metin, D. T. Peterson, S. Nadimi, *J. Magn. Magn. Mater.* **1991**, *93*, 101.

[17] B. Dieny, V. S. Speriosu, S. S. P. Parkin, B. A. Gurney, D. R. Wilhoit, D. Mauri, *Phys. Rev. B* **1991**, *43*, 1297.

[18] J. S. Moodera, L. R. Kinder, T. M. Wong, R. Meservey, *Phys. Rev. Lett.* **1995**, *74*, 3273.

[19] T. Miyazaki, N. Tezuka, *J. Magn. Magn. Mater.* **1995**, *139*, L231.

[20] J. E. Davies, J. D. Watts, J. Novotny, D. Huang, P. G. Eames, *Appl. Phys. Lett.* **2021**, *118*.

[21] C. P. O. Treutler, *Sensors Actuators, A Phys.* **2001**, *91*, 2.

[22] A. Bernieri, G. Betta, L. Ferrigno, M. Laracca, *IEEE Sens. J.* **2013**, *13*, 4513.

[23] C. Reig, M.-D. Cubells-Beltrán, D. Ramírez Muñoz, *Sensors* **2009**, *9*, 7919.

[24] T. Costa, M. S. Piedade, J. Germano, J. Amaral, P. P. Freitas, *IEEE Trans. Instrum. Meas.* **2014**, *63*, 1171.

[25] A. Sobczak-Kupiec, J. Venkatesan, A. Alhathal AlAnezi, D. Walczyk, A. Farooqi, D. Malina, S. H. Hosseini, B. Tyliszczak, *Nanomedicine Nanotechnology, Biol. Med.* **2016**, *12*, 2459.

[26] K. Yang, H. Chen, L. Lu, X. Kong, R. Yang, J. Wang, *IEEE Trans. Appl. Supercond.* **2019**, *29*, 1.

[27] M. Buchner, K. Höfler, B. Henne, V. Ney, A. Ney, *J. Appl. Phys.* **2018**, *124*, 161101.

[28] J. Clarke, M. Hatridge, M. Mößle, *Annu. Rev. Biomed. Eng.* **2007**, *9*, 389.

[29] K. Fujiwara, M. Oogane, A. Kanno, M. Imada, J. Jono, T. Terauchi, T. Okuno, Y. Aritomi, M. Morikawa, M. Tsuchida, N. Nakasato, Y. Ando, *Appl. Phys. Express* **2018**, *11*.

[30] M. Oogane, K. Fujiwara, A. Kanno, T. Nakano, H. Wagatsuma, T. Arimoto, S. Mizukami, S. Kumagai, H. Matsuzaki, N. Nakasato, Y. Ando, *Appl. Phys. Express* **2021**, *14*, 123002.

[31] C. Reig, S. Cardoso, S. C. Mukhopadhyay, *Giant Magnetoresistance (GMR) Sensors*; Smart Sensors, Measurement and Instrumentation; Springer Berlin Heidelberg: Berlin, Heidelberg, 2013; Vol. 6.

[32] R. Sbiaa, H. Morita, *Appl. Phys. Lett.* **2004**, *84*, 5139.

[33] M. A. Seigler, *IEEE Trans. Magn.* **2007**, *43*, 651.

[34] L. Wang, J. J. Qiu, W. J. McMahon, K. B. Li, Y. H. Wu, *Phys. Rev. B - Condens. Matter Mater. Phys.* **2004**, *69*, 1.

[35] E. Y. Tsymbal, D. G. Pettifor, In *Solid State Physics - Advances in Research and Applications*; 2001; pp. 113–237.

[36] C. Vouille, A. Barthélémy, F. Elokan Mpondo, A. Fert, P. A. Schroeder, S. Y. Hsu, A. Reilly, R. Loloee, *Phys. Rev. B* **1999**, *60*, 6710.

[37] D. M. Edwards, J. Mathon, R. B. Muniz, *IEEE Trans. Magn.* **1991**, *27*, 3548.

[38] J. Mathon, *J. Magn. Magn. Mater.* **1991**, *100*, 527.

[39] A. Vedyaev, C. Cowache, N. Ryzhanova, B. Dieny, *Phys. Lett. A* **1995**, *198*, 267.

[40] J. Barnás, A. Fert, *J. Magn. Magn. Mater.* **1995**, *140–144*, 509.

[41] R. Schad, C. D. Potter, P. Beliën, G. Verbanck, J. Dekoster, G. Langouche, V. V. Moshchalkov, Y. Bruynseraede, *J. Magn. Magn. Mater.* **1995**, *148*, 331.

[42] S. S. P. Parkin, Z. G. Li, D. J. Smith, *Appl. Phys. Lett.* **1991**, *58*, 2710.

[43] S. S. P. Parkin, N. More, K. P. Roche, *Phys. Rev. Lett.* **1990**, *64*, 2304.

[44] T. L. Monchesky, B. Heinrich, R. Urban, K. Myrtle, **1999**, *60*, 242.

[45] B. Dieny, V. S. Speriosu, S. Metin, S. S. P. Parkin, B. A. Gurney, P. Baumgart, D. R. Wilhoit, *J. Appl. Phys.* **1991**, *69*, 4774.

[46] Jongill Hong, J. Kane, J. Hashimoto, M. Yamagishi, K. Noma, H. Kanai, *IEEE Trans. Magn.* **2002**, *38*, 15.

[47] D. M. Jeon, J. P. Lee, D. H. Lee, S. Y. Yoon, Y. S. Kim, S. J. Suh, *J. Magn. Magn. Mater.* **2004**, *272–276*, 1903.

[48] A. Gupta, S. Mohanan, M. Kinyanjui, A. Chuvilin, U. Kaiser, U. Herr, *J. Appl. Phys.* **2010**, *107*, 093910.

[49] A. Veloso, P. P. Freitas, P. Wei, N. P. Barradas, J. C. Soares, B. Almeida, J. B. Sousa, *Appl. Phys. Lett.* **2000**.

[50] J. D. Suh, C. A. Ross, In *Physica Status Solidi (B) Basic Research*; 2007; Vol. 244, pp. 4474–4477.

[51] P. V. Sreevidya, U. P. Borole, T. Gawade, J. Khan, C. L. Prajapat, Y. Kumar, H. C. Barshilia, P. Chowdhury, *J. Magn. Magn. Mater.* **2019**, *481*, 170.

[52] K. Inomata, S. Okamura, A. Miyazaki, M. Kikuchi, N. Tezuka, M. Wojcik, E. Jedryka, *J. Phys. D. Appl. Phys.* **2006**, *39*, 816.

[53] B. S. D. C. S. Varaprasad, A. Srinivasan, Y. K. Takahashi, M. Hayashi, A. Rajanikanth, K. Hono, *Acta Mater.* **2012**, *60*, 6257.

[54] R. A. de Groot, F. M. Mueller, P. G. van Engen, K. H. J. Buschow, *Phys. Rev. Lett.* **1983**, *50*, 2024.

[55] P. Mavropoulos, I. Galanakis, V. Popescu, P. H. Dederichs, *J. Phys. Condens. Matter* **2004**, *16*, S5759.

[56] S. Fujii, S. Sugimura, Ishida, S. Asano, *J. Phys. Condens. Matter* **1990**, *2*, 8583.

[57] S. Ishida, S. Fujii, S. Kashiwagi, S. Asano, *J. Phys. Soc. Japan* **1995**, *64*, 2152.

[58] I. Galanakis, *J. Phys. Condens. Matter* **2004**, *16*, 3089.

[59] H. C. Kandpal, G. H. Fecher, C. Felser, G. Schönhense, *Phys. Rev. B* **2006**, *73*, 094422.

[60] X.-Q. Chen, R. Podloucky, P. Rogl, *J. Appl. Phys.* **2006**, *100*, 113901.

[61] B. S. D. C. S. Varaprasad, A. Srinivasan, Y. K. Takahashi, M. Hayashi, A. Rajanikanth, K. Hono, *Acta Mater.* **2012**, *60*, 6257.

[62] S. C. Lee, T. D. Lee, P. Blaha, K. Schwarz, *J. Appl. Phys.* **2005**, *97*, 10C307.

[63] S. Idrissi, S. Ziti, H. Labrim, L. Bahmad, *J. Low Temp. Phys.* **2021**, *202*, 343.

[64] I. Kurniawan, K. Nawa, K. Masuda, Y. Miura, K. Hono, *Acta Mater.* **2021**, *218*, 117218.

[65] S. Li, Y. K. Takahashi, T. Furubayashi, K. Hono, *Appl. Phys. Lett.* **2013**, *103*, 042405.

[66] J. W. Jung, Y. Sakuraba, T. T. Sasaki, Y. Miura, K. Hono, *Appl. Phys. Lett.* **2016**, *108*, 102408.

[67] T. Kubota, Y. Ina, M. Tsujikawa, S. Morikawa, H. Narisawa, Z. Wen, M. Shirai, K. Takanashi, *J. Phys. D. Appl. Phys.* **2017**, *50*, 014004.

[68] K. Inomata, N. Ikeda, N. Tezuka, R. Goto, S. Sugimoto, M. Wojcik, E. Jedryka, *Sci. Technol. Adv. Mater.* **2008**, *9*, 014101.

[69] T. Furubayashi, K. Kodama, H. Sukegawa, Y. K. Takahashi, K. Inomata, K. Hono, *Appl. Phys. Lett.* **2008**, *93*, 122507.

[70] H. Sukegawa, W. Wang, R. Shan, T. Nakatani, K. Inomata, K. Hono, *Phys. Rev. B* **2009**, *79*, 184418.

[71] J. Chen, J. Liu, Y. Sakuraba, H. Sukegawa, S. Li, K. Hono, *APL Mater.* **2016**, *4*, 056104.

[72] J. W. Jung, Y. Sakuraba, T. T. Sasaki, Y. Miura, K. Hono, *Appl. Phys. Lett.* **2016**, *108*, 102408.

[73] T. M. Nakatani, T. Furubayashi, S. Kasai, H. Sukegawa, Y. K. Takahashi, S. Mitani, K. Hono, *Appl. Phys. Lett.* **2010**, *96*, 212501.

[74] T. Furubayashi, K. Kodama, T. M. Nakatani, H. Sukegawa, Y. K. Takahashi, K. Inomata, K. Hono, *J. Appl. Phys.* **2010**, *107*, 113917.

[75] T. M. Nakatani, T. Furubayashi, K. Hono, *J. Appl. Phys.* **2011**, *109*, 07B724.

[76] C. Hordequin, J. P. Noziè Res, J. Pierre, *J. Magn. Magn. Mater.* **1998**, *183*, 225.

[77] J. A. Caballero, Y. D. Park, J. R. Childress, J. Bass, W.-C. Chiang, A. C. Reilly, W. P. Pratt, F. Petroff, *J. Vac. Sci. Technol. A Vacuum, Surfaces, Film.* **1998**, *16*, 1801.

[78] D. L. Zhang, X. G. Xu, Y. Wu, J. Miao, Y. Jiang, *J. Magn. Magn. Mater.* **2011**, *323*, 631.

[79] J. P. Nozières, V. S. Speriosu, B. A. Gurney, B. Dieny, H. Lefakis, T. C. Huang, *J. Magn. Magn. Mater.* **1993**, *121*, 386.

[80] B. Dieny, *J. Magn. Magn. Mater.* **1994**, *136*, 335.

[81] P. . Grünberg, *Sensors Actuators A Phys.* **2001**, *91*, 153.

[82] R. Coehoorn, *Handb. Magn. Mater.* **2003**, *15*, 1.

[83] R. Sbiaa, H. Morita, *Appl. Phys. Lett.* **2004**, *84*, 5139.

[84] V. V. Ustinov, M. A. Milyaev, L. I. Naumova, *Phys. Met. Metallogr.* **2017**, *118*, 1300.

[85] M. Milyaev, L. Naumova, V. Proglyado, T. Krinitsina, N. Bannikova, V. Ustinov, *IEEE Trans. Magn.* **2019**, *55*, 1.

[86] S. Jo, M. Seigler, *J. Appl. Phys.* **2002**, *91*, 7110.

[87] J. Hong, H. Kanai, Y. Uehara, In *IEEE International Digest of Technical Papers on Magnetics Conference*; IEEE, 2002; p. CA3.

[88] F. Matroodi, M. G. Shoar, *J. Phys. Conf. Ser.* **2017**, *917*, 072001.

[89] L. Wang, J. J. Qiu, W. J. McMahon, K. B. Li, Y. H. Wu, *Phys. Rev. B* **2004**, *69*, 214402.

[90] N. Hasegawa, F. Koike, K. Ikarashi, M. Ishizone, M. Kawamura, Y. Nakazawa, A. Takahashi, H. Tomita, H. Iwasaki, M. Sahashi, *J. Appl. Phys.* **2002**, *91*, 8774.

[91] I. Ohnuma, H. Enoki, O. Ikeda, R. Kainuma, H. Ohtani, B. Sundman, K. Ishida, *Acta Mater.* **2002**, *50*, 379.

[92] I. Galanakis, 2016; pp. 3–36.

[93] W. Wang, H. Sukegawa, R. Shan, K. Inomata, *Appl. Phys. Lett.* **2008**, *93*, 2006.

[94] J. Bass, *J. Magn. Magn. Mater.* **2016**, *408*, 244.

[95] D. L. Zhang, X. G. Xu, Y. Wu, J. Miao, Y. Jiang, *J. Magn. Magn. Mater.* **2011**, *323*, 631.

[96] T. M. Nakatani, A. Rajanikanth, Z. Gercsi, Y. K. Takahashi, K. Inomata, K. Hono, *J. Appl. Phys.* **2007**, *102*, 033916.

[97] T. Furubayashi, K. Kodama, T. M. Nakatani, H. Sukegawa, Y. K. Takahashi, K. Inomata, K. Hono, *J. Appl. Phys.* **2010**, *107*, 113917.

[98] T. C. Schulthess, W. H. Butler, *J. Appl. Phys.* **2000**, *87*, 5759.

[99] H. Laidler, B. J. Hickey, T. P. A. Hase, B. K. Tanner, R. Schad, Y. Bruynseraede, *J. Magn. Magn. Mater.* **1996**, *156*, 332.

[100] T. Furubayashi, K. Kodama, T. M. Nakatani, H. Sukegawa, Y. K. Takahashi, K. Inomata, K. Hono, *J. Appl. Phys.* **2010**, *107*, 113917.

[101] K. B. Fathoni, Y. Sakuraba, Y. Miura, T. T. Sasaki, T. Nakatani, K. Hono, *J. Phys. D. Appl. Phys.* **2021**.

[102] G. H. Fecher, C. Felser, *J. Phys. D. Appl. Phys.* **2007**, *40*, 1582.

[103] H. Brown, E. Dan Dahlberg, C. Hou, *J. Appl. Phys.* **2001**, *89*, 7543.

[104] J. P. Perdew, K. Burke, M. Ernzerhof, *Phys. Rev. Lett.* **1996**, *77*, 3865.

[105] P. Giannozzi, S. Baroni, N. Bonini, M. Calandra, R. Car, C. Cavazzoni, D. Ceresoli, G. L. Chiarotti, M. Cococcioni, I. Dabo, A. Dal Corso, S. de Gironcoli, S. Fabris, G. Fratesi, R. Gebauer, U. Gerstmann, C. Gougoussis, A. Kokalj, M. Lazzeri, L. Martin-Samos, N. Marzari, F. Mauri, R. Mazzarello, S. Paolini, A. Pasquarello, L. Paulatto, C. Sbraccia, S. Scandolo, G. Sclauzero, A. P. Seitsonen, A. Smogunov, P. Umari, R. M. Wentzcovitch, *J. Phys. Condens. Matter* **2009**, *21*, 395502 (19pp).

[106] P. Giannozzi, O. Andreussi, T. Brumme, O. Bunau, M. B. Nardelli, M. Calandra, R. Car, C. Cavazzoni, D. Ceresoli, M. Cococcioni, N. Colonna, I. Carnimeo, A. D. Corso, S. de Gironcoli, P. Delugas, R. A. D. Jr, A. Ferretti, A. Floris, G. Fratesi, G. Fugallo, R. Gebauer, U. Gerstmann, F. Giustino, T. Gorni, J. Jia, M. Kawamura, H.-Y. Ko, A. Kokalj, E. Küçükbenli, M. Lazzeri, M.

Marsili, N. Marzari, F. Mauri, N. L. Nguyen, H.-V. Nguyen, A. Otero-de-la-Roza, L. Paulatto, S. Poncé, D. Rocca, R. Sabatini, B. Santra, M. Schlipf, A. P. Seitsonen, A. Smogunov, I. Timrov, T. Thonhauser, P. Umari, N. Vast, X. Wu, S. Baroni, *J. Phys. Condens. Matter* **2017**, *29*, 465901.

[107] S. Baroni, A. Dal Corso, S. de Gironcoli, P. Gianozzi, Quantum Espresso.

[108] S. Li, T. Nakatani, K. Masuda, Y. Sakuraba, X. D. Xu, T. T. Sasaki, H. Tajiri, Y. Miura, T. Furubayashi, K. Hono, *Acta Mater.* **2018**, *142*, 49.

[109] Y. Sakuraba, K. Izumi, T. Iwase, S. Bosu, K. Saito, K. Takanashi, Y. Miura, K. Futatsukawa, K. Abe, M. Shirai, *Phys. Rev. B* **2010**, *82*, 094444.

[110] B. Büker, J. Jung, T. Sasaki, Y. Sakuraba, Y. Miura, T. Nakatani, A. Hütten, K. Hono, *Phys. Rev. B* **2021**, *103*, L140405.

[111] R. Sbiaa, H. Morita, *Appl. Phys. Lett.* **2004**, *84*, 5139.

[112] COMSOL AB, *COMSOL Multiphysics® v.5.6*; Stockholm, Sweden, 2020.

[113] A. Kohn, A. Kovács, R. Fan, G. J. McIntyre, R. C. C. Ward, J. P. Goff, *Sci. Rep.* **2013**, *3*, 1.

[114] T. L. Monchesky, R. Urban, B. Heinrich, M. Klaua, J. Kirschner, *J. Appl. Phys.* **2000**, *87*, 5167.

[115] Sining Mao, Zheng Gao, *IEEE Trans. Magn.* **2000**, *36*, 2860.

[116] J. R. Childress, R. E. Fontana, *Comptes Rendus Phys.* **2005**, *6*, 997.

[117] T. Mizuguchi, T. Miyauchi, *IEEE Trans. Magn.* **1999**, *35*, 2598.

[118] P. D. Kulkarni, T. Nakatani, T. Sasaki, Y. Sakuraba, *J. Appl. Phys.* **2021**, *129*, 213901.

[119] B. Heinrich, Z. Celinski, J. F. Cochran, W. B. Muir, J. Rudd, Q. M. Zhong, A. S. Arrott, K. Myrtle, J. Kirschner, *Phys. Rev. Lett.* **1990**, *64*, 673.

[120] Y. Kamiguchi, H. Yuasa, H. Fukuzawa, K. Koui, H. Iwasaki, M. Sahashi, *Dig. INTERMAG* **1999**.

[121] Z. Celinski, B. Heinrich, *J. Magn. Magn. Mater.* **1991**, *99*, 25.

[122] B. Dieny, V. S. Speriosu, S. S. P. Parkin, B. A. Gurney, D. R. Wilhoit, D. Mauri, *Phys. Rev. B* **1991**, *43*, 1297.

[123] K. B. Fathoni, Y. Sakuraba, T. Sasaki, Y. Miura, J. W. Jung, T. Nakatani, K. Hono, *APL Mater.* **2019**, *7*.

[124] S. Ishio, T. Kobayashi, H. Saito, S. Sugawara, S. Kadowaki, *J. Magn. Magn. Mater.* **1996**, *164*, 208.

[125] M. Urbaniak, F. Stobiecki, T. Luciński, M. Kopcewicz, A. Grabias, J. Aleksiejew, *Acta Phys. Pol. A* **2000**, *97*, 539.

[126] R. Bai, Z. Qian, H. Zhu, Q. Li, Y. Li, Y. Peng, D. Huo, *IEEE Trans. Magn.* **2017**, *53*, 1.

[127] S. S. P. Parkin, *Phys. Rev. Lett.* **1993**, *71*, 1641.

[128] E. A. Stern, *Phys. Rev.* **1967**, *157*, 544.

[129] M. Saito, N. Hasegawa, K. Tanaka, Y. Ide, F. Koike, T. Kuriyama, *J. Appl. Phys.* **2000**, *87*, 6974.

[130] S. Araki, M. Sano, S. Li, Y. Tsuchiya, O. Redon, T. Sasaki, N. Ito, K. Terunuma, H. Morita, M. Matsuzaki, *J. Appl. Phys.* **2000**, *87*, 5377.

[131] K. M. H. Lenssen, D. J. Adelerhof, H. J. Gassen, A. E. T. Kuiper, G. H. J. Somers, J. B. A. D. Van Zon, *Sensors Actuators, A Phys.* **2000**, *85*, 1.

[132] M. J. Carey, T. Le, T. Thompson, B. A. Gurney, *J. Appl. Phys.* **2002**, *92*, 4538.

[133] C. L. Lee, A. Devasahayam, M. Mao, J. Kools, P. Cox, K. Masaryk, D. Mahenthiran, J. Munson, *J. Appl. Phys.* **2003**, *93*, 8406.

[134] V. A. Vas'ko, M. T. Kief, *J. Appl. Phys.* **2003**, *93*, 8409.

[135] T. Mizuguchi, S. Terada, T. Miyauchi, A. Matsuzono, *IEEE Trans. Magn.* **1998**, *34*, 1504.

[136] X. Peng, A. Morrone, K. Nikolaev, M. Kief, M. Ostrowski, *J. Magn. Magn. Mater.* **2009**, *321*, 2902.

[137] Y. Maeda, K. Hamaya, S. Yamada, Y. Ando, K. Yamane, M. Miyao, *Appl. Phys. Lett.* **2010**, *97*.

[138] S. Sakai, M. Kawano, M. Ikawa, H. Sato, S. Yamada, K. Hamaya, *Semicond. Sci. Technol.* **2017**, *32*.

[139] H. Sugiyama, M. Ishikawa, T. Inokuchi, T. Tanamoto, Y. Saito, N. Tezuka, *Solid State Commun.* **2014**, *190*, 49.

[140] J. Chen, J. Liu, Y. Sakuraba, H. Sukegawa, S. Li, K. Hono, *APL Mater.* **2016**, *4*.

[141] J. Chen, Y. Sakuraba, K. Yakushiji, Y. Kurashima, N. Watanabe, J. Liu, S. Li, A. Fukushima, H. Takagi, K. Kikuchi, S. Yuasa, K. Hono, *Acta Mater.* **2020**, *200*, 1038.

[142] K. Yakushiji, A. Sugihara, T. Nakano, S. Yuasa, *Appl. Phys. Lett.* **2019**, *115*, 202403.

[143] T. G. S. M. Rijks, R. L. H. Sour, D. G. Neerinck, A. E. M. De Veirman, R. Coehoorn, J. C. S. Kools, M. F. Gillies, W. J. M. de Jonge, *IEEE Trans. Magn.* **1995**, *31*, 3865.

[144] T. C. Schulthess, W. H. Butler, *J. Appl. Phys.* **2000**, *87*, 5759.

[145] J. M. D. Coey, *J. Appl. Phys.* **2003**, *93*, 8224.

[146] J. Chen, Y. Sakuraba, K. Yakushiji, Y. Kurashima, N. Watanabe, J. Liu, S. Li, A. Fukushima, H. Takagi, K. Kikuchi, S. Yuasa, K. Hono, *Acta Mater.* **2020**, *200*, 1038.

[147] A. D. Smigelskas, E. O. Kirkendall, *Trans. AIME* **1947**, *171*, 130.

[148] H. J. T. Ellingham, *J. Soc. Chem. Ind.* **1944**, *63*, 125.

[149] U. of Cambridge, The Interactive Ellingham Diagram.

[150] M. El Harfaoui, H. Le Gall, J. Ben Youssef, S. Pogossian, A. Thiaville, P. Gogol, A. Qachaou, J. . Desvignes, *J. Magn. Magn. Mater.* **1999**, *198–199*, 107.

[151] D. Gall, *J. Appl. Phys.* **2016**, *119*, 085101.

Publication

K. B. Fathoni, Y. Sakuraba, T. Sasaki, Y. Miura, J. W. Jung, T. Nakatani and K. Hono
"Band match enhanced current-in-plane giant magnetoresistance in epitaxial $Co_{50}Fe_{50}$/Cu multilayers with metastable bcc-Cu spacer"
APL Mater. **7**, 111106 (2019) https://doi.org/10.1063/1.5119370

K. B. Fathoni, Y. Sakuraba, Y. Miura, T. Sasaki, T. Nakatani and K. Hono
"Analysis of current-in-plane giant magnetoresistance using $Co_2FeAl_{0.5}Si_{0.5}$ half-metallic Heusler alloy"
J. Phys. D: Appl. Phys. **55**, 125001 (2021) https://doi.org/10.1088/1361-6463/ac3b12

K. B. Fathoni, T. Nakatani, Y. Sakuraba, Z. H. Li, T. Sasaki, and K. Hono
"Epitaxial bcc-Cu/$Co_{50}Fe_{50}$-based current-in-plane giant magnetoresistive spin valve on Si(001) wafer"
J. Magn. Magn. Mater **551**, 169154 (2022) https://doi.org/10.1016/j.jmmm.2022.169154